



HAL
open science

Physical and chemical phenomena occurring between solid ceramics and liquid metals and alloys at laser and plasma composite coatings formation: A review

Soufiane Oukach, Bernard Pateyron, Lech Pawlowski

► To cite this version:

Soufiane Oukach, Bernard Pateyron, Lech Pawlowski. Physical and chemical phenomena occurring between solid ceramics and liquid metals and alloys at laser and plasma composite coatings formation: A review. *Surface Science Reports*, 2019, 74 (3), pp.213-241. 10.1016/j.surfrep.2019.06.001 . hal-02447325

HAL Id: hal-02447325

<https://unilim.hal.science/hal-02447325>

Submitted on 20 Jul 2022

HAL is a multi-disciplinary open access archive for the deposit and dissemination of scientific research documents, whether they are published or not. The documents may come from teaching and research institutions in France or abroad, or from public or private research centers.

L'archive ouverte pluridisciplinaire **HAL**, est destinée au dépôt et à la diffusion de documents scientifiques de niveau recherche, publiés ou non, émanant des établissements d'enseignement et de recherche français ou étrangers, des laboratoires publics ou privés.



Distributed under a Creative Commons Attribution - NonCommercial 4.0 International License

Physical and chemical phenomena occurring between solid ceramics and liquid metals and alloys at laser and plasma composite coatings formation: A review

Soufiane Oukach¹, Bernard Pateyron², Lech Pawłowski^{2,*}

¹ Energy and Sustainable Development Research Team, High School of Technology, Ibn Zohr University, 81000 Guelmim, Morocco

² IRCER UMR CNRS 7315, University of Limoges, 87068 Limoges, France

*) Corresponding author: Phone +33(0)587 50 24 12, E-mail: lech.pawlowski@unilim.fr

Abstract

The review describes the physical and chemical phenomena occurring between solid ceramics used as reinforcement and liquid metals and alloys used as matrix in the composite coatings. Initially, the properties of typical matrix metals as Ni, Co, Fe and alloys as Ni-based (NiCr, NiAl, NiCrAlY,...) and Co-based (*Stellites*) alloys in liquid state are described. Then, the phenomena related to the diffusion of some atoms such as nitrogen or carbon in liquid metals and alloys solidification are described. Subsequently, the phenomena at the interface between liquid metals and alloys and solid ceramics such as oxides or carbides during the coatings' formation are reviewed. Finally, the methods of composite coatings deposition using laser cladding and plasma transferred arc are described and the properties of the composite coatings related to their microstructure are discussed by taking into account the phenomena in melt-pool.

Keywords

Metal matrix composite; coatings build-up; plasma transferred arc, laser cladding, hardfacing, wetting of solid ceramics by liquid metal

Table of Content

Abstract

Keywords

Content

Acronyms and symbols

Acronyms

Symbols

Greeks letters

Indices

Exponents

1. Introduction

2. Properties of composite matrices of metals and alloys

2.1. Mechanical properties of some metals and alloys

2.1.1. *Nickel based alloys*

2.1.1.1. Nichrome

2.1.1.2. Nickel aluminides

2.1.1.3. MCrAlY

2.1.1.4. NiCrBSi

2.1.1.5. *Inconel*TM

2.1.1.6. *Hastelloy*TM

2.1.2. *Cobalt alloys*

2.1.2.1. *Stellite*TM

2.1.2.2. ***Triballoy***TM

2.1.3. *Titanium alloys*

2.1.4. *Iron-based superalloys*

2.2. Thermodynamic properties

2.2.1. *Gibbs free energy*

2.2.2. *Surface energy*

2.2.3. *Volumetric thermal expansion*

2.3. Diffusion in liquid phase

2.3.1. *Diffusion of carbon*

2.3.2. *Diffusion of nitrogen*

2.3.3. *Diffusion of oxygen*

2.4. *Surface tension* of metals in liquid phase

3. Physical properties of oxides and carbides used for composites reinforcements

4. Interface between ceramics and liquid metals and alloys

4.1. Fundamentals of wetting

4.1.1. *Non-reactive wetting*

- 4.1.2. *Wetting between metals or alloys and carbides*
 - 4.1.3. *Wetting between metals and alloys and oxides*
 - 4.2. Reactive wetting
 - 4.2.1. *Dissolutive wetting*
 - 4.2.2. *Local reaction at contact*
 - 4.2.3. *Examples of wetting between metals or alloys and oxides*
- 5. Modern methods of *hardfacing*
 - 5.1. Plasma Transferred Arc (PTA)
 - 5.2. Laser assisted methods
- 6. Cermet coatings obtained by *hardfacing*
 - 6.1. Feedstock used in processing
 - 6.2. Phenomena in melt-pool
 - 6.2.1. *Physical phenomena*
 - 6.2.2. *Chemical phenomena*
 - 6.3. Flame and plasma assisted methods
 - 6.3.1. *Typical microstructure of coatings*
 - 6.3.2. *Properties of coatings*
 - 6.4. Laser assisted methods
 - 6.4.1. *Typical microstructure of coatings*
 - 6.4.2. *Properties of coatings*

Bibliography

Acronyms and symbols

Acronyms

1SLD - One-step laser deposition

2SLD – Two steps laser deposition

13YSZ- $ZrO_2+13 \text{ wt. } \% Y_2O_3$

CaP – Calcium phosphates

CFM - Compound formation model

CSM - Conformal solution model

cw – Continuous wave

EDS – Energy Dispersive X-ray Spectroscopy

HA - Hydroxyapatite, $Ca_{10}(PO_4)_6(OH)_2$

HAZ- Heat affected zone

HPTA – High power plasma transferred arc

HRC - Rockwell hardness scale C

HSM - Hard sphere model

LAPD – Laser-assisted powder deposition

LSA – Laser surface alloying

MD - Molecular dynamic

MIG – Metal inert gas

MMC – Metal matrix composite

MPTA - Micro plasma transferred arc

OD – Outer diameter

PAW – Plasma arc welding

PPM - Pseudo potential model

PRMMC – Particle reinforced metal matrix composite

PTA - Plasma transferred arc

QCA - Quasi-Chemical Approximation

QSM – Quasi-regular solution model

RT – Room temperature

SEM – Scanning electronic microscope

slpm – Standard liter per hour

SMMC – Surface metal matrix composite

TCP – Tricalcium phosphate, $\text{Ca}_3(\text{PO}_4)_2$

TEM – Transmission electron microscope

TIG – Tungsten inert gas

TTCP – Tetracalcium phosphate, $\text{Ca}_4\text{P}_2\text{O}_9$

XRD – X-ray diffraction

YAG – Yttrium aluminum garnet

YSZ – Yttria stabilized zirconia

Symbols

A – surface, m^2

C – concentration, $1/\text{m}^3$

c - constant

d – diameter, m

D - diffusion coefficient, m^2/s

E – Energy, J or Young modulus, GPa

H – Enthalpy, J/kg

HB – Brinell hardness

HV - Vickers hardness

HV30 – Vickers hardness under load of 30 kgf

HRC – Rockwell hardness

k – Boltzmann's constant, $k \approx 1.38 \times 10^{-23} \text{ J/K}$

k_y – strengthening coefficient, $\text{MPa}\cdot\text{m}^{0.5}$

M – molar mass, g/mol

P – pressure, Pa or power, W

Q – deposition factor (see Eq. 9), $\text{J}\cdot\text{s}/(\text{m}\cdot\text{kg})$ or activation energy, J

q – feed rate, kg/s or power density, W/m^2

R – constant of perfect gases $R \approx 8.314 \text{ J}/(\text{K}\cdot\text{mol})$

r – radius, m

slpm – standard liter per minute

T – Temperature, K

t – time, s

U – speed, m/s^1

V – volume, m^3

W_a – work of adhesion, J/m^2

X – fraction (see Table 9)

Y – fraction (see Table 9)

Greeks letters

α – thermal expansion coefficient, K^{-1}

γ – surface tension, J/m^2

λ - heat conductivity, $\text{W}/(\text{m}\cdot\text{K})$

ΔG – Gibbs free energy, J/mol

ΔG_r^0 - Gibbs free energy of formation, J/mol

ΔH_f^0 - enthalpy of formation, J/mol

ΔH_m - Gibbs free energy of mixing, J/mol

θ - angle of contact, °

ρ - density, kg/m³

σ - stress, MPa or surface energy, J/m²

τ - duration of pulse, s

Indices

0 - initial

a - adhesion

Al - aluminum

ch - chemistry

cheq - chemical equilibrium

Cr - chromium

Cu - copper

eV - evaporation

f - free

Fe - iron

LV - contact between liquid and vapor

m - melting or molar

M - mixing

neq - non - equilibrium

Ni - nickel

P - pressure

pd - plastic deformation

SL - contact between solid and liquid

SV – contact between solid and vapor

Ti - titanium

V – volumetric

VDW – van der Waals

y – yield

Zr – zirconium

Exponents

Int – interface

1. Introduction

The elaboration of composite materials enables obtaining interesting properties, impossible to reach in homogeneous materials. These properties are particularly important on their surfaces enhancing their usefulness and duration in service. One of the ways leading to a formation of composites is melting of material surface and injecting of a reinforcement. The methods associated with such manufacturing technology are called often **hardfacing** or surfacing by welding. Frequently, the molten surface is of metallic or alloy substrate and reinforcement is of such ceramics as carbides and/or oxides. The coatings technology may be categorized following the way of substrate melting, which occurs mainly by: (i) combustion flame; (ii) plasma and electric arc (plasma transferred arc, PTA); and, (iii) laser beam (laser cladding). Most of the published recently papers describe the coatings manufactured by PTA and by laser cladding and many of properties of coatings obtained with these two techniques are analyzed carefully in present review. The properties of composite metal matrix composite (MMC) coatings, called also surface metal matrix composites (SMMC), depend strongly of geometric factors such as shape of reinforcement and its distribution in the matrix [1]. The present review is focused on the metal matrix composites reinforced with ceramics powder, called particles reinforced MMC (PRMMC). The distribution of the reinforcement in the matrix depends strongly on the phenomena related to the wettability of solid reinforcement in liquid matrix and is also discussed in the review. The phenomena occur at high temperatures during the short time when the heat source melts the substrate forming a liquid bath which subsequently solidifies [2, 3]. The review describes the substrates being applied often in **hardfacing**, namely metals

such as Ni, Co and Fe and alloys such as NiCr, NiCrAlY, stellites and stainless steel. Consequently, phase diagrams and some properties including some thermodynamic functions, surface energy, thermal expansion of selected metals and alloys are shortly reviewed. The problems related to rapid solidification with the rate ranging from 10^4 to 10^8 K/s of metals and alloys included in composites influence their microstructures [4, 5]. In some solidification conditions the amorphous or dendrites including microstructure can be formed. The liquid matrix remains during a short time in contact with solid ceramics. The related phenomena are discussed starting from the *law of Young-Dupré* [6]. The described phenomena may occur with or without a chemical reaction on the interface between metallic matrix and ceramics. An important element of discussion is related to the geometry of liquid with solid interaction. Namely, in most of the cases discussed in the literature a liquid droplet is in contact with cold substrate (see Fig. 1 a). Inversely, at *hardfacing*, the solid particles are surrounded by liquid material as shows. The angle of wetting influences, in this case, the porosity between particle and matrix as show it Fig. 1 b.

(Fig. 1)

Fig. 1 Geometry of liquid droplet spread out on flat solid substrate (a) and of a solid particle being surrounded by a liquid (b).

Some important factors influencing the reactive and no-reactive wetting are shortly described. Finally, the techniques being presently used for *hardfacing*, including plasma and laser assisted ones, are described in details.

The *hardfacing* is accompanied by melting of metallic substrate by plasma, flame or laser. The sources of heat, the methods of melting as well as the phenomena occurring may be found in the papers related to welding. For example, the modern methods of plasma arc welding were recently reviewed by Liu *et al.* [7].

The metal matrix composite (MMC) coatings may be obtained using PTA, laser cladding and thermal spraying. These composites were reviewed by Deuis *et al.* [8]. However, it is also possible to manufacture the MMC using other methods. An example is heat treatment of preplaced powder. Consequently, Fan *et al.* [9] preplaced the mixture of Ti-Zr-Cu-Ni alloy matrix with TiC powder reinforcement onto Ti6Al4V substrate. The mixture was subsequently submitted to vacuum heat treatment what enabled obtaining composite coatings. It must be added, that temperature of treatment was low and the substrate did not melt. Consequently, the method is different than the *hardfacing* associated formation of melt-pool in substrate by plasma, flame or laser.

The quality of the composite coatings produced by *hardfacing* depends on many factors related to the phenomena occurring at the processing. The process parameters resulting in a formation of melt pool and on interaction of liquid metal/alloy with solid ceramics are particularly important. The present review focuses on this interaction.

2. Properties of composite matrices of metals and alloys

The MMC are most frequently composed of metals as Al, Ni, Co, Ti, Fe and their alloys being matrix and ceramic particles or fibers of SiC, Al₂O₃, B₄C etc. being reinforcement. The properties of the composites result essentially from: (i) chemical compositions of matrix and reinforcement; (ii) volume fraction of reinforcement; (iii) reinforcement size. The matrix is generally monolithic, and the added reinforcement should be distributed homogeneously as shows it Fig. 2.

(Fig. 2)

Fig. 2 Micrographic structure of typical MMC (self-fluxing alloy reinforced with tungsten carbide) available commercially as MetcoClad 52052™. Reproduced with permission of Oerlikon Metco.

MMC can be categorized as particulate composites reinforced with particles and fibrous composites reinforced with continuous monofilaments or short fibers (e.g. whiskers). Particulate MMC are more frequently applied while fibrous ones have only a few industrial applications. In fact, although the mechanical properties of fibrous composites, especially that reinforced with the monofilaments, are very good, their cost is generally higher than 100 €/kg. The high price results from the price of fibers and from the difficulty of their introduction into the matrix. That is why, the authors decided to focus the review on particulate MMCs.

It can be mentioned that the composites of cobalt reinforced with WC particles or that of nickel reinforced with TiC, TiN or Mo₂C are used frequently for cutting and mining tools and for high temperature protection. The ceramic materials used frequently for reinforcement of composites are also SiC and Al₂O₃ and, to a lesser extent, ZrO₂, Al₂TiO₅, B₄C and Si₃N₄. The reinforcing particles may be also mixture of these different ceramics and may be characterized by their composition, size, hardness and shape (see e.g. Emanian *et al.* [10]).

2.1. Mechanical properties of some metals and alloys

The main application of MMC is wear resistance against abrasion, erosion and friction. Indeed, the service life of wear parts coated with MMC may be tripled with regards to uncoated alloys.

Comparing to aluminum alloys, MMCs may also have slightly higher (by 10 to 20 %) Young's modulus and yield strength. It is also possible to modify the coefficient of expansion of the composite by adding an appropriate quantity of reinforcement.

The ceramic particles finely dispersed in a matrix improve the mechanical properties of the MMCs by the following ways:

- reinforcement particles are breakpoints to the propagation of a cracks and slow down their speed;
- cracks cannot propagate in a straight line as in pure matrix but rather zigzag between the particles what increases the total path of propagation.

Some properties of pure metals are collected in Table 1. Some properties may be improved by the use of **superalloys**. The *superalloys*, which are high performance metal alloys, have excellent mechanical strength and good creep resistance up to high temperatures (about $0.7 - 0.8 \times T_m$), and are resistant against corrosion. Their crystal structure is typically face centered cubic. The metals used in *superalloys* are most often nickel, cobalt and iron and to a lesser extent, titanium and aluminum. The *superalloys* found their applications in aircraft engine turbines (turbojet turbines blades) and gas turbines. They are identified by their trade names, such as: **Hastelloy**, **Inconel**, **Stellite**.

Table 1

Some properties of pure metals [11].

2.1.1. *Nickel-based alloys*

Nickel-based *superalloys*, such as Ni-Al-Cr, are used in high-temperature applications requiring high hot corrosion resistance. The examples are power-generation turbines and aircraft engines. The ductility of the Ni-based alloy is improved by adding Cr. Similarly, the addition of a few wt. % of Cr (up to 8) to the Ni₃Al improves the tensile strength of the alloy.

On the other hand, Co and Co–Ni based alloys with high Cr content are particularly efficient against hot corrosion. An addition of a small amount of Y, Si and Hf improves stability of alloys and the addition of Ta or Re - their oxidation resistance [12, 13].

2.1.1.1. Nichrome

The data showed in Table 2 concern the most commonly used alloy composed of nickel and 20 wt. % chromium. However, there are many other compositions of these metals for various applications. Nichrome is corrosion resistant. Because of its low cost of manufacturing, high strength, ductility, resistance to oxidation, stability at high temperatures, this alloy is widely used in electric heating elements used e. g. as hair dryers.

Table 2

Properties of NiCr (Ni+ 20 wt. % Cr) in standard conditions [14]

2.1.1.2. Nickel aluminides

Nickel aluminides are intermetallic alloys of nickel and aluminum having properties intermediate between ceramics and metals. The nickel aluminides include Ni_3Al , NiAl , and NiAl_3 . Nickel aluminides have useful mechanical properties and high thermal conductivity at high temperatures but they may be fractured in a brittle way at ambient temperatures [15, 16]. These compounds are applied frequently in gas turbines and jet engines. IC-221M alloy includes Ni_3Al and some other elements such as chromium, molybdenum, zirconium and boron [16]. The addition of boron increases the ductility of the alloy and its hardness. This strengthening occurs by **effect Hall - Petch** i.e. by decrease of the crystallites size which hampers the movement of dislocations and modifies the yield strength. This alloy is even stronger than well-known SAE 304 stainless steel and its strength increases from room temperature up to 800 °C [15, 16].

Nickel aluminides are resistant against heat and corrosion and some of their properties are collected in Table 3.

Table 3

Properties of nickel aluminides [16]

2.1.1.3. MCrAlY

MCrAlY alloys (where M is metal as Co, Fe, Ni or Co/Ni) are widely used as corrosion resistant materials. A well-known application is a bond-coating for use with zirconia top-coating in thermal barrier coatings. The high temperature corrosion resistance of MCrAlY results from the formation of oxides on alloys surface. The protective role of Cr and Al oxides in MCrAlY alloys is promoted by the

presence of Y. The oxidation behavior of MCrAlY alloys with different content of aluminum was discussed by e.g. Brandl *et al.* [17].

2.1.1.4. NiCrBSi

NiCrBSi is a group of Ni-based alloy with useful mechanical properties resulting from the presence of carbides and borides dispersed in the microstructure. This alloy is used as MMCs matrix for the applications requiring high wear resistance. The NiCrBSi contributes in MMCs functionality with high toughness. The typical alloy is composed of Ni (bal.) + 12-18 wt. % of Cr + 3-6 wt. % of Si + 2-6 wt. % of Fe + 1-5 wt. % of B and small contents of Al and of C.

2.1.1.5. Inconel™

Inconels are the alloys belonging to austenitic nickel-chromium-based *superalloys* [18]. The alloys resist against corrosion and oxidation because of formation of stable passive oxide layer on their surface. The alloys, including e.g. *Inconel 600*, *Inconel 617*, *Inconel 626* or *Inconel 690* have slightly different chemical composition including mainly nickel and chromium as a second element. *Inconels* retain their strength at high temperatures. This strength results from solid solution strengthening or from precipitation hardening.

2.1.1.6. Hastelloy™

Hastelloys belong to a family of nickel alloys *superalloys* including also chromium, cobalt, copper, iron, manganese, aluminum, magnesium, molybdenum, silicon, zirconium and titanium and other elements being particularly resistant to corrosion. The alloys may be also used resistant against high temperature corrosion and against wear. There is a lot of *Hastelloys* having different composition. The alloys are noted by the letters associated with numbers. Table 4 shows the composition of some *Hastelloys*.

Table 4

Chemical composition of some *Hastelloys* [19].

2.1.2. Cobalt alloys

2.1.2.1. Stellite™

Stellites belong to a family of cobalt-chromium alloys. Their chemical composition includes also some amount of tungsten, molybdenum, and of carbon. The alloys are resistant against wear and e.g. *Stellite 100* is used frequently for manufacturing of cutting tools [20]. The *stellites* may be

composed to be resistant against high temperatures corrosion. The alloys are hard and difficult to be machined and are, consequently, manufactured rather by casting.

2.1.2.2. *Tribaloy™*

CoMoCrSi alloys, known also as *Tribaloy™*, combine wear and corrosion resistance with mechanical strength. The alloys include very hard intermetallic phases known as **Laves phases** [21]. T-800 *Tribaloy* alloy includes about 50 % of these hard phases in soft cobalt matrix. This alloy is useful in contact with a hard surface where lubrication is difficult to apply. However, the alloy is brittle and has low resistance against crack initiation and propagation. This is particularly important in processing associated with high thermal stresses generation such as e.g. laser cladding [22]. A reduction of these hard phases content may be realized by addition of Ni done in T-900 alloy which is more ductile than T-800 alloy having however lower hardness and wear resistance.

2.1.3. *Titanium alloys*

Titanium alloys are very light and have high tensile strength and toughness. Moreover, they resist well against corrosion thanks to the passivation layer on their surface and against high temperature. A major drawback is the cost of raw materials and of their processing what limits their application to selected fields such as e.g. military or aviation industry [23]. *Titanium and its alloys include e.g.* [24]:

- T40, which is nearly pure titanium with a small addition of iron and oxygen used in aeronautic industry having density of 4510 kg/m³ and tensile strength of 550 MPa;
- Ti-6Al-7Nb developed recently to replace a well-known alloy Ti-6Al-4V for medical applications includes titanium alloyed with 6% aluminum and 7 % niobium and has a density of 4520 kg/m³ and tensile strength as high as 900 MPa.

2.1.4. *Iron-based superalloys*

The iron-based *superalloys*, which are less expensive than that cobalt- or nickel-based can be categorized in a following way [25]: (i) alloys strengthened by a martensitic type of transformation; (ii) austenitic alloys strengthened by a sequence of hot and cold working; and, (iii) austenitic alloys strengthened by precipitation hardening. Generally, the martensitic types of alloys are used at temperatures below 800 K and the austenitic types above this temperature.

Iron-based *superalloys* are resistant against corrosion and wear. The latter increases with carbon content. The alloys 611, 612, and 613 are used against wear resistance. The martensitic steels are difficult to weld and should be annealed or tempered prior to welding.

2.2. Thermodynamic properties

The reviewed thermodynamic properties of liquid alloys concern mainly: (i) **Gibbs free energy**; (ii) surface energy; and, (iii) thermal expansion. The theoretical models will be used if the experimental measurements of properties of liquid alloys are not available.

2.2.1. Gibbs free energy

Gibbs free energy, ΔG , is also known as free enthalpy is a maximum energy which may be obtained from a system at constant temperature and pressure. The reacting system has a natural tendency to reach minimum *Gibbs free energy*. It provides information about atomic bonding strength and about stability of the alloys. The *Gibbs free energy*, ΔG , is negative for spontaneous processes, being positive for non-spontaneous ones. The following models can be used to study the behavior of liquid alloys:

- **Pseudo-potential model** [26-27] which can be generated for a chemical element, using different methods. This pseudo-potential can then be specifically used for a given system or for a group of systems in order to describe their physical properties.
- **Hard sphere model** [28-31] is frequently used to describe particles of fluids and solids in a statistical way. The spheres are submitted to strong repulsion that at very close distances. The hard spheres model is used in analytical studies and in numerical simulations of molecules movement.
- **Conformal solution model** [32-33] is used when two mixed molecules are not very different and when full information of pure components is available. The model consists of use one component as a perturbation of a reference system.
- **Quasi-Chemical Approximation (QCA)**, developed by Bhatia and Singh [34-35], is applied to describe the thermodynamic properties of a compound forming alloys.

By using method QCA, the thermodynamics of mixing in liquid state of frequently used alloys, namely Co–Cr, Cr–Ni and Co–Ni has been analyzed [36]. The normalized *Gibbs free energy* of mixing $\Delta G_M/RT$ for the alloys liquid system, calculated for $T = 1873$ K is depicted in Fig. 3. The alloys Co-Cr shows a

minimum $\Delta G_M/RT = -0.83$ for concentration of Cr equal to $C_{Cr} = 0.5$. It means that the tendency of a compound formation in the Co–Cr liquid phase is weak. The systems Cr–Ni and Co–Ni are also shown and the values of $\Delta G_M/RT > -1$ indicating a weak interaction. The authors found however that the system Cr–Ni forms a compound while the system Co–Ni is segregating.

(Fig. 3)

Fig. 3 Concentration dependence of normalized Gibbs energy for mixing, $\Delta G_m/RT$, for liquid Co–Cr, Cr–Ni and Co–Ni alloys at $T = 1873$ K [36].

For the Co–Fe liquid alloy, the minimum value of normalized free energy of mixing was calculated to be $\Delta G_M/RT = -0.63$ what was in good agreement with experiment results being equal to $\Delta G_M/RT = -0.61$ [37]. The energy for Fe–Si alloys in molten state at 1873 K, given by theory and by experiment methods, analyzed by Adhikari *et al.* [38] is shown in Fig. 4. The minimum value of this energy is equal to -2.31 is reached for the concentration of $C_{Fe} = 0.55$. The calculation of free energy of mixing shows that Fe–Si is a strongly interacting system in liquid state.

Fig. 4. Concentration dependence of normalized Gibbs energy for mixing, $\Delta G_m/RT$, for liquid Fe–Si at temperature of 1873K (–) theory and (o) experimental points [38]. Reproduced with permission.

Thermodynamics of MMCs can be studied using *Ellingham diagrams*. The diagrams are used to predict equilibrium temperatures for metals and oxygen and, similarly, for metal and carbon or metal and nitrogen. The *Ellingham diagrams* represent graphically the **standard free enthalpy of oxidation**, ΔG , in function of temperature. The feasibility of a reaction depends on the sign of ΔG and more negative value indicates more favorable thermodynamic conditions for metal reaction with oxygen, nitrogen or carbon.

An interesting MMC is iron reinforced with titanium carbide. Fig. 5 shows a phase diagram of Fe–Ti–C system. It can be observed that at the temperature higher than $T > 1400$ °C, there a solid phase of TiC coexists with liquid.

(Fig. 5)

Fig. 5 Phase diagram of the system Fe–Ti–C from Emanian *et al.* [10]. Reproduced with permission.

Thermodynamics of Fe–Ti–C system was studied e.g. by Jonsson [39]. The possible reactions in the Fe–Ti–V–C system between Ti and C, V with C, Fe with –Ti and Fe with C associated with standard free energy changes are shown in Table 5

Table 5

Main chemical reaction in the Fe-Ti-V-C system after Wang *et al.* [40]. Reproduced with permission.

The data from Table 5 enabled to create the *Ellingham diagram* for the system Fe-Ti-V-C (see Fig. 6). The values of Gibbs free enthalpy are negative at high temperature occurring e.g. at arc or laser cladding processes. The diagram indicates that TiC and VC are stable carbides.

(Fig.6)

Fig. 6 Ellingham diagram for system Fe-Ti-V-C created using data from Table 5.

The *liquidus* of a ternary phase diagram of Fe-Ti-C system is showed in Fig. 7. The diagram visualizes the influence of increasing *liquidus* temperature resulting from an increase of C and Ti content. The figure shows that the increase of C and Ti atomic percentage and decreasing the Fe one results in an increase of the *liquidus* temperature. At lower temperatures the phases remain in semi-solid state.

(Fig. 7)

Fig. 7 Liquidus section of Fe-Ti-C diagram with isotherms [39]. Reproduced with permission.

2.2.2. Surface energy

The properties of final coatings obtained by *hardfacing* are closely related to the properties of liquid metals (alloys) and to the phenomena occurring at processing at the interface between these liquids and solid reinforcements. The *surface energy* of liquids is an important thermodynamic parameter which can be found directly from the *Gibbs energy*. The *surface tension* (γ) of some pure metals are presented in the Table 6.

Table 6

Surface tension of some pure metals at the melting point [41].

The *surface tensions* of molten Ni-(Cr, Co, W) binary alloys were found experimentally vs. temperatures in the range of 1500 – 1600 °C are represented in the Fig. 8

(Fig. 8)

Fig. 8. Surface tension of molten Ni with Cr, Co, and W binary alloys in function of temperature [42].

Reproduced with permission.

The surface tension of these molten alloys decreases with increasing temperature. Feng *et al.* [42] measured surface tension in Ni with Cr, Co, and W binary alloys. The authors found out that, under controlled (Ar+ 3 vol. % H₂) atmosphere, the elements with lower surface tension separate rather on the surface of molten alloy contrary to the elements with higher surface tension, which separate rather inside it. Consequently, Cr separates onto the liquid surface and Co and W - inside the alloys. The melting under uncontrolled atmosphere may lead to adsorption of oxygen what leads to decrease of surface energy [2]. It should be added that it is difficult to determine experimentally the surface tension of liquid metals and alloys and that the theoretical models are frequently used to estimate this parameter.

2.2.3. Volumetric thermal expansion

Volumetric thermal expansion describes the increase of liquids' volume with temperature. At a constant pressure, the volumetric thermal expansion coefficient α_V can be defined as:

$$\alpha_V = \frac{1}{V} \left(\frac{\partial V}{\partial T} \right)_P \quad \text{Eq. 1}$$

Generally, the coefficient increases with temperature. Fig. 9 shows the volumetric thermal expansion coefficient for liquid Ni comparing with that of solid Ni. Fig. 10 shows the coefficient for Ni₃Al alloy.

(Fig. 9)

Fig. 9 Volumetric thermal expansion coefficient of Ni [43]. Reproduced with permission.

(Fig. 10)

Fig. 10 Volumetric thermal expansion coefficient of Ni₃Al [44-45]. Reproduced with permission.

Finally, Fig. 11 shows the volumetric thermal expansion coefficient for liquid Ni-Cu-Fe alloy having fixed composition of Fe and Cu and increasing content of Ni.

(Fig. 11)

Fig. 11 Volumetric thermal expansion coefficient of liquid Ni-Cu-Fe alloy versus Ni content [46]. Reproduced with permission.

2.3. Diffusion in liquid phase

Diffusion is the movement of molecules or atoms from a region of high concentration to the one of low concentration. It is driven by the concentration gradients. The study of diffusion processes in liquids helps to understand nucleation and crystal growth [47]. Diffusion coefficient is an important parameter characterizing the diffusion. The diffusion depends on temperature as shows it the **Arrhenius relation** (Eq.2). This equation was used by e.g. Ejima and Yamamura [48] to describe diffusion of impurities in liquid Al and Cu. Their experiments were carried out at temperatures being 200 K above the melting point temperature of the metals.

$$D=D_0 \exp(-Q/kT) \quad \text{Eq. 2}$$

2.3.1. Diffusion of carbon

Carbon atoms diffuse easily into metals such as Fe, Ni, and Mo. The diffusivity of carbon in austenite was first determined by Smith [49] using the steady-state method. The coefficients of carbon diffusion in a wide range of concentration were determined by measuring the flux and carbon concentration profiles in many studies [50-51]. It was shown the carbon diffusion coefficient is not significantly influenced by the small quantities alloying elements, such as Cr or Si [52].

The temperature dependence of the diffusion coefficient of carbon in α -Fe and in austenite is given in Table 7 [53-54] and in Co [55]. The diffusion coefficient of carbon in liquid iron at 1 823 K is ranging from 6.7 to 7.9 x 10⁻⁹ m²/s depending on initial carbon content in iron [54]. It must be underlined the poor affinity of C to Ni leads leading to a gradient of carbon concentration in Ni-alloys [50, 52].

Table 7

Carbon diffusion coefficient in iron and austenite [53-54].

2.3.2. Diffusion of nitrogen

The studies of the diffusion of nitrogen in liquid iron and liquid iron-base alloys has been reported in many papers. The diffusivity of nitrogen in liquid iron having low concentration of carbon was determined using such experimental methods as [56-60]:

- unsteady state gas-liquid metal cell technique;
- quenching technique at temperature of 1873 K;
- capillary reservoir method at temperatures 1823 K to 1953 K;

- steady state technique at the temperatures ranging between 1823 K and 1973 K.

Lee and Parlee [61-62] measured the absorption of nitrogen in Fe-containing liquid systems at the temperature of 1873 K under pressure of nitrogen of 10^5 Pa. The authors studied the effect of alloying elements on diffusion coefficient. It was found that the nitrogen diffusivity increases significantly with additions (above 10 wt. %) of such elements as of Si, Al, Co, Ni, W and Sn. The additions of Mn results also in an increase of nitrogen diffusivity of nitrogen but to a less extent [57]. On the contrary, the additions of V and Nb result in decrease the nitrogen diffusivity. No effects on the diffusion were observed by addition of Cr and Mo.

The rates of nitrogen absorption in the Fe-Ni and Fe-Co liquid alloys were studied by Benner and Parlee [63]. Kojima *et al.* [64] determined diffusion coefficients of Fe-alloys with Ni and Co at 1600°C. Some literatures values of diffusion coefficients of N in liquid Fe and in low carbon Fe-alloys are collected in Table 8. The values of nitrogen diffusion coefficients in the iron alloyed with different metals was studied by Villegas [57] and is shown in Table 9.

Table 8

Diffusion coefficients of N in liquid Fe and low carbon Fe-alloys [57, 59-60, 65-67]

Table 9

Experimental values of diffusion coefficient of N in the alloys including iron with other metals noted as X and Y at 1600 °C. The content of other metals is 2.5% X and 2.5% Y [57].

2.3.3. Diffusion of oxygen

Saiz *et al.* [68] used scanning electron microscopy (SEM) and atomic force microscopy (AFM) to observe the phenomena at the interface between liquid metals (Ni, Cu, Au, Al) and polycrystalline alumina including the diffusion of oxygen. This diffusion in liquid iron was measured experimentally under the pressures ranging between 3 and 18 GPa at the temperature ranging from 1973–2643 K [69]. The diffusion coefficient was in the range from 6×10^{-9} to $2 \times 10^{-8} \text{ m}^2\text{s}^{-1}$ and activation enthalpy was lower than 100 kJ mol^{-1} . The results obtained by Otsuka and Kozuka [70], who found the oxygen diffusivities in liquid nickel and iron by using an electrochemical method are shown in Table 10.

Table 10

Diffusivity of oxygen in liquid nickel and iron [70].

2.4. *Surface tension* of metals in liquid phase

The liquid metals and alloys occurring at the processes of *hardfacing* can be characterized by *surface tension*. This parameters at the melting point are collected in Table 11

Table 11

Surface tension of metals at melting point [71].

3. Physical properties of oxides and carbides used for composites reinforcements

Some properties important for composite reinforcements, such as Young modulus, hardness, melting temperature, standard enthalpy of formation for oxides are collected in Table 12. The described oxides are used as reinforcement include alumina, zirconia, yttria, and ceria. The properties of carbides of tungsten, titanium, chromium, boron, vanadium, and molybdenum are shown in Table 13.

Table 12

Physical properties of typical oxides [11]

Table 13

Physical properties of typical carbides [11]

4. Interface between ceramics and liquid metals and alloys

The principal phenomena occurring in contact between ceramic reinforcement and liquid metal (alloy) matrix are shortly described. The phenomena include mainly the different aspects of wetting.

4.1. Fundamentals of wetting

The wetting phenomena description presented in the section is very elementary. More careful description of wetting at high temperatures may be found in many studies synthesized by Estathopoulos *et al.* [2].

4.1.1. *Non-reactive wetting*

The fundamental energy balance of liquid, solid and vapor phase can be represented graphically as a liquid droplet being in contact with surrounding vapors and with a solid surface (see Fig. 12). The contact area between solid and liquid is supposed to not include the reacting species. The essential parameter of contact is the angle of wetting, θ . The wetting can be categorized in a

simplified way using this angle as [2]: (i) perfect wetting for $\theta = 0^\circ$; (ii) wetting for $0^\circ < \theta < 90^\circ$; and, (iii) no wetting for $90^\circ \leq \theta \leq 180^\circ$.

Fig. 12

Fig. 12 Energy balance and the contact angle corresponding to *Young-Dupré equation*.

Oxide ceramics have electronic structures very different from that of metals [72-73]. Electrons are free in metals while in oxide ceramics they are ion-bound and localized in the crystal lattice. Differences in electronic structures appear at the interface between ceramic and metal. Their thermodynamic expression is Gibbs free energy which modification resulting from a contact between two different materials is given by following equation [74-75]:

$$\Delta G_f^{Int} = \sigma_{SV} + \sigma_{LV} - \sigma_{SL} + \Delta G_{ch} + \Delta G_{pd} \quad \text{Eq. 3}$$

Two terms of this equation should be explained. The *free enthalpy* of plastic deformation, ΔG_{pd} , appears in a case of a collapse of liquid droplet with a solid substrate and the enthalpy of chemical reaction ΔG_{ch} is at its minimum at thermodynamic equilibrium [72]. In the case of *hardfacing* processes there is no plastic mechanical deformation. For discussed case of non-reactive wetting, the *Gibbs free energy* ΔG_f^{Int} is equal to the surface adhesion work, W_a . The latter the sum of the surface energies between solid, liquid and vapor phase as shows it the well-known equation:

$$W_a = \sigma_{SV} + \sigma_{LV} - \sigma_{SL} \quad \text{Eq. 4}$$

The equation can be also re-formulated by taking the angle of wetting, θ (see Fig. 12) into account as, well-known, *Young–Dupré law* [2]:

$$\cos\theta = \frac{W_a}{\sigma_{LV}} - 1 = \frac{\sigma_{SV} - \sigma_{SL}}{\sigma_{LV}} \quad \text{Eq. 5}$$

Young's-Dupré law says that the contact angle between the liquid droplet and the solid substrate results from the equilibrium between the surface energies of liquid and solid phases ($\sigma_{SV} - \sigma_{SL}$) and from the cohesion force of the liquid σ_{LV} . Liquid metals have high cohesion forces and if the surface energy between liquid and solid phase is also high, $\cos\theta$ may be close to unity. The *Young-Dupré's law* can then be re-written as (see Dezellus and Estathopoulos [72]):

$$W_a = \sigma_{SV} + \sigma_{LV} - \sigma_{SL} = \sigma_{LV}(1 + \cos\theta) \quad \text{Eq. 6}$$

Lawrence [76] indicates that the work of adhesion W_a can be also expressed as the sum of the contributions of interfacial interactions between the two phases:

$$W_a = W_{cheq} + W_{VDW} + W_{neq} \quad \text{Eq. 7}$$

W_{neq} represents the contributions to the energy of adhesion resulting from chemical reactions taking place at the metal-ceramic interface and W_{cheq} is the cohesive energy between two phases in contact resulting from the establishing of a chemical equilibrium. Finally, W_{VDW} represents the energy resulting from *van der Waals* forces.

4.1.2. Wetting between metals or alloys and carbides

The analysis of Li [77] showed that the adhesion energy of non-reactive liquid metals to metal carbides is a function of the concentration of valence electrons in both metal and carbide. Consequently, this adhesion energy of different metals to TiC increases linearly with the increase of the electron density on the boundary of the **Wigner-Seitz cell**¹ of metals in contact. Li's approach shows that the interactions between metals and carbides is similar to that between the metals because of the overlap of the valence electrons at the interface. Another paper of Li [78] generalizes his analysis for the case of contact between liquid metals and ion-covalent solids. Table 14 shows a good wetting ($\theta \ll 90^\circ$) by non-reactive liquid metals in contact with metals, semiconductors and ceramics with metallic behavior.

Table 14

Wetting by non-reactive liquid metals (after Dezellus and Eustathopoulos [79])

Similar behavior has the contact between liquid metals and the semiconductors such as SiC [80]. This results from that fact that the semiconductors behave as metals at their surface. Liquid metals wet well the metal carbides, nitrides and borides because metallic character bonding of these materials [81-82]. The solids which are not well wetted by the liquid metals are: (i) carbon; (ii) ion-covalent oxides; and, (iii) the covalent ceramics which have a large electronic gap, such as BN or AlN [83-84]. More examples are shown in Table 14.

¹ The Wigner-Seitz mesh is an elemental mesh. The *Wigner-Seitz mesh* corresponds to the first Brillouin zone in the reciprocal space

4.1.3. *Wetting between metals or alloys and oxides*

The liquid metals and alloys do not wet well oxide ceramics. It must be also underlined that ceramics such as SiC and Si₃N₄, and a lot of solid metals such as e.g. stainless steels, *superalloys*, and alloys containing Al are frequently oxidized on their surface. The oxidation layer modifies their wetting behavior [85-86].

4.2. Reactive wetting

Saiz *et al.* [87] suggested that the reactive wetting results from adsorption at the initial liquid-solid interface of a reactive alloying element while the kinetics of the spreading would be governed by the migration of a ridge formed at the solid-liquid-vapor line. This hypothesis was not confirmed experimentally [88]. A model of interfacial reaction resulting in a formation of an intermediate layer was proposed by Landry and Eustathopoulos [89].

4.2.1. *Dissolutive wetting*

Dissolutive wetting occurs when a dissolution of solid in liquid takes place. The dissolution is accompanied by formation of an interface having dendritic microstructure [88-89]. It occurs frequently at solidification of metals [90-91]. The dissolutive wetting was reported to occur in contact of Ni/C [89], Ni/HfB₂ [92] and AuNi/ZrB₂ [93].

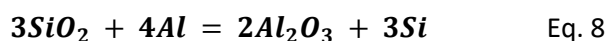
4.2.2. *Local reaction at contact*

The chemical reaction at contact between liquid and solid may result in formation of compounds which may constitute the wetting barriers. For example, liquid Au does not wet TiC, the contact angle is equal to $\theta = 130^\circ$ being the same as that of gold on the carbon substrate [94]. This results from small solubility of carbon in gold which precipitates without any reaction. To improve this solubility a small addition of nickel is useful. Consequently, adding of 3% to 7% nickel to gold, enabled obtaining contact angles in the range of $60^\circ < \theta < 80^\circ$.

Similarly, in the liquid Ag /SiC system the dissolution of silicon in silver causes the precipitation at the interface of graphite which is not wetted by Ag. With the addition of Si to Ag, the carbon precipitation is suppressed, and good wetting was observed [95]. Similarly, a CuSi alloy did not wet an oxidized (in form of a thin silica layer) SiC substrate. However, the reaction between silicon and silica resulted in formation of the volatile SiO. The latter removed the oxide layer what resulted in a good wetting [96].

4.2.3. Examples of wetting between metals or alloys and oxides

Generally, the metals are covered with a few nanometers thin layer of metal oxide formed in contact with the air at room temperature. The oxides are not well wetted by the liquid metals [97-98]. Consequently, in order to improve the wettability, it is necessary to find for reactions enabling formation of intermetallic film which may replace the oxide layer. Zhou and De Hosson [99] measured contact angles of contact between liquid Al and solid SiO₂ and of liquid Ti with solid Al₂O₃. The authors found out that the change of ceramic substrate volume at reactive wetting may be significant. It was observed at Al liquid contacting solid SiO₂ in which the reaction following reaction takes place:



The volume of ceramic substrate initially decreased because of formation of Al₂O₃ (see Eq. 8). On the other hand, the wettability increased after reaction. Similar effect was observed at the contact between liquid Ti and solid Al₂O₃ substrate. A dense layer of titanium-aluminum mixed oxide was formed at the solid-liquid interface what improved the wetting.

5. Modern methods of *hardfacing*

The methods of coatings manufacturing by *hardfacing* may be also called ***bulk coatings*** because of great quantity of material deposited [3]. The well-known examples of *bulk coatings* manufacturing are painting or printing. A group of *bulk coatings* discussed in this review is characterized by a local melting of a substrate and by the introduction into the melt-pool of material contributing in coating formation in the form of a powder or wire. In a case of a composite coating deposition, the introduced feedstock may be:

- mixture of metal/alloy with ceramic in a form of powder or wire which form a composite;
- ceramic powder forming a composite with a metal into a molten pool of substrate.

Another possibility is the use of a composite wire containing the mixture of metal/alloys and ceramics being an electrode which is molten by arc at processing. The arc is also melting the coated substrate and the molten droplets of composite form a coating welded to a substrate (see Fig. 13). Such a coating technique is known as arc welding [100].

Fig. 13

Fig. 13 The composite wire electrode for arc welding a) and microstructure of coating b) [100]. Reproduced by permission

Finally, the powders may be pre-placed as a coating before the heat treatment. This method is well adapted to a laser heat treatment and was used to obtain MMC coating e.g. in the studies [101-103]. The plasma and flame heat treatment are less appropriate being associated with gas movement which may displace pre-deposited powder. The displacement can be avoided by gluing of pre-placed powders with an organic binder to the substrate e.g. with epoxy resin. However, the use of organic binder may increase the electrical conductivity of pre-placed powder which should be low in the PTA process.

The formation of melt-pool in a substrate can be realized using:

- combustion flame;
- arc and plasma;
- laser.

Since the interface between the substrate and the deposit results from the dilution of a liquid phases of substrate with that of coating (Fig. 14), this family of coatings is often called **deposits by welding**. The dilution, defined in Fig. 14, is an important parameter of such deposition process. In general, one seeks to obtain deposits with a dilution of a few percent. This is however difficult to reach, and the dilution values are generally in the range from 10 to 40% [104].

Fig. 14

Fig. 14. Dilution in a *bulk coating*: A, zone of a solution of substrate with coating; B, coating; C, heat affected zone (HAZ)

The technique in which the substrate is melted by the oxyacetylene combustion flame is least efficient² because of low melting capacity of a substrate by the flame. The resulting dilution is rather small. Better coatings' efficiency can be achieved by applying an electrical arc between the substrate and a non-consumable tungsten electrode (TIG process) or a consumable electrode (MIG process). These techniques are described elsewhere [7, 104]. Plasma may be used for the non-transferred arc melting of a substrate in a process called plasma cladding described by e.g. Guozhi *et al.* [105]. More frequently, plasma is used as with transferred arc (the anode being a substrate), being a very efficient way of melting the substrate surface. The dilution depends on the operational parameters. The statistical study carried out by Balasubramanian *et al.* [106] for PTA technique enabled to find out that the dilution depends mainly on: (i) transferred arc current; (ii) travel speed; (iii) powder feed rate; (iv) oscillation frequency, and; (v) distance between torch and substrate. The greatest influence has travel speed and the lowest one – the powder feed rate. The composite coating formed on the top of dilution zone may have one of three possible morphologies, described for carbides reinforcement MMC deposited onto aluminum substrate, by Deuis *et al.* [8] and shown in Fig. 15:

- particles dispersed composite layer is formed in fusion zone (Fig. 15a);
- compound layer is formed in upper part of fusion zone (Fig. 15b);
- composite layer is not formed (Fig. 15c).

(Fig.15)

Fig. 15 Possible morphologies of MMC coatings obtained by *hardfacing*, see description in the text (inspired by [8]).

5.1. Plasma Transferred Arc (PTA)

The principle of PTA coatings is shown in Fig. 16. The "pilot" arc is initiated between the cathode of thoriated tungsten and copper anode, cooled by water. This arc heats the plasma gas which is typically argon. Then, the torch is approached to the substrate and the transferred arc is ignited between the cathode and the anode-substrate. This arc melts locally the substrate. The powder is introduced into the melt-pool to create the deposit. The pool is protected against the influence of ambient atmosphere by an inert gas such as argon [107].

(Fig.16)

² Coating efficiency is understood as coating thickness obtained in one pass of a torch

Fig. 16 - Diagram of PTA processes: 1, plasma gas; 2, injection of powder with a carrier gas; 3, protective gas; 4, cathode; 5, anode; 6, substrate.

The MMC can be formed with the use of powder mixture or using separate injectors of powder of matrix and powder of ceramic reinforcement. In the latter, the powders can be fed by two powder feeders described by Zikin *et al.* [108]. The quality of coatings obtained by PTA depends mainly on the following elements of coating's processes after Demian *et al.* [109]:

- torch (pilot arc current, transferred arc current, plasma gas flow rate, shielding gas flow rate);
- powder (chemistry, granulometry, particles velocity resulting from carrier gas flow rate);
- torch position with respect to the substrate (oscillation, stand-off, overlapping of the following deposition paths).

The PTA process can be also categorized in function of deposition rate in the following groups [104]:

- micro plasma transferred arc (MPTA) with low powder feed rate, low dilution and coatings thickness up to 1.5 mm;
- standard PTA described in present paragraph;
- high power plasma transferred arc characterized by a very high deposition rate ranging from 200 to 250 g/min.

The typical industrial torch is powered electrically with 3 to 10 kW and the gas flow rates are relatively low [3]. An example of flow rates used to spray NiCrAlY – YSZ cermets is: (i) Ar plasma gas of 1.4 slpm; (ii) Ar+ H₂ shielding gas of 14 slpm; and, (iii) carrier gas of 3.5 slpm. The dilution of a coating depends on the ratio between the pilot arc current and the transferred arc current. A small transferred arc current results in a small dilution and a large pilot arc current ensures good heating of the particles before contact with the substrate. An example for deposition of NiAl alloy the pilot arc current of 45 A and the transferred arc of 80 A [110]. The powder applied in the PTA process has the particle sizes ranging typically from 40 to 150 μm. The particle sizes can be much more dispersed than that used in the thermal spraying processes. This results from a double mechanism of particles melting in PTA, including: (i) convection in pilot arc plasma; and, (ii) conduction in the melt pool created by the transferred arc. The convection melting in the plasma jet is much less important and mainly melting by conduction counts. The powder feed rates vary between a few tenths and a few

hundreds of g/min. The torch is subjected to two movements relative to the substrate: (i) translation (scan speed is typically equal to a few cm/min); and, ii) oscillations with an amplitude of about ten mm and its frequency about 40 to 100 mn^{-1} [109-110]. The stand-off between torch and substrate is as small as 6 to 8 cm [108 - 111] to keep the transferred arc ignited. Some processing parameters influencing the coatings quality may be reduced to one parameter. Consequently, Demian *et al.* [109] proposed a factor of deposition, Q , depending on electric power delivered to arc, P , torch scan speed, U , and powder feed rate, q . The factor is defined as:

$$Q = \frac{P}{Uq} \quad \text{Eq. 9}$$

The PTA coatings are formed in a few passes of a torch (see Fig. 17) and it is often necessary to rectify them before service.

(Fig. 17)

Fig. 17 Coating deposition by plasma cladding with a torch produced by *Saint Gobain Coating Solution, Avignon, France* (presented with the permission).

5.2. Laser assisted methods

The laser deposits can be obtained in two processes called: (i) one-step laser deposition (1SLD); and (ii) two-steps laser deposition (2SLD). The 1SLD process, similarly to PTA, consists of melting the substrate by a laser and injecting powder into a molten pool. Another possibility is to make a pre-deposit with another coatings' deposition technique (typically thermal spraying) and, later on, to perform a laser treatment. This technique can be called a two-steps laser deposition (2SLD). These two techniques can be further differentiated into the following methods (see also Fig. 18):

- *cladding*, in which the deposits are chemically different from the substrate;
- ***laser surface alloying*** (LSA), in which the materials of the deposit and the substrate form an alloy at processing;
- ***hard phase dispersion***, in which solid particles of a reinforcement are injected into the pool and remain solid.

Another emerging method is called ***laser prototyping*** and consists of injecting of small quantity of powder to be melted into a melt pool created by laser beam. The laser prototyping is a part of ***additive manufacturing*** method and to create the 3D objects from fine powder.

(Fig. 18)

Fig. 18 - The laser assisted coatings processes: *cladding, alloying and hard phase dispersion*.

The laser deposits are mainly made using four types of lasers: CO₂, Nd: YAG, diode laser, and fiber laser. The diode and fiber lasers applications grow rapidly in *hardfacing* industry. The main properties of these lasers are collected in Table 15.

Table 15

Selected characteristics of industrial lasers applied in laser assisted deposition coatings methods [112-115].

The most important parameter of laser processing is power density, defined, for a continuous wave laser, as:

$$q = \frac{P}{A} \quad \text{Eq. 10}$$

The power density for a pulsed laser is defined as:

$$q = \frac{E}{A\tau} \quad \text{Eq.11}$$

Each type of laser treatment requires a different power density. Generally, to melt the solid material, the power density should be in the range 1-10³ W/cm² [116].

6. Cermet coatings obtained by *hardfacing*

The cermet coatings obtained by flame, plasma, as well as, by laser assisted methods are described in the following chapter starting from feedstock and from the process parameters used for processing. Subsequently, it follows a short overview of cermets, categorized by type of ceramic reinforcement and a description of their properties.

6.1. Feedstock used in processing

The feedstock used in cermet cladding using flame, plasma and laser assisted methods is similar and is described in one chapter. The powders are used most frequently as the feedstock. The cermet powders can be:

- made of metal/alloy and ceramics mixed before processing or delivered using two different powder feeders and are separately injected in the molten pool;
- manufactured as cladded powders, having thin metallic layer around ceramic particle, or as composite ones i.e. with metal/alloy particles mixed with the ceramic ones.

Sometimes, rods or fibers are used as a feedstock. In this case, ceramics and metal/alloy powders are sintered initially to a form of rod or wire.

The size of metal/alloy and carbides powders being mixed or separately delivered was discussed by Deuis *et al.* [8]. The authors underlined the following restrictions concerning the particles used in PTA surfacing:

- size of the matrix particles should be in the range 50-150 μm to avoid the feeding problems and the reinforcement particles should be rather smaller, say 5-20 μm , to achieve better coating strength by ***dispersion-hardening mechanism***;
- morphology of reinforcement particles should be rather spherical or shaped in an angular way and the morphologies of whiskers and fibers are to be avoided because of bad flowability;
- density of reinforcement particles should have similar density to that of the melt pool in order to avoid particles falling to the bottom of the melt pool.

The typical powders and wires used in metallic matrix composited are shown in Table 16.

Table 16

Cermet powders and wires used for plasma/ flame and laser cladding after [117-121]

The metallic matrices are often the Ni- based and Co-based alloys and ceramic reinforcements are oxides, carbides or cermets (see Table 16). The use of cermet reinforcement results from the recycling of powders and the size of cermet powder is much greater than the other reinforcement powders. Generally, the sizes of matrix powders are generally greater than that of reinforcement. Another possibility, shown by Emamian *et al.* [122-123], is a formation of the reinforcement at coating process. These authors injected into a melt-pool formed by fiber laser, the mixture of powders having size about 40 μm : iron, titanium and graphite. The processing, called ***laser assisted powders deposition*** (LAPD), enabled formation of TiC reinforcement having size of a few micrometers and shape depending on deposition parameters by following reaction:

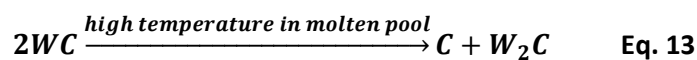


The process parameters, such as feeding rate, influenced chemical composition and laser power energy influenced the melt-pool temperature. TiC morphology were influenced by chemical composition of used feedstock and by the temperature of particles. The chemical composition of the pool including solid TiC particles is shown in Fig. 19.

Fig. 19

Fig. 19 The evolution of chemical composition of Fe, Ti and graphite particles at laser cladding: initial powders, a); melting and dissolution of Ti powder leading to the formation of TiC, b); increase of TiC particles size, c) [122]. Reproduced with permission.

An important factor is related to capturing of reinforcement by the melt-pool formed by metallic matrix. The ratio of captured powder was estimated by Abioye *et al.* [121] on 24 to 42 % while injecting WC-W₂C powder to the melt pool formed by *Inconel* 625 alloy. Consequently, the feedstock feed rates should take the capturing into account. The free carbon atoms may come from the reaction of reduction in molten pool. Liu *et al.* [124] observed the reduction of cast WC powder to W₂C:



The free carbon atoms did enter in reaction, described by reaction shown Eq. 12, with Ti being present in the pool because of melting Ti6Al4V alloy substrate.

Nanostructured feedstock was discussed by Dubenskaia *et al.* [125] and Duan *et al.* [126]. Dubenskaja and her co-authors used nanostructured cermet WC-Co and WC-Co-BN produced by mechano-chemical alloying with the particles size of 56 μm for WC-Co and 28 μm for WC-Co-BN. The sizes of WC crystals were equal to 13 nm for both powders. The authors used them for cladding with the Yb fiber laser. Duan with colleagues clad a cermet powder Fe-Cr-Mo having composition (Fe, bal. +15 wt. % Cr+1 wt. % Mo) and size of 70 to 150 μm with 5 to 10 wt. % of Al₂O₃ having sizes in micrometer (from 20 to 70 μm) and in nanometers range (less than 100 nm). The cladding was made using CO₂ laser. The powders were mechanically mixed before being preplaced on a substrate. The behavior of Al₂O₃ powder particles in molten pool depended on their size as discussed in the next section. The technology of cladding by laser glazing of initially deposited FeCr-TiC cermet was described by e.g. Pawłowski and Smurov [127].

Cladded powders may be manufactured by covering the core particle with a layer of different material. The cladding of powders may be realized in solid, liquid and gas phases. The possible structures of layers applied on powders particles are shown in Fig. 20.

(Fig. 20)

Fig. 20 External layers of cladded powder particle obtained using different technologies [112].

The ceramic cores may be coated with metallic layers what may to (i) improve the wetting inside the molten pool; and, (ii) avoid the agglomerations of ceramic particles. It is also possible to manufacture the powder particles very fine. An example of such nanostructured particle in which a ceramic core of YSZ is coated with Ni is shown in Fig. 21. The particles, produced by electroless plating, are not only nanostructured but also nano-sized with a size of about 100 nm [128].

(Fig. 21)

Fig. 21- TEM image of nano-sized powder particle of YSZ core coated by Ni [128]. Reproduced with permission.

6.2. Phenomena in melt-pool

The intensive interactions between molten alloys or metals and ceramic reinforcement take place in melt-pool during very short time. That is why; a careful description of physical and chemical phenomena occurring in melt pool is necessary. The melt-pool may be formed by: (i) electric arc heating; (ii) convective heating of plasma, flame; or, (iii) radiative heating of laser.

6.2.1. Physical phenomena

To simplify the description, one can imagine a liquid with cold surface and hot bottom part. The convection movement, known as **Rayleigh - Bénard convection**, will take place in such a liquid. The mechanism this movement was discussed by Kadanoff [129].

As the molten fluid has a free surface, the fluctuation of the temperature of the surface resulting from the colder fluid arriving from the bottom part and from the evaporation at the surface influences the surface tension. The gradients of surface tension create the forces moving the fluid and deforming its surface (see Fig. 22). This effect is called also **Bénard - Marangoni convection** being a form of *Rayleigh-Bénard convection* for melted liquid with free surface.

(Fig.22)

Fig. 22 - Movements of liquid in a melt-pool with a cold free surface

The formation of melt-pool by plasma or laser and its solidification, resulting from the heat source movement, occurs in a very short period. The modeling of 2SLD process including CO₂ laser heating of FeCr-TiC cermet pre-deposited by plasma spraying made by Pawłowski and Smurov [127] shows the heating and cooling rates of melt-pool being equal to about 10⁴ K/s (see Fig. 23).

(Fig. 23)

Fig. 23 -Evolution in time of spot center temperature at laser heating and cooling of FeCr-TiC plasma sprayed cermet coatings for different laser scan speeds [127].

Cladding with plasma or laser may be associated with injection of powder in a coaxial way, i.e. under angle 90° with regards to the melt-pool surface, as discussed by Kumar and Roy [130]. The injection under an acute angle was discussed by Fallah *et al.* [131]. The sketch of laser cladding with coaxial injection is shown in Fig. 24 and the profiles of obtained iron coating are shown in Fig. 25.

(Fig. 24)

Fig. 24 - Schema of coaxial powder injection in laser cladding process [131]. Reproduced with permission.

(Fig.25)

Fig. 25 - View of melt-pool at iron coating build up using laser cladding for geometry shown in Fig. 19: a) section, and b) view from the top.

The shape of melt-pool is hemispherical, and it becomes greater and more conical with increasing thermal energy input and/or with lower scan speed. This is well visualized for stationary fiber laser interactions with stainless steel AISI 304 when laser power increases (see Fig. 26).

(Fig. 26)

Fig. 26 - The simulated and experimental melt-pools cross sections generated by a fiber laser in AISI 304 stainless steel for laser power of 500 W during 1 s a) and of 750 W acting during 0.6 s. b) [132]. Reproduced with permission.

The cross-section of melt-pool visible in Fig. 26 enables estimation of its volume on a few mm³. This is the volume to which are injected the ceramic particles being the reinforcement of MMC. On the other hand, the particles injected to the melt-pool have a size ranging from a few tenths of μm up to a few hundreds of μm (see Table 16).

The optimal composite coatings have the reinforcement particles distributed evenly. An example of such distribution in laser deposited composite with WC+W₂C reinforcement and Inconel 525 alloy matrix is shown in Fig. 27.

(Fig. 27)

Fig. 27 - SEM micrograph (back-scattered electrons) showing cross-sections of laser clad MMC with WC+W₂C reinforcement having mean size of 125 μm and Inconel 625 alloy matrix obtained using different laser energy density and constant feedstock feed rates [121].

Reproduced with permission.

An example of uneven reinforcement particles' distribution in melt-pool is shown in Fig. 28. The WC reinforcement having size about 50 μm³ was unevenly distributed in Ti6Al4V alloy matrix. Some agglomerations of reinforcement particles are visible.

(Fig.28)

Fig. 28 - SEM micrograph of MMC obtained by PTA using WC reinforcement and Ti5Al4V alloy matrix for different arc currents: a) 70 A, b) 80 A, and c) 90A [133]. Reproduced with permission.

The distribution of the WC reinforcement particles, in the discussed PTA process, could have been improved by optimization of powder feed rate and of flow rate of powder-carried gas. On the other hand, the agglomeration of 30 wt. % of 13YSZ reinforcement particles in the NiCrAlY alloy matrix shown in Fig. 29 resulted most probably from the poor wetting of solid oxides inside by molten alloy.

(Fig.29)

Fig. 29 - SEM micrographs of MMC having 30 wt. % of 13YSZ reinforcement of size -45+22 μm in the NiCrAlY matrix [109].

³ The authors wrote 280 mesh what was probably an error and the real value was 230 mesh corresponding to 63 μm.

The wetting effect was discussed by the authors of study [109] to explain the formation of agglomerated islands in the MMC coating in which micro-sized 13YSZ oxide particles were used. On the other hand, the use of nanosized Al_2O_3 reinforcement in MMC coating formed by laser cladding using FeCrMo matrix resulted in better homogeneity of reinforcement distribution in comparison to the similar composite the micro-sized Al_2O_3 [126]. The authors explain the even distribution of nano-sized powder particles by their large specific area. Another, possible, explanation is such that the nanoparticles may easily follow the convective movement inside the melt-pool. This movement helps in avoiding the agglomeration of oxides to form islands. Moreover, the ceramic reinforcement particles being in contact with melt-pool may get dissolved in the pool what was observed in many studies e.g. [134-135]. The dissolved atoms of C or O enter in reaction with metals present in melt-pool to form carbides or oxides discussed later. On the other hand, the rapid solidification of the phases present in melt-pool results in a formation of dendrites being frequently observed in the MMC coatings (see Fig. 30). The dendrites present in the Figure can be attributed to Fe_2C phase formed by the reaction of carbon dissolved in melt-pool and originating from TiC reinforcement, with Fe atoms originating from the alloy matrix. The Fe_2C phase was observed by XRD analysis in coating only after laser glazing. It was absent in the plasma sprayed pre-deposits [135].

(Fig.30)

Fig. 30 - Optical micrograph of FeCr-TiC cermet cross-section. The coating was obtained by plasma spraying of FeCr-TiC powder followed by CO_2 laser glazing. TiC – titanium carbide, P – porosity and D- dendrites [135].

6.2.2. Chemical phenomena

The atoms available in the melt-pool and reacting with the other atoms may come from liquid metal/alloy matrix and/or from solid reinforcement. The metal atoms have temperature of the melt and their mobility is high. The atoms of carbon or oxygen enter to melt pool from the particles of ceramic reinforcement having higher melting point. Consequently, they diffuse initially through the lattice of solid carbides and oxides before entering to the pool. This diffusion is confirmed by the evacuation of carbon and titanium from the TiC sites. Fouilland-Paille *et al.* [102], who treated pre-deposited TiC powder onto Ti substrate with YAG laser, reported about formation of Ti_{1-x}C phase. This formation resulted from the diffusion of Ti and the formation of vacancies in the lattice. It was also confirmed by the decrease of the lattice parameter of face-centered cubic structure from $a = 0.432$ nm in initial powder to 0.428 nm in the coating. Similarly, the ceramic reinforcement

dissolution in the melt-pool reduced the solid particles' sizes. Such dissolution of Al_2O_3 and TiC grains was observed by e.g. Cai *et al.* [136] and is shown in Fig. 31.

(Fig.31)

Fig. 31 - Evolution of reinforcement particles sizes preplaced on the steel substrate (a), entering in melt-pool (b), cooled after laser source leaved the site (c), and solidifying (d). The symbols correspond to: 1 - Al_2O_3 surrounded by Ti-rich alloy; 2 – Ti rich big ceramic grain; and 3 - Ti -rich small ceramic grain [136]. Reproduced by permission.

The dissolution of ceramic grains started at their sharp edges which were transformed to take more spherical shapes. Diffusion of Al_2O_3 was more intensive than that of TiC. The reaction of atoms leaving solid ceramic particle with that being present in the melt pool occurred near to particles' surfaces. For example, the carbon atoms leaving WC particle reacted with Ti in melt-pool forming TiC compound as shows it Fig. 32.

(Fig.32)

Fig. 32 - SEM micrograph of the reaction zone between the WC reinforcement and Ti atoms produced at laser cladding [126]. Reproduced with permission.

Small reinforcement particles having of a few μm may dissolve entirely in melt-pool. This was reported for the composites including Y_2O_3 particles smaller than 5 μm being a part of reinforcement preplaced on Ti-alloy substrate by Weng *et al.* [137]. Y-atoms introduced to melt-pool did reduce the surface tension and were influencing wetting and growth of another reinforcement of produced composite, namely TiN. Ma *et al.* [138] observed the partial dissolution of large WC particles (size of 100-200 μm) being reinforcement a composite having Ni-alloy including also Cr, Fe, Si, B and C matrix. The obtained composite coatings included many compounds formed at processing:

- carbides such as initial WC and newly formed W_2C , Cr_3C_2 , Cr_{23}C_6 and NiC_x ;
- borides such as Cr_5B_3 and W_2B_5 .

The compounds generated in the melt-pool can be detected using X-ray diffraction of MMC coatings. Their composition may be predicted by considering the possible reactions to occur in the pool by considering the following factors [137]:

- available atoms coming from: molten matrix; dissolution of reinforcement; and, dilution of the substrate;
- diffusion resulting from un-homogeneous distribution of the atoms in the melt-pool;
- *Gibbs free energy* analysis indicating whether a reaction can take place.

6.3. Flame and plasma assisted methods

The microstructures described in the following sections are quite similar for plasma/flame and laser assisted cladded cermets. Some differences result from the size of melt-pool generated by plasma/flame which is greater than that of laser generated. Consequently, the heat flux and the temperature gradients are greater at laser cladding.

6.3.1. Typical microstructure of coatings

An example of a microstructure characterized by a presence of 13YSZ particles inside the melt pool of NiCrAlY shown in Fig. 29 is presented under a higher magnification in Fig. 33. The oxide is not well distributed inside the alloy matrix and form an agglomerated island around alloy particle [109].

(Fig.33)

Fig. 33- SEM micrograph and EDS elemental maps microanalyses of MMC formed by NiCrAlY + 20 wt. % of 13YSZ showing an agglomerated island of oxides around a metal particle [109].

This type of microstructure composed of large islands is typical to cladding with the composites having hard phase which is not well wetted by liquid metal matrix. Generally, the microstructure of metallic matrix is dendritic because of solidification with high cooling rate. The size of dendrites can be modified by addition of different element or compounds. Fan *et al.* [139] reported about modification of plasma cladded self-fluxing Co-based alloy of composition (in wt. %): Co+21 Cr+6 W+3 B+ 2 Ni+ 2 Si by addition of 2 wt. % of Nb and of 1 wt. % of CeO₂. These additives influenced the surface tension of solidifying alloy and did reduce the nucleation energy and the number of nucleating sites. Fig. 34 shows the optical images of modified microstructure.

(Fig.34)

Fig. 34 - Optical micrograph of Co-based plasma cladded coating with addition of a 2 wt. % of Nb; b) 2 wt. % Nb; and, c) 1 wt. % of CeO₂ [139]. Reproduced with permission.

The metallic matrix of a composite including carbides as reinforcement may contain also some carbides formed from carbon atoms dissolved in melt pool. The formation of such carbides as Cr_7C_3 and Cr_{23}C_6 was reported in e.g. PTA composite obtained by cladding of NiCrBSi powders used as matrix with 40 vol. % Cr_3C_2 reinforcement [140]. The microstructure of a clad coating resulted from the distribution of temperature in the melt-pool. The center of the pool had the greatest temperature and the grains of ceramic reinforcement could have been entirely dissolved and formed new phases when solidifying. On the contrary, the reinforcement particles on the periphery of the pool could have preserved their initial form an/or get only partly molten. An example of such behavior is shown in Fig. 35 b. The figure shows strip- or rod-shape grains of carbides or borides formed from FeCrB self-fluxing alloy and B_4C reinforcement being injected in the center of melt pool and having been entirely molten at plasma cladding and precipitated at solidification. On the contrary, the initial shape of B_4C particles was preserved when the powder was injected on melt-pool periphery shown in Fig. 35a.

(Fig. 35)

Fig. 35- SEM micrograph and EDS analysis of: the edge of melt-pool formed at plasma cladding of FeCrB self-fluxing alloy with 18 wt. % of B_4C reinforcement a); and, center of melt-pool b) [141].

Reproduced with permission.

6.3.2. Properties of coatings

The cermet coatings cladded with the help of plasma and flame are mainly applied against different form of wear (adhesive, abrasive, erosive). The properties related to these applications are mainly mechanical ones, namely hardness, modulus of elasticity, and wear resistance. These properties are synthesized in Table 17. The hardness and Young modulus of reinforcement is generally greater than that of matrix (see e.g. lines 1 and 6 of the Table 17).

Table 17

Mechanical properties of plasma/flame cladded cermets [108, 120, 141-145]

This renders the entire composite coating harder and stronger. The improvement of the wear resistance of composites may be explained by the resistance of strong and hard reinforcement against third body wearing the surface. A comparison of wear resistances of a zone without

reinforcement with a zone reinforced with B_4C particles, described in line 3 of Table 17, is shown in Fig. 36.

(Fig. 36)

Fig. 36 - Mechanism of wear resistance of zones without reinforcement a) and zone reinforced with B_4C particles b) [141]. Reproduced with permission.

Wear resistance of composites depends also on the content of reinforcement and on the size of its particles. As shows it Fig. 37, the wear resistance of coating increased with the content of WC reinforcement up to 45 wt. % in the arc welded composite using wires including steel as matrix and WC as reinforcement. The size of the reinforcement grains of 135 μm was optimal to reach the greatest wear resistance.

(Fig. 37)

Fig. 37 - The influence of content of WC reinforcement a) and of size of WC grains on wear resistance, measured using ASTM G65 test method⁴ of composite coatings having matrix of different steels [100] (reproduced with permission).

Some of the composites obtained using PTA technique shown in Table 17 were also tested for their corrosion resistance at high temperature of 973 K [143]. The composite NiCrBSi+40 wt. % Cr_2C_3 (see line 2 of Table 17) was found to be useful against oxidation and action of phosphate ions. NiCrBSi+(TiC+20 wt. % NiMo) composite coating described in line 1 of Table 17 resisted against oxidation. The detailed sketch describing corrosion resistance of different cermets is shown in Fig. 38.

(Fig. 38)

Fig. 38 - Corrosion resistance at 973 K of PTA cermets with NiCrBSi matrix and Cr_2C_3 and TiC (with NiMo) reinforcement against different corroding and oxidizing media after Rojacz *et al.* [146]. Reproduced with permission.

⁴ Standard test method for Measuring Abrasion Using the Dry Sand/Rubber Wheel Apparatus, G 65-04 (1 November 2004)

6.4. Laser assisted methods

The coatings deposited using laser are, generally not very different of that, deposited using plasma and flame. However, the laser assisted methods enable better focusing of energy on the samples' surfaces. Consequently, the microstructure of coatings depends strongly on laser power. For the same laser power, the microstructure and properties would depend strongly on the content of the reinforcement.

6.4.1. Microstructure of coatings

The influence of laser power on the microstructure of laser cladded composite with NiFeCrSiB matrix reinforced by 20 wt. % of WC was tested by Ma *et al.* [138]. The authors observed that the initial size of WC reinforcement decreased from 100 μm in initial powder to 60 μm in the coating while using 3.6 kW of laser power (see Fig. 39 a). Around, the WC grains was formed a eutectic structure composed of the atoms from reinforcement and from matrix. The lowering the laser power down to 3.2 kW resulted in a formation of some blocky precipitates around the WC grains (Fig. 39 b). Finally, at the power of 2.4 kW the WC grains were only slightly dissolved (Fig. 39 c).

(Fig. 39)

Fig. 39 Optical microscope micrographs showing influence of fiber laser power at constant laser scan velocity of 3 mm/s on the microstructure of composite NiFeCrSiB + 20 wt. % WC obtained using laser power of: 3.6 kW a); 3.2 kW b); and 2.4 kW c) [138]. Reproduced with permission.

The influence of the content of WC reinforcement in self-fluxing NiCrBSi matrix in laser cladded composites was studied by Deschuyteneer *et al.* [147]. The authors observed such features as pearls and dendrites resulting from a reaction between Cr phases and WC. The pearls were observed at 10 vol. % of WC (Fig. 40 a) and pearls and dendrites at 30 vol. % WC (Fig. 40 b).

(Fig. 40)

Fig. 40 - SEM micrographs showing, using two different magnifications, evolution of the microstructure of laser cladded NiCrBSi+WC composite with different fraction of reinforcement, namely: 10 vol. % WC a) and 30 vol. % WC b) [147]. Reproduced with permission.

6.4.2. Properties of coatings

The reviewed literature concerning laser clad composite coatings shows mainly the characterizations of mechanical properties such as microhardness, modulus of elasticity and resistance against different kinds of wear. The reinforcements were mainly carbides such as TiC, WC and Cr₂C₃ with the matrixes of Ni and his alloys including the self-fluxing ones, stainless steel and other Fe alloys and Co-based alloys. The mechanical properties of carbides reinforced laser clad alloys are shown in Table 18.

Table 18

Mechanical properties of laser clad cermets [120, 134, 147-150]

The choice of laser cladding parameters influences the mechanical properties. To take an example, the use reinforcement did improve only slightly the hardness of cermet with NiCrBSi matrix (see line 4 of Table 18) for the content of 20 and 30 vol. % of WC. The hardness for the content of 10 vol. % WC was even smaller than that of the matrix. This resulted from the modification of microstructure shown in Fig. 40. Quite similar effect can be observed for the modulus of elasticity. For example, the use of 20 wt. % Cr₂C₃ reinforcement (line 5 of Table 18) increased the modulus of Inconel 625 matrix of the composite of less than 15 %.

The use of oxides reinforcement may improve the mechanical properties of cermets when the nano-sized particles were applied. Duan *et al.* [126] did show the hardness of composites of FeCrMo steel with 8 wt. % of nano-Al₂O₃ treated by CO₂ laser to be about *HV0.5*=630 and their elastic modulus to be about 164 GPa. The use of nano-YSZ reinforced Ni matrix obtained by preplacing powder and by CO₂ laser treatment, enabled to o Xiong *et al.* [128] obtaining microhardness *HV0.2* ranging from 1280 to 1440.

The nitride reinforcement, TiN, was used with 90 wt. % matrix of CoCrNiFeBSi self-fluxing alloy to obtain composite coatings with help of CO₂ cw laser. The composites had the microhardness of *HV0.2* about 1200 measured Weng *et al.* [137].

Bibliography

1. M.F. Ashby and D.R.H. Jones, *Engineering Materials 2: An Introduction to Microstructures, Processing, and Design*, Dunod, Paris, France, 1991 (in French).

2. N. Eustathopoulos, M.G. Nicholas, and B. Drevet, *Wettability at High Temperatures*, Pergamon Press and Elsevier Science, Kidlington, Oxford, UK, 1999.
3. L. Pawłowski, *Dépôts Physiques*, PPUR, Lausanne, Switzerland, 2003.
4. W. Kurz and D.J. Fisher, *Fundamentals of Solidification*, 4th edition, Trans Tech Publications Ltd, Zürich, Switzerland, 1998.
5. J. A. Dantzig and M. Rappaz, *Solidification*, PPUR, Lausanne, Switzerland, 2009.
6. A. Dupré, *Théorie Mécanique de la Chaleur*, Chapitre IX, Gauthier-Villars, Paris, France, 1869.
7. Z.M. Liu, S. Cui, Z. Luo, C. Zhang, Z. Wang, and Y. Zhang, Plasma arc welding: Process variants and its recent developments of sensing, controlling and modeling, *J. Manufact. Process.* 23 (2016) 315-27.
8. R.L. Deuis, J. M. Yellup, and C. Subramanian, Metal matrix composite by PTA surfacing, *Composite Sci. Technol.*, 58 (1998) 299-309.
9. D. Fan, X. Liu, J. Huang, R. Fu, S. Chen, and X. Zhao, An ultra-hard and thick composite coatings metallurgically bonded to Ti-6Al-4V, *Surf. Coat. Technol.* 278 (2015) 157-62
10. A. Emanian, S. F. Corbin and A. Khajepour, The effect of powder composition on the morphology of in situ TiC composite coating deposited by Laser-Assisted Powder Deposition (LAPD), *J. Appl. Surf. Sci.* 261 (2012) 201-208
11. J. R. Rumble, *CRC Handbook of Chemistry and Physics*, 99th edition 2018-2019
12. C. Costa, E. Barbareschi, P. Guarnone, and G. Borzone, Phase evolution in an MCrAlY coating during high temperature exposure, *J. Min. Metall. Sect. B Metall.* 48 (3) (2012) 359–365.
13. H. Wei, H.Y. Zhang, X.F. Sun, M.S. Dargusch, and X. Yao, Interdiffusion within the β -phase region of the Ni–Co–Cr–Al quaternary system, *J. of Alloys and Compounds*, 493 (2010) 507–516.
14. <https://www.reade.com/products/nickel-chromium-alloys-nicr>, checked on March, 19, 2019
15. G. K. Dey, Physical metallurgy of nickel aluminides, *Sadhana*, 28 (1-2) (2003) 247–262.
16. https://en.wikipedia.org/wiki/Nickel_aluminide checked on March, 19, 2019
17. W. Brandl, H.J. Grabke, D. Toma, and J. Krüger, The oxidation behavior of sprayed MCrAlY coatings, *Surf. Coat. Technol.*, 86-87 (1996) 41-7.
18. <https://en.wikipedia.org/wiki/Inconel> checked on March 26, 2019.
19. <https://fr.wikipedia.org/wiki/Hastelloy> checked on March, 29, 2019.
20. <https://en.wikipedia.org/wiki/Stellite> checked on March, 21, 2019.
21. F. Stein, M. Palm, and G. Sauthoff, Structure and stability of Laves phases. Part I. Critical assessment of factors controlling Laves phase stability, *Intermetallics*, 12 (7-9) (2004) 713-20.

22. M.J. Tobar, J.M. Amado, C. Alvarez, A. Garcia, A. Varela, and A. Yanez, Characteristics of Tribaloy T-800 and T-900 coatings on steel substrates by laser cladding, *Surf. Coat. Technol.*, 202 (11) (2008) 2297-301.
23. R.R. Boyer, Attributes, characteristics, and applications of titanium and its alloys, *JOM*, 62 (5) (2010) 21-4.
24. Catalog of society ACNIS Int. in Chassieu, France, <http://www.acnis-titanium.com/fr/titane/> consulted on March 29, 2019.
25. *Machine Design*, Iron-based superalloys, November 15, 2002, <https://www.machinedesign.com/basics-design/iron-based-superalloys>, consulted on April 24, 2019.
26. W.A. Harrison, *Pseudo Potential theory of Metals*, Benjamin, New York, N.Y., USA, 1966.
27. V. Heine, *Solid State Physics*, Academic Press, New York, N.Y., USA, 1970
28. E. Theile, Equation of state for hard spheres, *J. Chem. Phys.*, 39 (2) (1963) 474-479.
29. J. Libowitz, Exact solution of generalized Percus-Yevick equation for a mixture of hard spheres, *Phys. Rev.* 133 (4A) (1964) 895-899.
30. T. E. Faber, *Introduction to the Theory of Liquid Metals*, Cambridge University Press, Cambridge, UK, 1972.
31. M. Simoji, *Liquid Metals*, London Academic, London, UK, 1977.
32. H.C. Longuet-Higgins, The statistical thermodynamics of multicomponent systems, *Proc. R. Soc.* A205 (1951) 247-269.
33. K.P. Shukla, M. Luckas, H. Marquardt, and K. Lucas, Conformal solutions: which model for which application? *Fluid Phases Equilibria*, 26 (2) (1986) 129-47.
34. B. Bhatia and R. N. Singh, Thermodynamic properties of compound forming molten alloys in a weak interaction approximation, *Phys. Chem. Liqs.*, 11(4) (1982) 343-351.
35. B. Bhatia and R. N. Singh, A quasi-lattice theory for compound forming molten alloys, *Phys. Chem. Liqs.*, 13 (3) (1984) 177-190.
36. C. Costa, S. Delsante, G. Borzone, D. Zivkovic, and R. Novakovic, Thermodynamic and surface properties of liquid Co–Cr–Ni alloys, *Journal of Chemical Thermodynamics*, 69, 2014, 73–84.
37. R. Novakovic and T. Tanaka, Bulk and surface properties of Al–Co and Co–Ni liquid alloys, *Physica B* 371 (2) (2006) 223–231, cited after [36]
38. D. Adhikari, I. S. Jha and B.P. Singh, *Energy Disorder in Liquid Fe-Si Alloy*, *The Himalayan Physics*, 1 (1) 2010.

39. S. Jonsson, Assessment of the Fe–Ti–C system, calculation of the Fe–Ti–N system and prediction of the solubility limit of Ti(C,N) in liquid Fe, *Metallurgical and Materials Transactions B: Process Metallurgy and Materials Processing Science* 29 (1998) 371–384.
40. X. Wang, Z. Zou, and S. Qu, Microstructure of Fe-based alloy hardfacing coating reinforced by TiC-VC particles,” *Journal of Iron and Steel Research International*, 13(4) (2006), 51-55.
41. E.A. Brandes, G.B. Smithells, *Metals Reference Book*, 6th ed., Butterworths Oxford UK, 1983.
42. X. Feng, L.X. Liu, H. Yang, H.K. Zhao, F. Liang, C. Zhang, Surface tension of molten Ni-(Cr, Co, W) alloys and segregation of elements, *Trans. Non Ferrous Met. Soc. China* 18 (2008) 1184-88.
43. S. K. Chung, D. B. Thiessen, and W.K. Rhim, A non-contact measurement technique for the density and thermal expansion coefficient of solid and liquid materials, *Rev. Sci. Instrum.* 67 (1996) 3175.
44. O. V. Savin, N.N. Stepanova, D.P. Rodionov, Y. N. Akshentsev, V.A. Sazovona, Y.E. Turhan., X-ray diffraction investigation of ordering kinetics in Ni₃Al alloyed with a third element, *Phys. Met. Metallography* 90 (2000) 138-44.
45. N. N. Stepanova, S. G. Teploukhov, S.F. Dubinin, Y.N. Akshentsev, D.P. Rodionov, V.D. Parkhomenko, Study of the structure of Ni₃Al and (Ni,Co)₃Al crystals grown by the Bridgman method, *Phys. Met. Metallography* 96 (2003) 626-633.
46. H.P. Wang, J. Chang, and B. Wei, Density and related thermophysical properties of metastable liquid Ni-Cu-Fe ternary alloys, *Physics Letters A*, 374 (2010) 2489-93.
47. M. Hillert, *Phase Equilibria, Phase Diagrams and Phase Transformations, Their Thermodynamic Basis*, 2nd ed., Cambridge University Press, Cambridge, UK, 2007.
48. T. Ejima and T. Yamamura, Impurity diffusion in liquid aluminum and copper, *Le Journal de Physique Colloques*, 41 (C8) (1980) 345-348.
49. R.P. Smith, The diffusivity of carbon in iron by steady-state method, *Acta Metal.* 1 (1953) 578-587.
50. S.K. Bose and H.J. Grabke, Diffusion coefficient of carbon in Fe-Ni austenite in the temperature range 950-1100 degree C, *Z. Metallkd.* 69 (1) (1978) 8-15.
51. S.K. Roy, H.J. Grabke, and W. Wepner, Diffusivity of carbon in austenitic Fe-Si-C alloys, *Arch. Eisenhütt.*, 51 (3) (1980) 91-6.
52. C. Wells and R.F. Mehl, Rate of diffusion of carbon in austenite in plain carbon, in nickel and in manganese steels, American Institute Mining Metallurgical Engineers, Technical Publication, 1940, 1180-9.

53. O. Dahlke and O. Knake, Die Auflösung von Kohlenstoff in flüssigem Eisen, Arch. Eisenhüttenwesen, 26 (1955) 373-382
54. W. Batz and R.F. Mehl, Diffusion coefficient of carbon in austenite, Trans. AIME, 188, (1950) 553—60.
55. D.W. Morgan and J.A. Kitchener, Solution in liquid iron, Part 3: - Diffusion of Cobalt and carbon, Trans. Faraday Soc., 50, 1954, 51-60.
56. M. Nabeel, "Diffusion of elemental additives during sintering", Royal Institute of Technology, Sweden, Master's Thesis 2012.
57. A. Villegas, "The diffusion of nitrogen in liquid iron alloys at 1600° C" PhD thesis, Stanford University, Stanford, CA, USA, April 1976
58. K. Schwerdtfeger, Diffusion of oxygen and nitrogen in liquid iron, Trans. AIME, 239 (1967) 134-137
59. M. Inouye, Y. Kojima, T. Choh, T. S. Uekawa, and Y. Yamada, On the measurements of diffusion coefficients of nitrogen in the liquid Fe, J. Iron Steel Institute of Japan (*Tetsu-to-Hagane*) 59 (1973) 205-13.
60. H. D. Kunze, Effect of the elements chromium, manganese, cobalt, nickel, molybdenum and tungsten on the diffusion of nitrogen in liquid iron alloys, Arch. Eisenhüttenw., 44 (2), (1973) 71-80 .
61. J. Y. Lee, *The Diffusion of Nitrogen in Liquid Iron and Iron Alloys*, Stanford University, Stanford, CA, USA, PhD. Thesis (1971)
62. J. Y. Lee and N. A. D. Parlee, The diffusion of nitrogen in liquid iron and iron alloys, J. High Temperature Science, 4 (2) (1972) 147-59.
63. B. R. Benner and N. A. D. Parlee, The rates of absorption of nitrogen in the stagnant liquid Fe-Co and Fe-Ni alloy systems at 1600°C, Metallurgical and Materials Transactions B 4(1) (1973) 370-373.
64. Y. Kojima, Y. Yamada, and M. Inouye, The solubilities and diffusion coefficients of nitrogen in the liquid Iron-Nickel and Iron-Cobalt alloys at 1600°C", J. Iron Steel Institute of Japan (*Tetsu-to-Hagane*), 61 (2) (1975) 195-201.
65. M. Walbrühl, "Diffusion in the liquid Co binder of cemented carbides: Ab initio molecular dynamics and DICTRA simulations", KTH Royal Institute of Technology, Degree project in Materials Science and Engineering Second cycle, Stockholm, Sweden 2014
66. H. Bester and K. W. Lange, Arch. Eisenhüttenwes. 44 (1973) 71-80.
67. Diffusion Information Center, Cleveland, Ohio, "Diffusion Data" v. 4, (1970)

68. R. Saiz, R. M. Cannon and A. P. Tomsia, Atomic transport at liquid metal/ Al_2O_3 Interfaces, Key Engineering Materials, "Defect and Diffusion Forum" vols. 194-199 (2001), 1-10.
69. E. S. Posner, D. C. Rubie, D. J. Frost, and G. Steinle-Neumann, Experimental determination of oxygen diffusion in liquid iron at high pressure, Earth and Planetary Science Letters 464 (2017) 116–23.
70. S. Otsuka, and Z. Kozuka, The diffusivities of oxygen in liquid Nickel and Liquid Iron determined by electrochemical measurements, Trans. JIM, 1977 Vol. 18, 690-696.
71. M. Lu and Q. Jiang, Surface tension and its temperature coefficient for liquid metal, J. Phys. Chem. B 2005, 109, 15463 -68
72. O. Dezellus and N. Eustathopoulos, Fundamental issues of reactive wetting by liquid metals, Journal of Materials Science, 45 (16) (2010) 4256-64.
73. M. G. Nicholas, *Ceramic-Metal Interfaces in Surfaces and Interfaces of Ceramic Materials*, Kluwer Academic Publishers, London, United Kingdom, 1989, 293-417
74. J. M. Howe, Bonding, Structure and properties of metal/ceramic Interfaces - Part I chemical bonding, chemical reaction and interfacial structure. Int. Mater. Rev., 38 (1993) 233-255.
75. R. Arroyave, *Thermodynamics and Kinetics of Ceramic/Metal Interfacial Interaction*, PhD Thesis, Massachusetts Institute of Technology, Boston, MA, USA, February 2004.
76. J. Lawrence, Wetting and bonding characteristics of selected liquid-metals with a high power diode laser treated alumina bioceramic, Proc. Royal Soc. Lond. 460 (2004) 1723-35.
77. J. G. Li, Role of electron density of liquid metals and band- gap energy of solid ceramics on the work of adhesion and wettability of metal/ceramic systems, J. Mater. Sci. Lett. 11 (1992) 903–905.
78. J. G. Li, Wetting and interfacial bonding of metals with ion covalent oxides, J. Am. Ceram. Soc. 75 (1992) 3118–26.
79. O. Dezellus and N. Eustathopoulos, The role of van der Waals interactions on wetting and adhesion in metal/carbon systems, Scripta Materialia 40 (11) (1999), 1283-8.
80. C. Rado, S. Kalogeropoulou, and N. Eustathopoulos, Bonding and wetting in non-reactive metal/SiC systems: weak or strong interfaces? Materials Science and Engineering A 276 (1-2) (2000) 195–202.
81. O. Dezellus, R. Voytovych, A. Li, G. Constantin, F. Bosselet, and J. Viala, Wettability of Ti_3SiC_2 by Ag-Cu and Ag-Cu-Ti melts, Journal of Materials Science 8 (2010) 2080-2084.
82. R. Voytovych, A. Koltsov, F. Hodaj, and N. Eustathopoulos, Reactive vs nonreactive wetting of ZrB_2 by azeotropic Au-Ni, Acta Materialia 55 (18) (2007) 6316–21.

83. Y.V. Naidich and N.Y. Taranets, Wettability trends for molten metals on aluminum nitride Poroshk. Metall., 5-6, (1996) 74-78.
84. Y. V. Naidich, *Progress in Surface and Membrane Sciences*, v. 14, (in:] *The Wettability of Solids by Liquid Metals*, Academic Press, New-York, 1981, 353–484.
85. C. Rado and N. Eustathopoulos, The role of surface chemistry on spreading kinetics of molten silicides on silicon carbide, *Interface Science* 12(1) (2004) 85–92.
86. P. Protsenko, A. Terlain, M. Jeymond, and N. Eustathopoulos, Wetting of Fe-7.5Cr steel by molten Pb and Pb-17Li, *Journal of Nuclear Materials* 307-311 (Part 2) (2002) 1396–1399.
87. E. Saiz and A. P. Tomsia, Atomic dynamics and Marangoni films during liquid-metal spreading, *Nature Materials*, 3(12) (2004), 903–909.
88. N. Eustathopoulos, Progress in understanding and modeling reactive wetting of metals on ceramics, *Current Opinion in Solid State and Materials Science* 9(4-5) (2005) 152–60.
89. K. Landry and N. Eustathopoulos, Dynamics of wetting in reactive metal/ceramic systems: linear spreading, *Acta Materialia* 44(10) (1996) 3923–3932.
90. F. Mechighel, M. Kadja, and B. Pateyron, Document Study of macro-segregation defects formation caused by double diffusive convective flow during solidification of a binary alloy, *Defect and Diffusion Forum* 283-286, (2008) 340-5.
91. F. Mechighel, M. El Ganaoui, M. Kadja, B. Pateyron, and S. Dost, Numerical simulation of three dimensional low Prandtl liquid flow in a parallelepiped cavity under an external magnetic field, *Fluid Dynamics and Materials Processing*, 5 (4) (2009) 313-330
92. A. Passerone, M. L. Muolo, F. Valenza, F. Monteverde, and N. Sobczak, Wetting and interfacial phenomena in Ni-HfB₂ systems, *Acta Materialia* 57 (2) (2009) 356–64.
93. R. Voytovych, A. Koltsov, F. Hodaj, and N. Eustathopoulos, Reactive vs nonreactive wetting of ZrB₂ by azeotropic Au-Ni, *Acta Materialia* 55(18) (2007) 6316–6321.
94. N. Frage, N. Froumin, and M. P. Dariel, Wetting of TiC by non-reactive liquid metals, *Acta Materialia* 50(2) (2002) 237–245.
95. S. Kalogeropoulou, C. Rado, and N. Eustathopoulos (1999) Mechanisms of reactive wetting: the wetting to non-wetting case, *Scripta Materialia* 41(7) (1999) 723–728.
96. O. Dezellus, F. Hodaj, C. Rado, J. N. Barbier, and N. Eustathopoulos, Spreading of Cu-Si alloys on oxidized SiC in vacuum: experimental results and modelling, *Acta Materialia* 50 (2002) 979–991.
97. P. Protsenko, A. Terlain, M. Jeymond, and N. Eustathopoulos, Wetting of Fe-7.5Cr steel by molten Pb and Pb-17Li, *Journal of Nuclear Materials* 307-311 (Part 2) (2002), 1396–9.
98. P. Protsenko, A. Terlain, V. Traskine, and N. Eustathopoulos, The role of intermetallics in wetting in metallic systems. *Scripta Materialia* 45(12) (2001)1439–1445.

99. X.B. Zhou and J. Th. M. De Hosson, Reactive wetting of liquid metals on ceramic substrates, *Acta Mater.* 44(2) (1996) 421-426.
100. V. Jankauskas, M. Antinov, V. Varnauskas, R. Skirkus, and D. Goljandin, Effect of WC size and content on low stress abrasive wear of manual arc welded hardfacings with low-carbon or stainless-steel matrix, *Wear* 328-329 (2015) 378-390.
101. G. Sun, Z. Tong, X. Fang, X. Liu, Z. Ni and W. Zhang, Effect of scanning speeds on microstructure and wear behavior of laser-processed NiCr-Cr₃C₂-MoS₂-CeO₂ on 38CrMoAl steel, *Optics & Laser Technol.* 77 (2016) 80-90.
102. L. Fouilland-Paille, S. Ettaqi, S. Benayoun, and J.J. Hantzpergue, Structural and mechanical characterization of Ti/TiC cermet coatings synthesized by laser melting, *Surf. Coat. Technol.* 88 (1996) 204-211.
103. F. Weng, H. Yu, C. Chen, and J. Dai, Microstructures and wear properties of laser cladding Co-based composite coatings on Ti-6Al-4V, *Mater. Design* 80 (2015) 174-181.
104. M.G. Hocking, V. Vantasree, and P.S. Sidky, *Metallic and Ceramic Coatings*, Longman Scientific & Technical, Burnt Mill, London, England, 1989.
105. X. Guozhi, S. Xiaolong, Z. Dongjie, W. Yuping and L. Pinghua, Microstructure and corrosion properties of thick WC composite coating formed by plasma cladding, *Appl. Surf. Sci.* 256 (2010) 6354-6358.
106. V. Balasubramanian, A.K. Lakshminarayanan, R. Varahamoorthy, and S. Babu, Application of response surface methodology to prediction of dilution on PTA hardfacing of stainless steel on carbon steel, *J. Iron Steel Res., Int.* 16(1) (2009) 44-53.
107. N.J. Allnat, G.R. Bell, and L.J. Griffith, *Developments in plasma arc surfacing*, [in:] Proc. 9th Inter. Therm. Spray. Conf., 19–23 May 1980, Hague, Pays Bas, Nederlands Instituut voor Lastechniek, Hague, Netherlands, 1980, 218–223.
108. A. Zikin, E. Badisch, I. Hussainova, C. Tomastik, and H. Danninger, Characterisation of TiC-NiMo reinforced Ni-based hardfacing, *Surf. Coat. Technol.* 236 (2013) 36-44.
109. C. Demian, A. Denoirjean, L. Pawłowski, P. Denoirjean, and R. El Ouardi, Microstructural investigations of NiCrAlY + Y₂O₃ stabilized ZrO₂ cermet coatings deposited by plasma transferred arc (PTA), *Surf. Coat. Technol.* 300 (2016) 104-109.
110. H. Hallen and C. Herrström, *PTA – Beschichtung mit Nickelaluminiumpulvern*, [in:] Thermische Spritzkonferenz TS 93, DVS – Berichte Band 152, DVS Verlag, Düsseldorf, Germany, 1993, 167–170.

111. D.R. Marantz and S.J. Richardson, *Plasma – transferred arc hard – facing an improved process for surfacing*, [in:] Proc. 9th Int. Therm. Spray. Conf., 19–23 May 1980, Hague, Netherlands, Nederlands Instituut voor Lastechniek, Hague, Netherlands, 1980, 207–210.
112. L. Pawłowski, *The Science and Engineering of Thermal Spray Coatings*, 2nd ed., Wiley, Chichester, U.K., 2008.
113. G. Brassart, J.L. Meyzonnett, and J.-P. Pocholle, *Sources laser*, [in:] Techniques de l'Ingénieur, E 4020 V1, 10 September 1996.
114. Catalogue of society Laserline, Mülheim, Germany [in:] <http://www.laserline.de/diode-laser-material-processing.html> visited on 28 February 2017.
115. M. Hanna, "Sources laser à fibre et applications", [in:] Techniques de l'Ingénieur, E 6450 V2, 10 January 2012.
116. L. Pawłowski, Thick laser coatings: a review, *J. Thermal Spray Technol.* 5 (1999) 279-295
117. A. Zikin, S. Ilo, P. Kulu, I. Hussainova, C. Katsich, and E. Badisch, Plasma transferred arc (PTA) hardfacing of recycled hardmetal reinforced nickel-matrix surface composites, *Materials Science* 18 (1) (2012) 12-17.
118. T. Araki, M. Nishida, A. Hirose, and H. Fujita, Effect of particle size of carbide powder and silica sand on abrasive wear resistance of an overlay composite alloy, *Welding International* 8 (1) (1994) 23-29.
119. M.R. Mansur, J. Wang, and C.C. Berndt, Microstructure, composition and hardness of laser-assisted hydroxyapatite and Ti-6Al-4V composite coatings, *Surf. Coat. Technol.* 232 (2013) 482-488.
120. C. Chang, D. Verdi, M. A. Garrido, and J. Ruiz-Hervias, Micro-scale mechanical characterization of Inconel cermet coatings deposited by laser cladding, *Boletín de la Sociedad Espanola de Ceramica Y Vidrio*, 55 (4) (2016) 136-142.
121. T.E. Abioye, P.K. Farayibi, D.G. McCartney, and A.T. Clare, Effect of carbide dissolution on the corrosion performance of tungsten carbide reinforced Inconel 625 wire laser coating, *J. Mater. Process. Technol.* 231 (2016) 89-99.
122. A. Emamian, S.F. Corbin, and A. Khajepour, Effect of laser cladding process parameters on clad quality and in situ formed microstructure of Fe-TiC composite coatings, *Surf. Coat. Technol.* 205 (2010) 2007-2015.
123. A. Emamian, S.F. Corbin, and A. Khajepour, The effect of powder composition on the morphology of in-situ TiC composite coating deposited by Laser-Assisted Powder Deposition (LAPD), *Appl. Surf. Sci.* 261 (2012) 201-208.

124. D. Liu, P. Hu, and G. Min, Interfacial reaction in cast WC particulate reinforced titanium metal matrix composites coating produced by laser processing, *Optics & Laser Technol.* 69 (2015) 180-186.
125. M. Doubenskaia, A. Kh. Gilmutdinov, and K. Yi. Nagulin, Laser cladding of metal matrix composites reinforced by cermet inclusions for dry friction applications at ambient and elevated temperatures, *Surf. Coat. Technol.* 276 (2015) 696-703.
126. X. Duan, S. Gao, Q. Dong, Y. Zhou, M. Xi, X. Xian, and B. Wang, Reinforcement mechanism and were resistance of $\text{Al}_2\text{O}_3/\text{Fe-Cr-Mo}$ steel composite coating produced by laser cladding, *Surf. Coat. Technol.* 291 (2016) 230-238.
127. L. Pawłowski and I. Smurov, Modeling of high-power laser interaction with APS deposited FeCr-TiC, *Surf. Coat. Technol.* 151-152 (2002) 308-315.
128. L. Xiong, H. Zheng, P. Yu, G. Li, Z. Chen, and B. Zhang, Laser-clad YSZ@Ni (core-shell nanoparticle) composite coatings, *Ceram. Int.* 41 (2015) 13850-13854.
129. L. Kadanoff, Turbulent heat flow: structures and scaling, *Physics Today*, 54 (8) (2001) 34-39.
130. A. Kumar and S. Roy, Effect of three-dimensional melt pool convection on process characteristics during laser cladding, *Comput. Mater. Sci.* 46 (2009) 495-506.
131. V. Fallah, M. Alimardani, S.F. Corbin, and A. Khajepour, Temporal development of melt-pool morphology and clad geometry in laser powder deposition, *Comput. Mater. Sci.* 50 (2011) 2124-2134.
132. J.I. Arrizubieta, A. Lamikiz, F. Klocke, S. Martinez, K. Arntz, and E. Ukar, Evaluation of the relevance of melt pool dynamics in Laser Material Deposition process modeling, *Int. J. Heat Mass Transfer* 115 (2017) 80-91
133. O.N. Celik, Microstructure and wear properties of WC particle reinforced composite coating on Ti6Al4V alloy produced by the plasma transferred arc method, *Appl. Surf. Sci.* 274 (2013) 334-40.
134. Z. Dawei, T. Li, and T.C. Lei, Laser cladding of Ni-Cr₂C₃/(Ni+Cr) composite coating, *Surf. Coat. Technol.* 110 (1998) 81-85.
135. S. Tondu, T. Schnick, L. Pawłowski, B. Wielage, S. Steinhäuser, and L. Sabatier, Laser glazing of FeCr-TiC composite coatings, *Surf. Coat. Technol.* 123 (2000) 247-251.
136. Y. Cai, Z. Luo, M. Feng, Z. Liu, Z. Huang, and Y. Zeng, The effect of TiC/ Al_2O_3 composite ceramic reinforcement on tribological behavior of laser cladding Ni60 alloys coatings, *Surface & Coatings Technology* 291 (2016) 222–229/

137. F. Weng, H. Yu, C. Chen, J. Liu, and L. Zhao, Microstructures and properties of TiN reinforced Co-base composite coatings modified with Y_2O_3 by laser cladding on Ti-6Al-4V alloy, *J. Alloys Compounds* 650 (2015) 178-184.
138. Q. Ma, Y. Yajiang, J. Wang, and K. Liu, Microstructure evolution and growth control of ceramic particles in wide- and laser clad Ni60/WC composite coatings, *Mater. Design*, 92 (2016) 897-905.
139. Y. Fan, X. Cui, Y. Li, and Z. Gao, Effect of Nb and CeO_2 on the mechanical and tribological properties of Co-based cladding coatings, *Surf. Coat. Technol.* 288 (2016) 25-29.
140. A. Zikin, I. Hussainova, C. Katsich, E. Badisch, and C. Tomastik, Advanced chromium carbide-based hardfacings, *Surf. Coat. Technol.* 206 (2012) 4270-4278.
141. Y. Lyu, Y. Sun, and F. Jing, on the microstructure and wear resistance of Fe-based composite coatings processed by plasma cladding with B_4C injection, *Ceram. Int.* 41 (2015) 10934-10939.
142. J. Liu, L. Wang, and H. Li, Reactive plasma cladding of TiC/Fe cermet using asphalt as a carbonaceous precursor, *Appl. Surf. Sci.* 255 (2009) 4921-4925.
143. D. Chen, D. Liu, Y. Liu, H. Wang, and Z. Huang, Microstructure and fretting wear resistance of γ /TiC composite coating in situ fabricated by plasma transferred arc cladding, *Surf. Coat. Technol.* 239 (2014) 28-33.
144. J. Liu, S. Yang, W. Xia, X. Jiang, and C. Gui, Microstructure and wear resistance performance of Cu-Ni-Mn alloy based hardfacing coatings reinforced by WC particles, *J. Alloy. Comp.* 654 (2016) 63-70.
145. A. Liu, M. Guo, M. Zhao, and C. Wang, Microstructures and wear resistance of large WC particles reinforced surface metal matrix composites produced by plasma melt injection, *Surf. Coat. Technol.* 201 (2007) 7978-7982.
146. H. Rojacz, A. Zikin, C. Mozelt, H. Winkemann, and E. Badisch, High corrosion studies of cermet particle reinforced NiCrBSi hardfacings, *Surf. Coat. Technol.* 222 (2013) 90-96.
147. D. Deschuyteneer, F. Petit, M. Gonon, and F. Cambier, Processing and characterization of laser clad NiCrBSi/WC composite coatings – influence of microstructure on hardness and wear, *Surf. Coat. Technol.* 283 (2015) 162-171.
148. Y.P. Kathuria, Nd-YAG laser cladding of Cr_2C_3 and TiC cermets, *Surf. Coat. Technol.* 140 (2001) 195-199.
149. C. Kumar Sahoo and M. Masanta, Effect of pulse laser parameters on TiC reinforced ISI 304 stainless steel composite coating by laser surface engineering process, *Optics and Lasers in Engineering* 67 (2015) 35-48.

150. X. Luo, J. Li, and G.J. Li, Effect of NiCrBSi content on microstructural evolution, cracking susceptibility and wear behaviors of laser cladding WC/Ni-NiCrBSi composite coatings, *J. Alloy. Comp.* 626 (2015) 102-111.

Figures

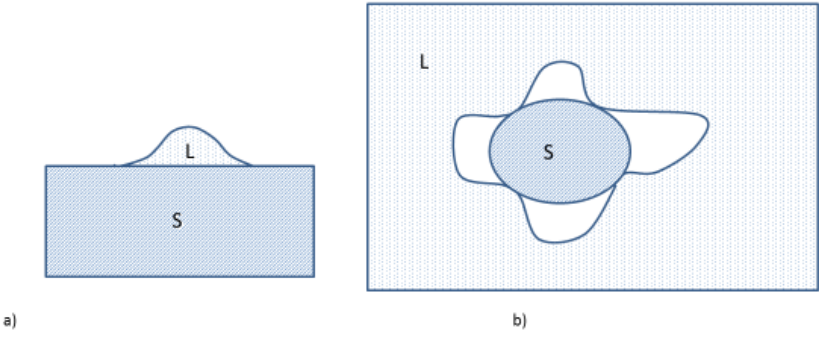


Fig. 1

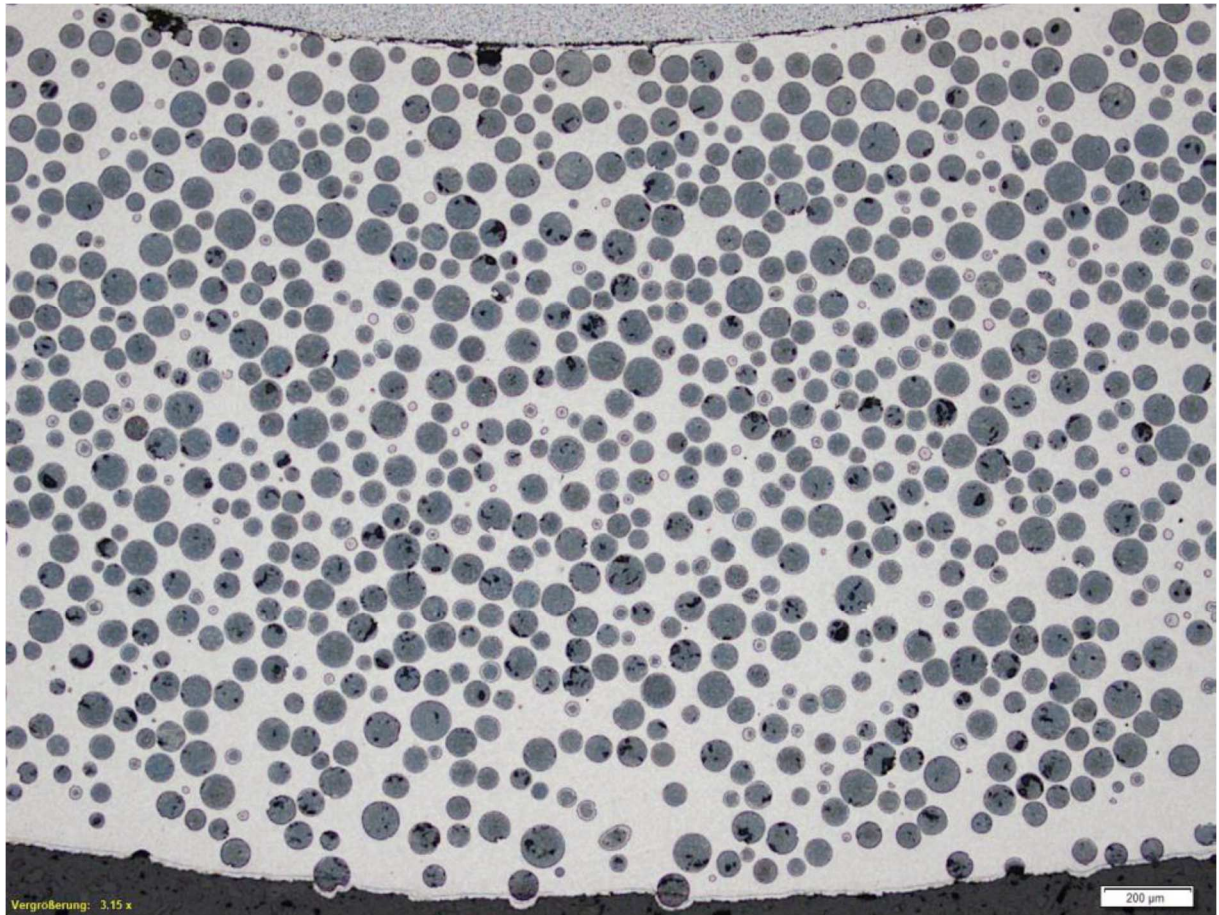


Fig. 2

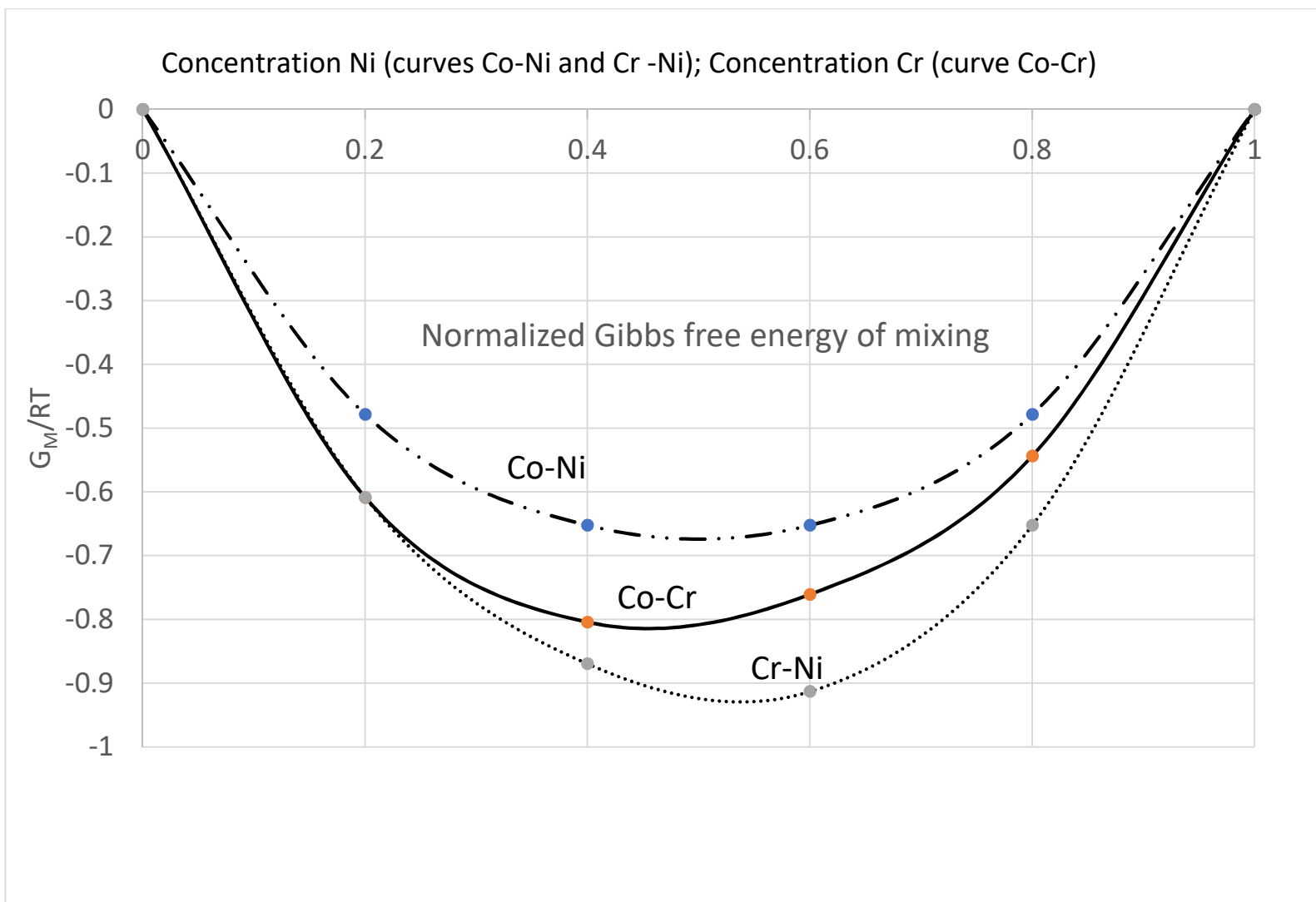


Fig. 3

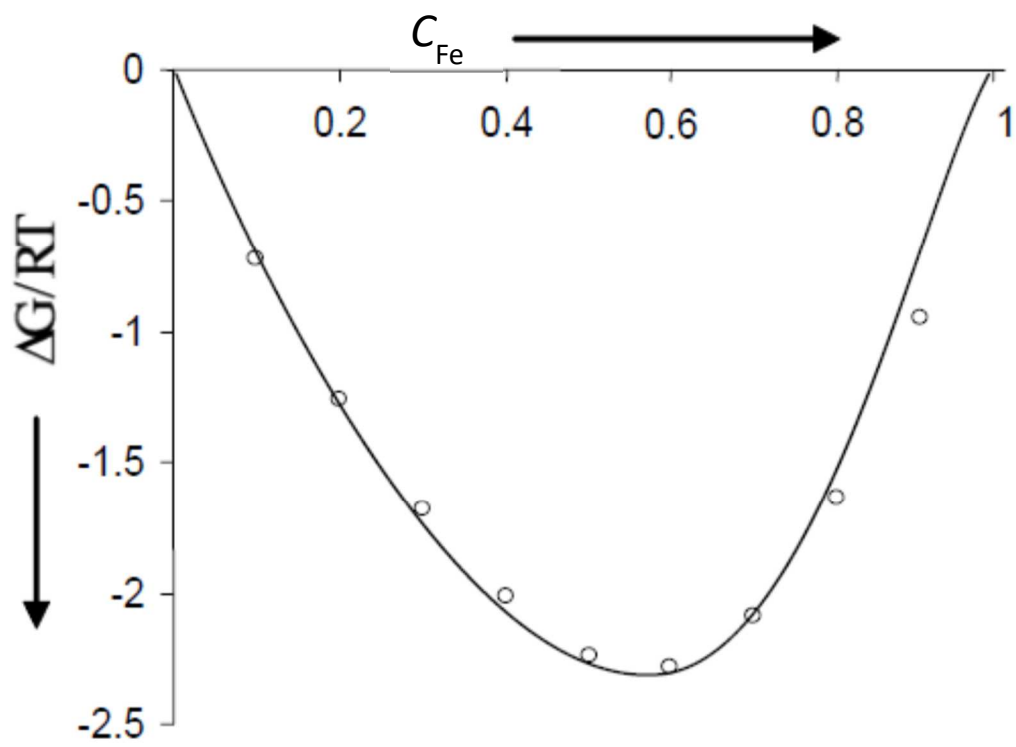


Fig. 4

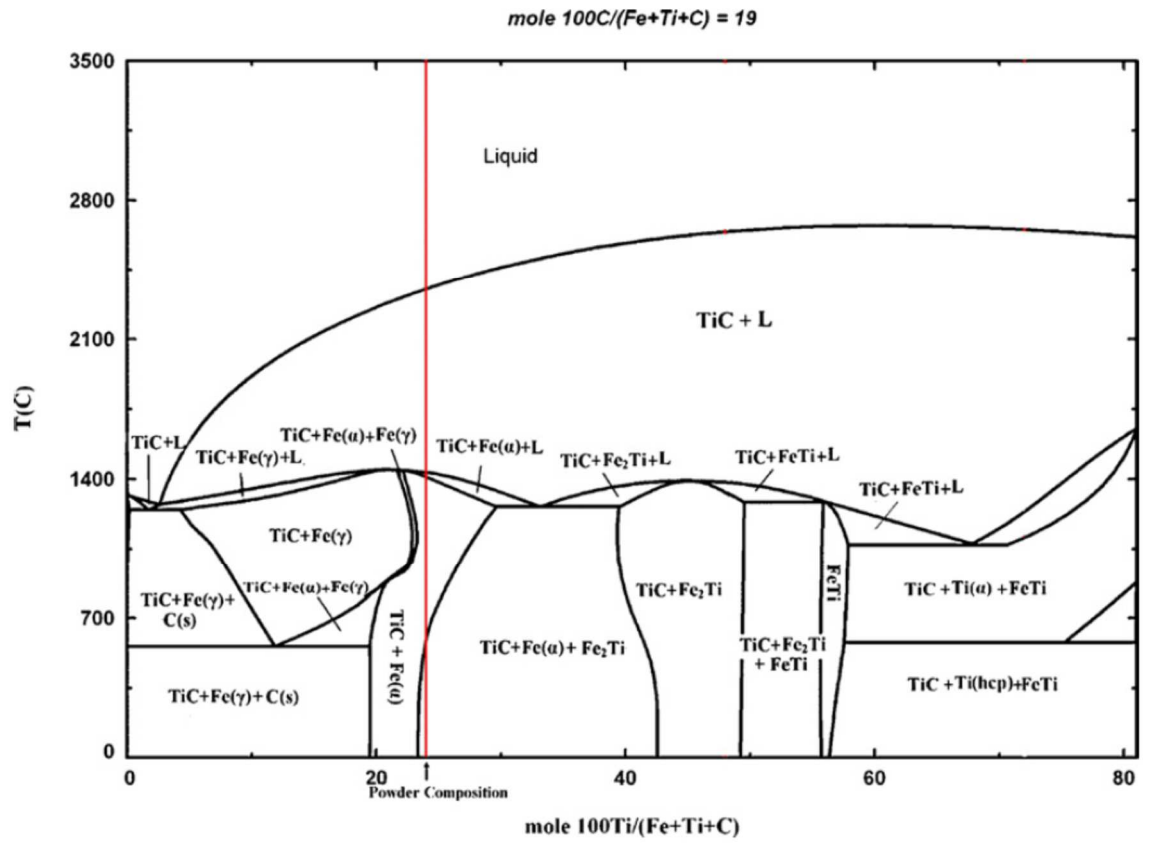


Fig. 5

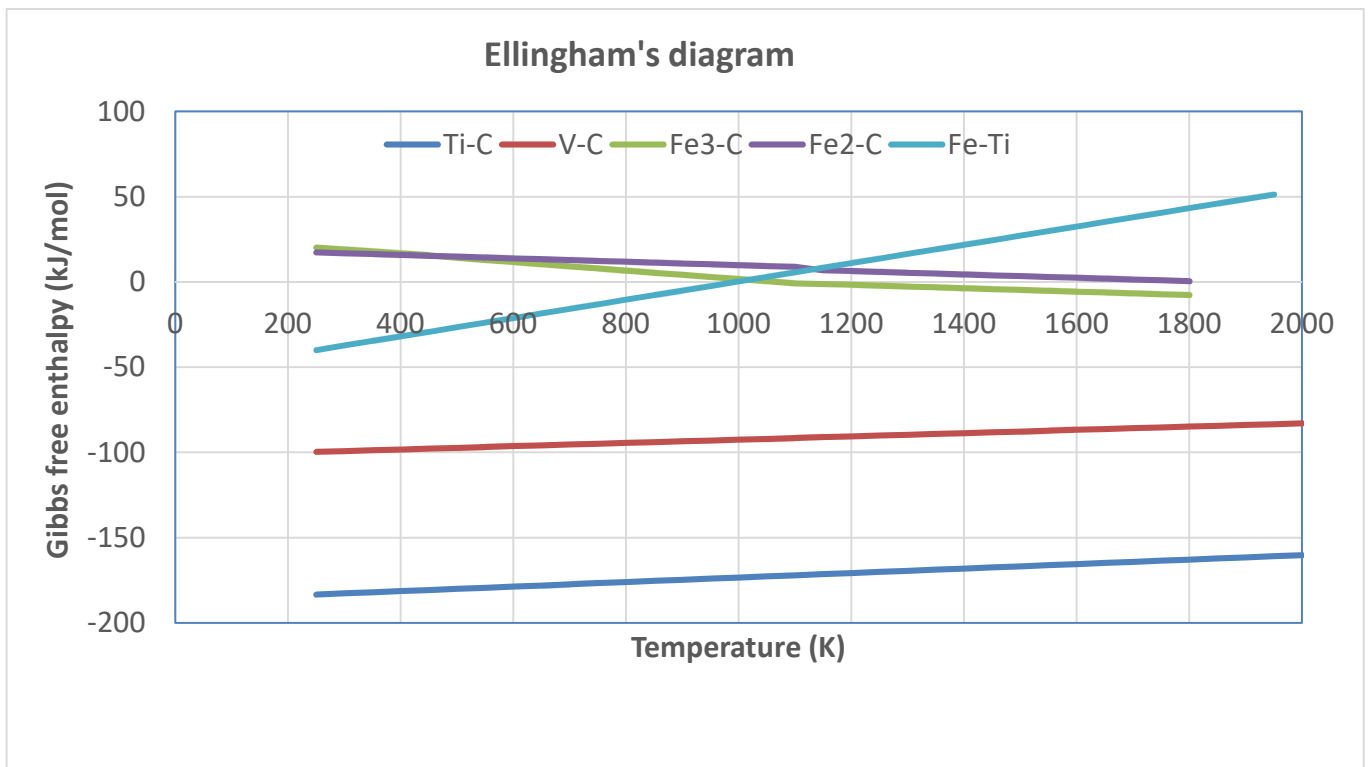


Fig. 6

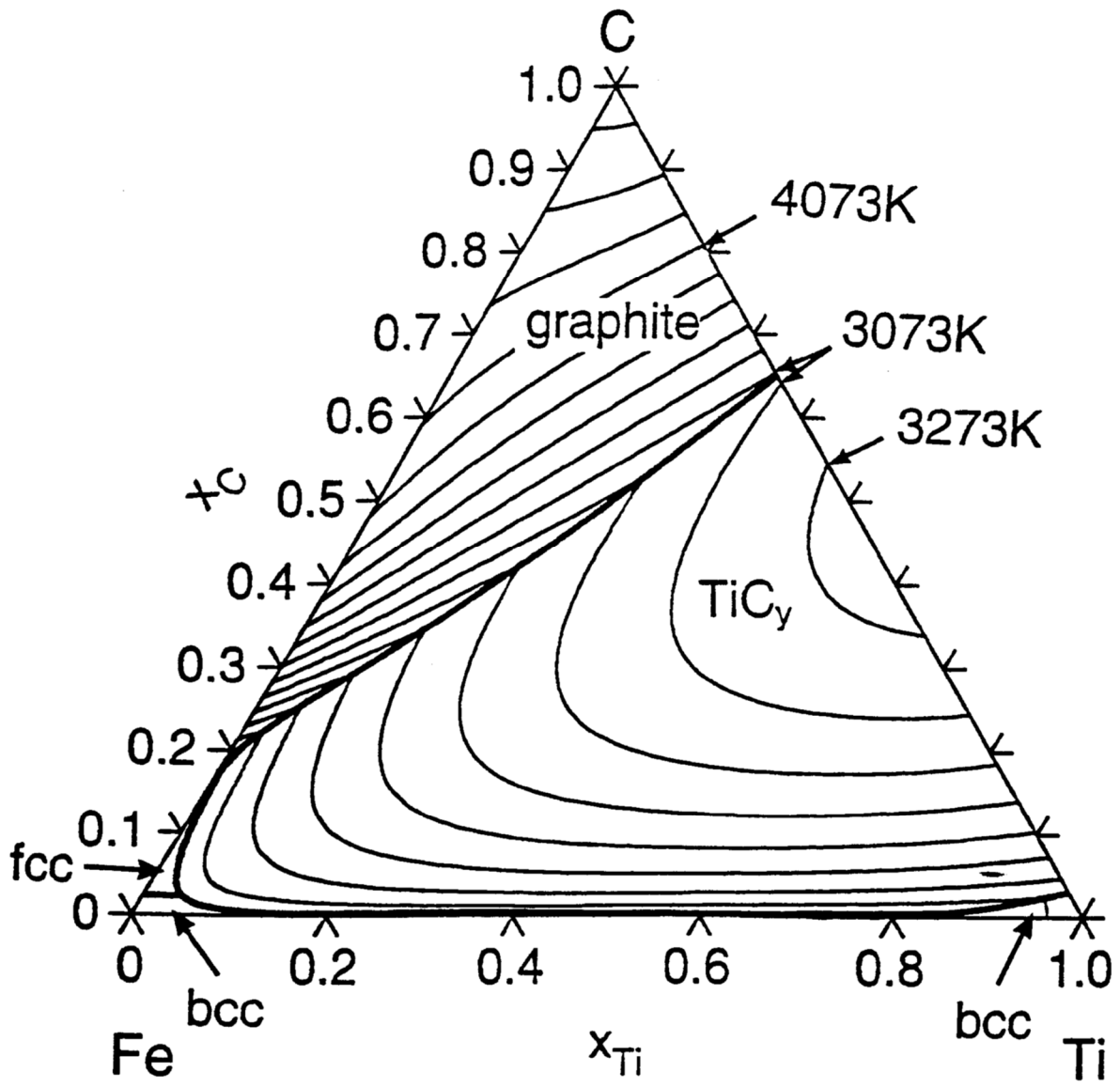


Fig. 7

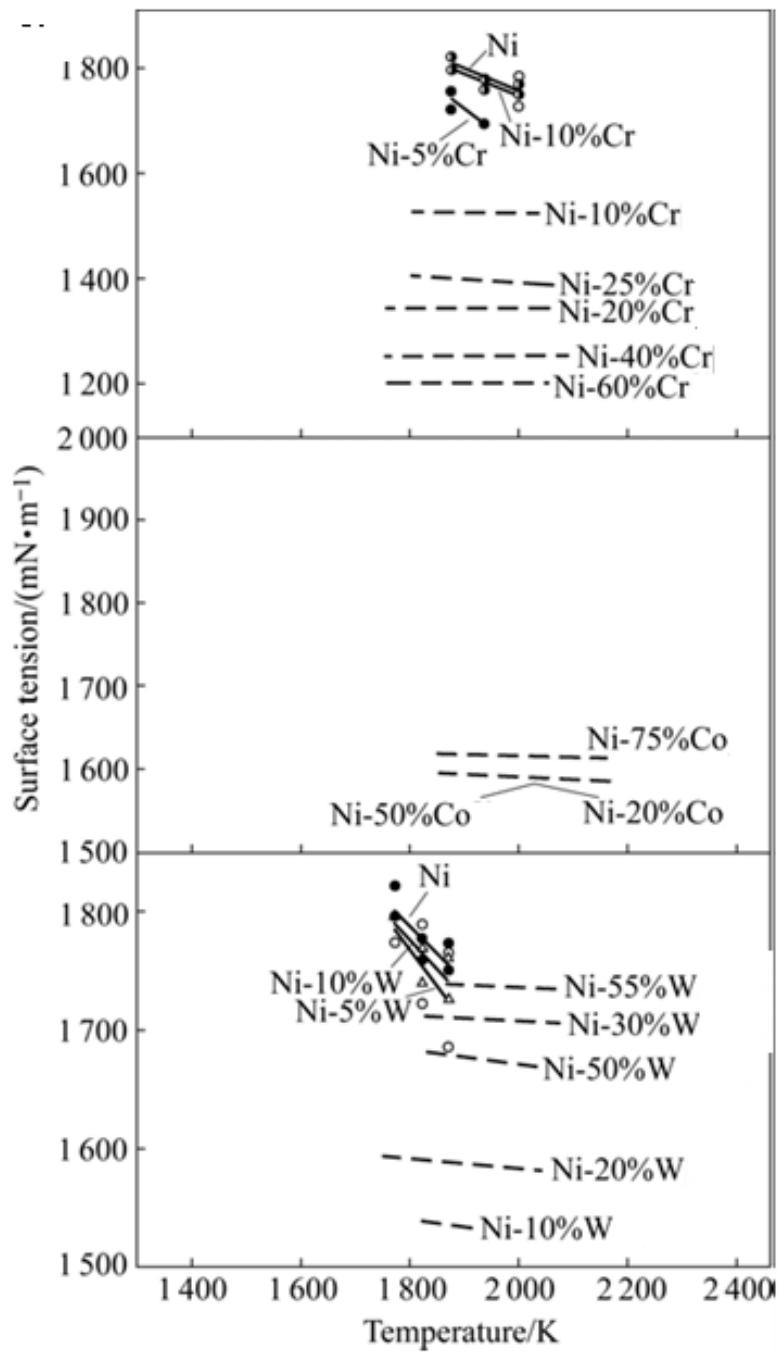


Fig. 8

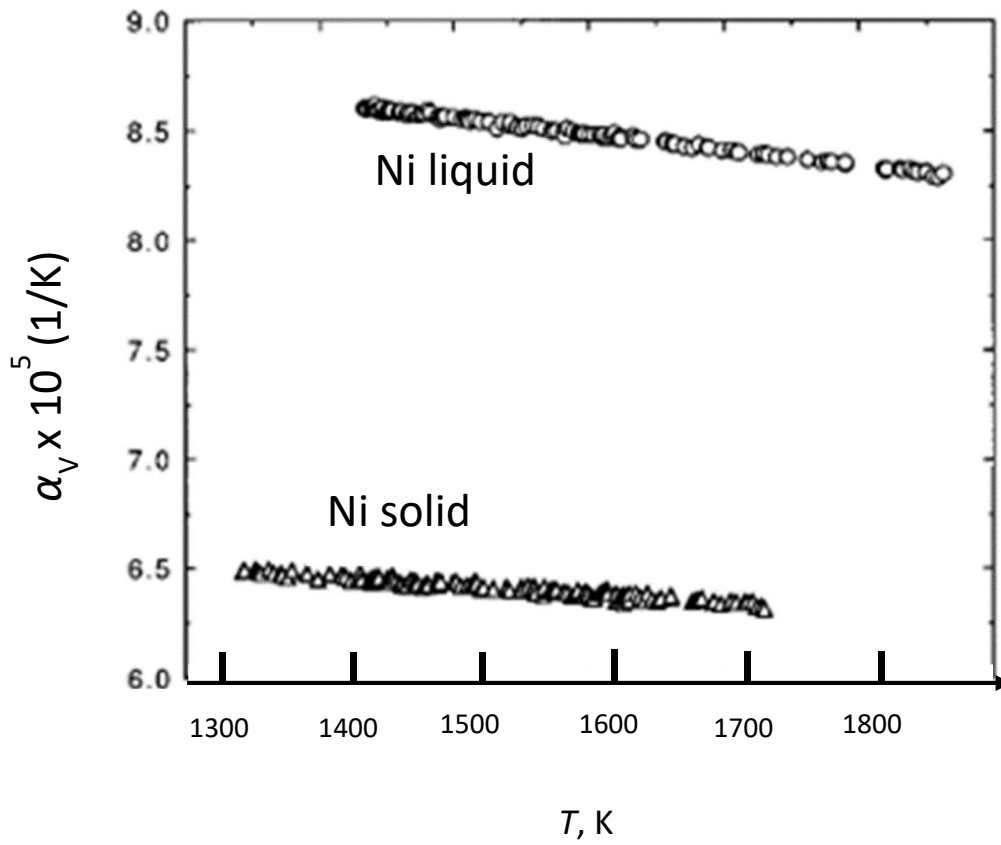


Fig. 9

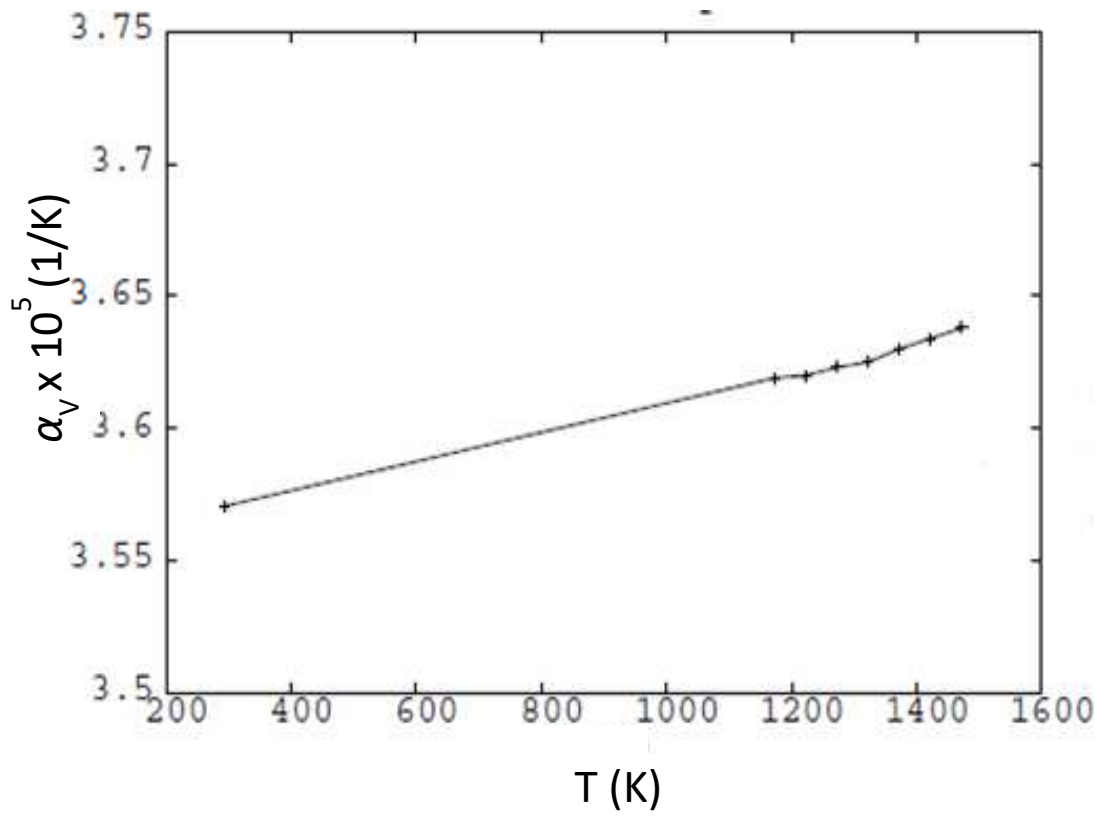


Fig. 10

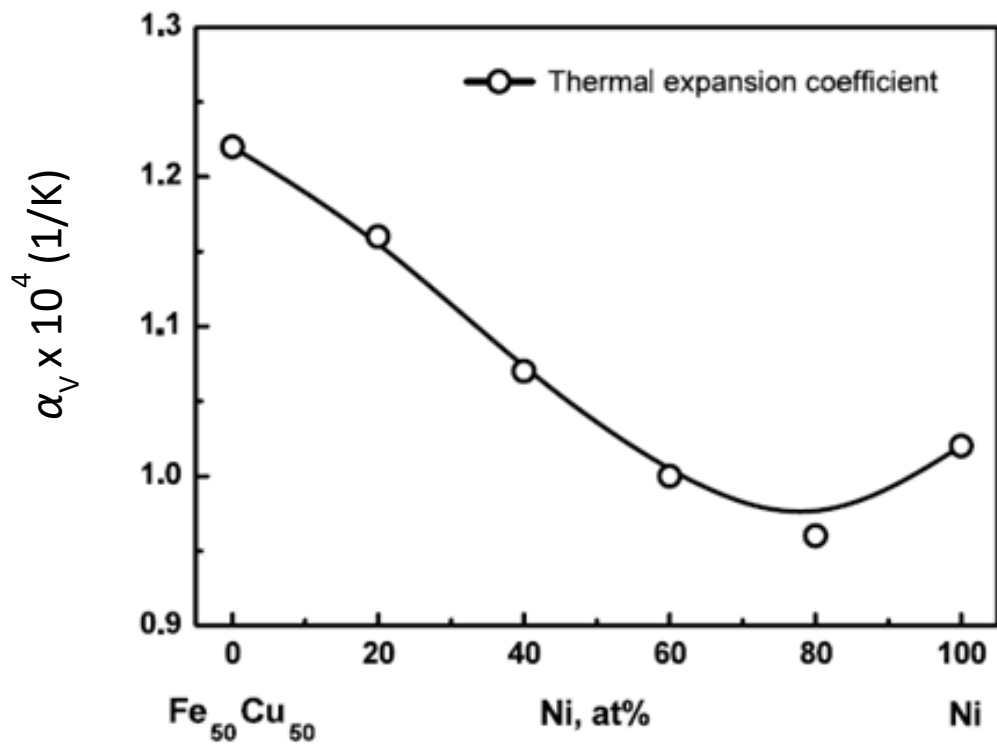


Fig. 11

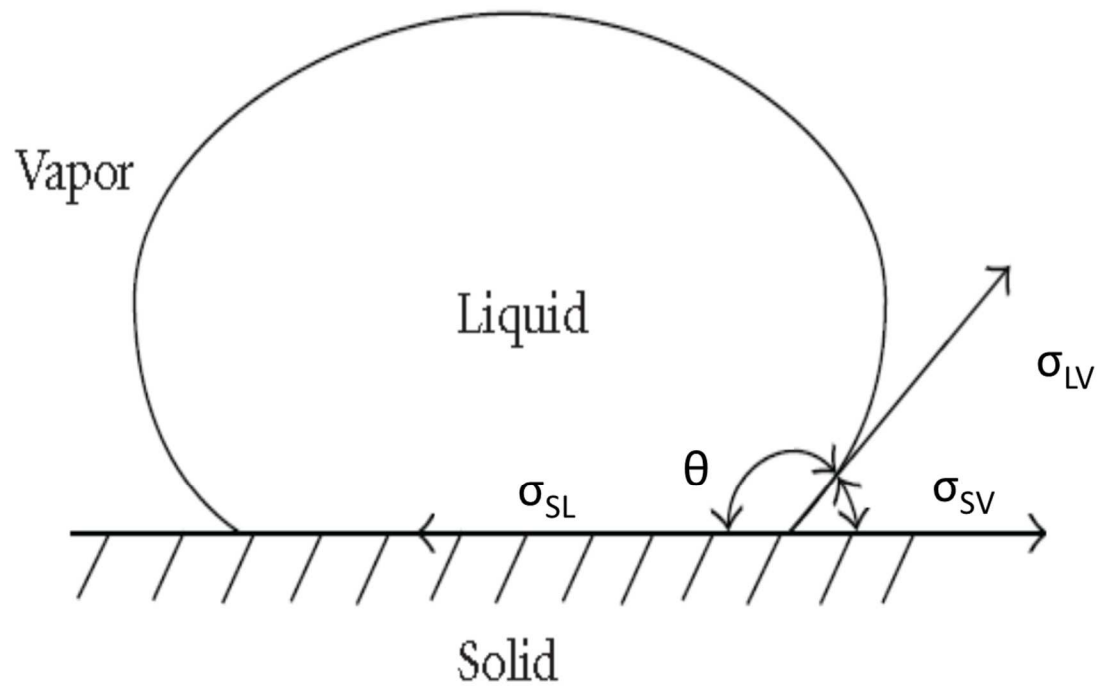


Fig. 12

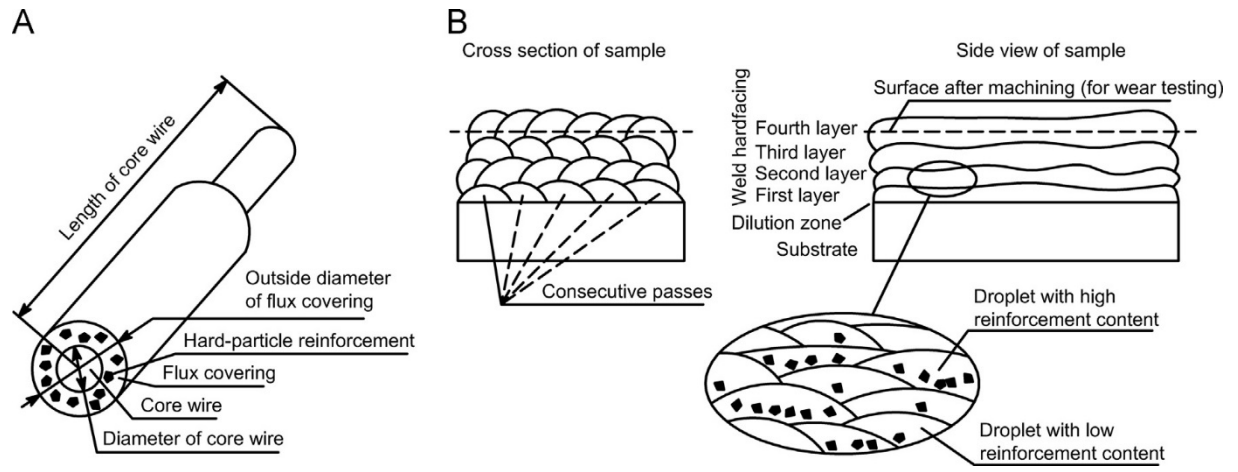
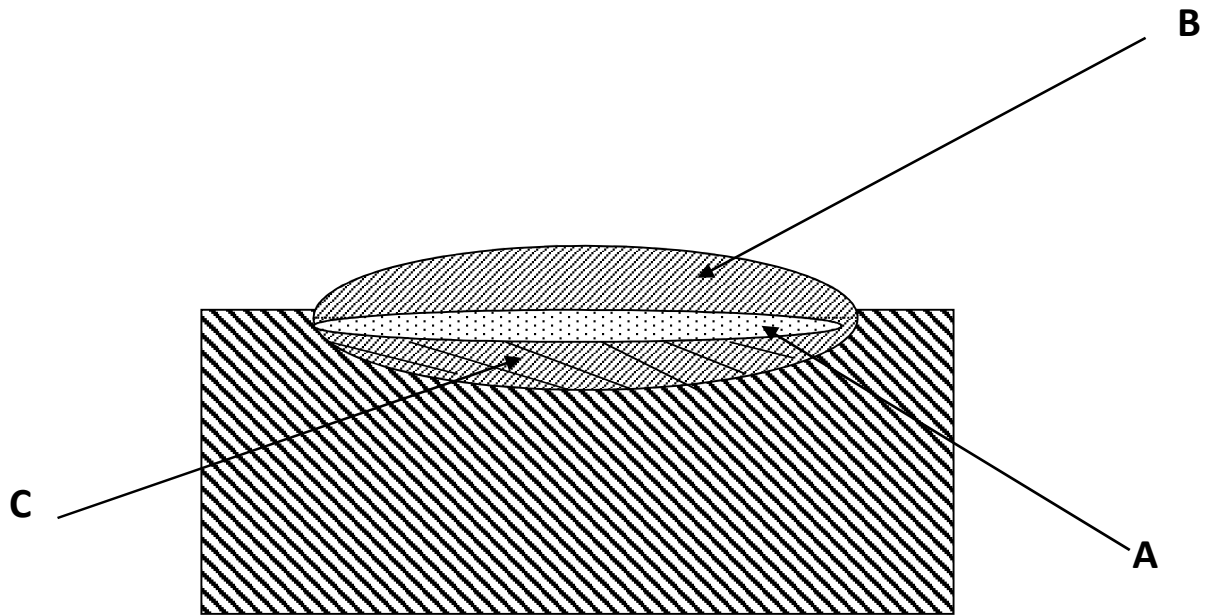


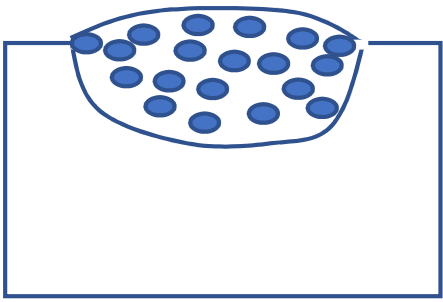
Fig. 13



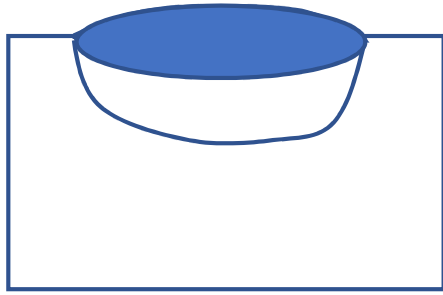
$$\text{Dilution} = A \times 100\% / (A + B)$$

Fig. 14

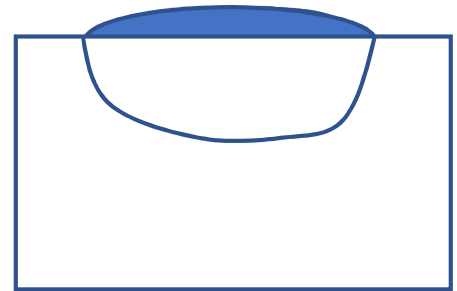
Error! Reference source not found.



a



b



c

Fig. 15

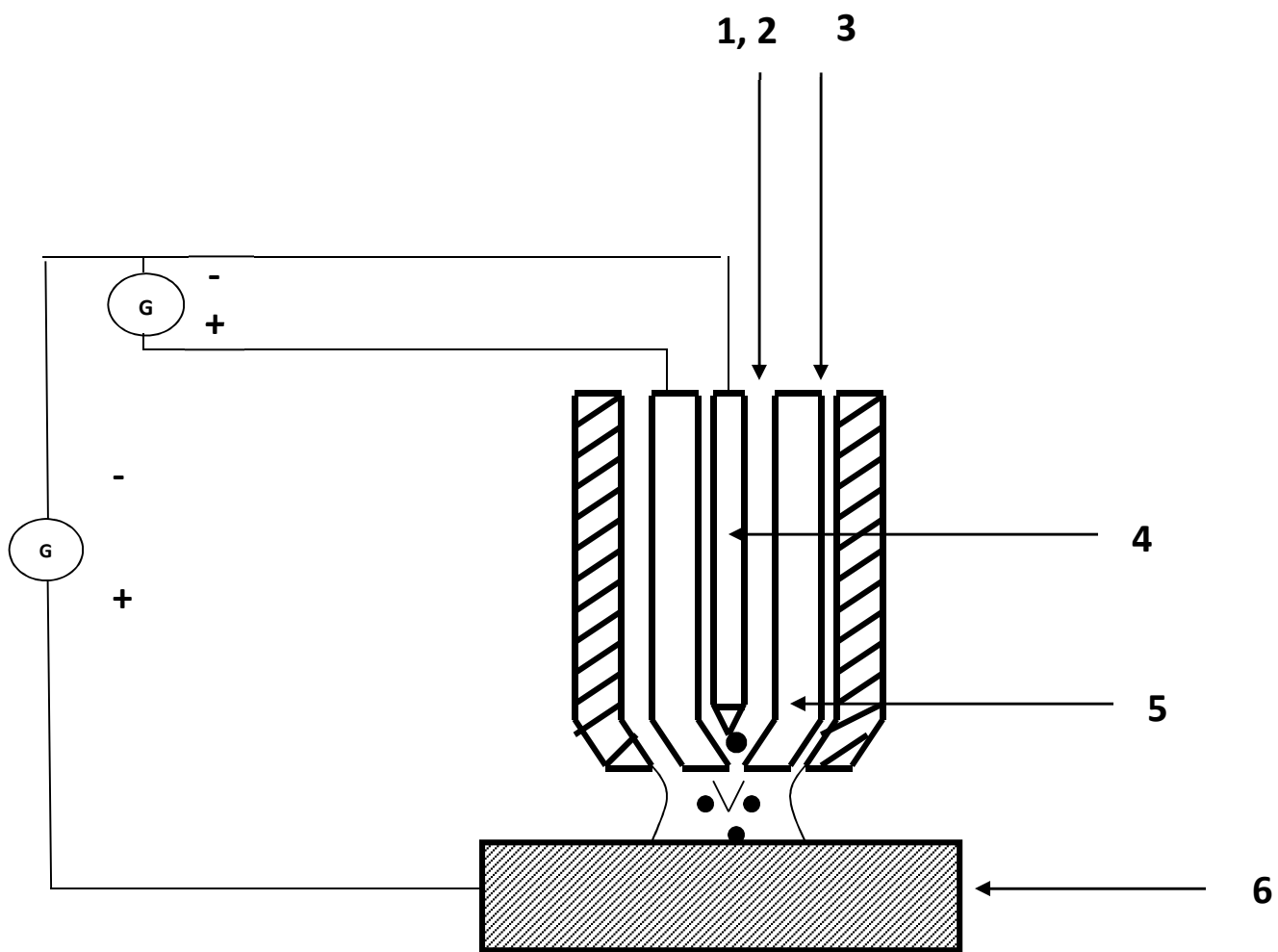


Fig. 16

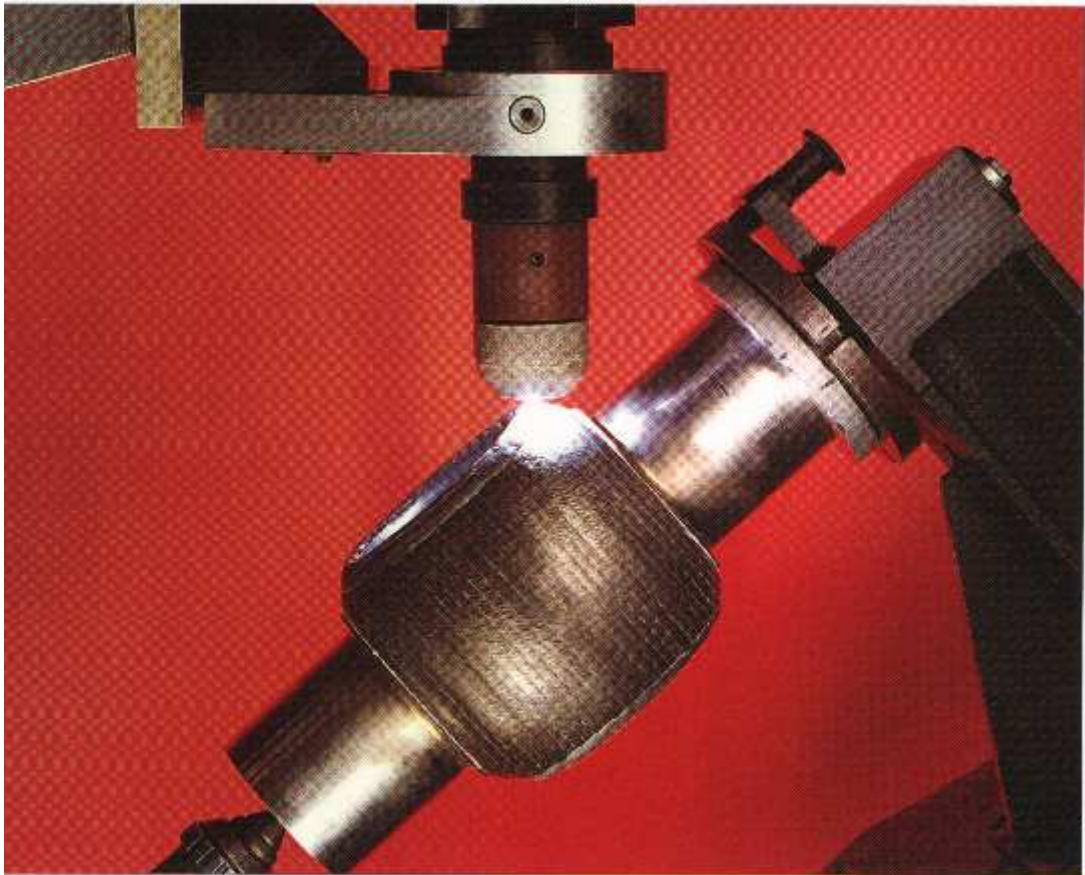
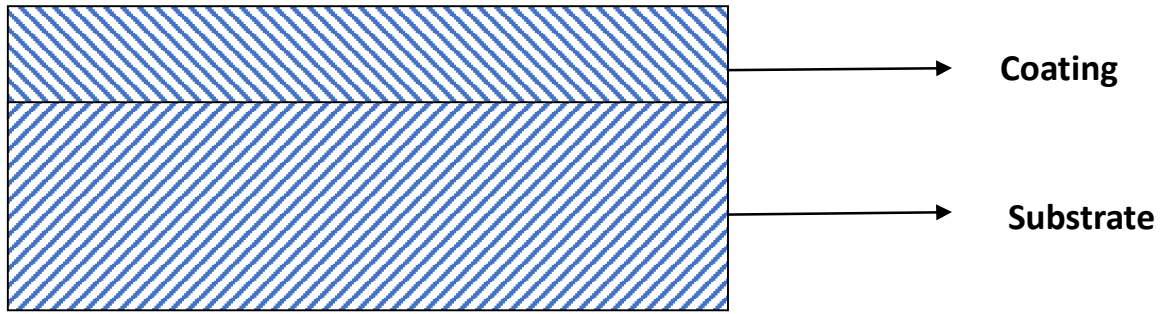
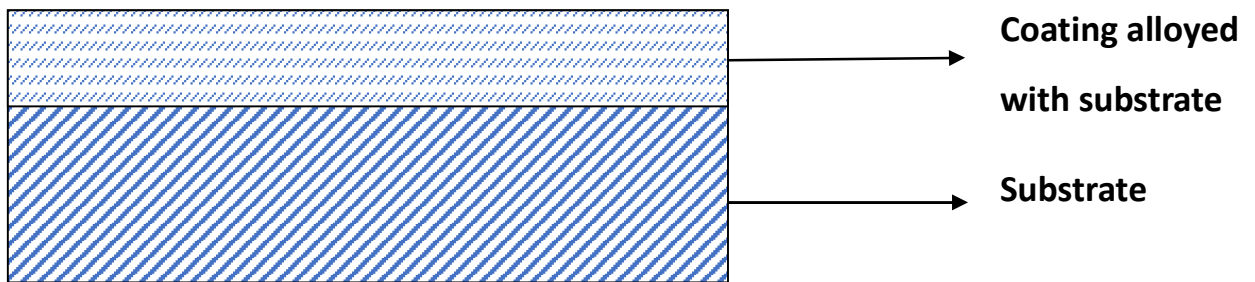


Fig. 17

Cladding



Alloying



Hard phase dispersion

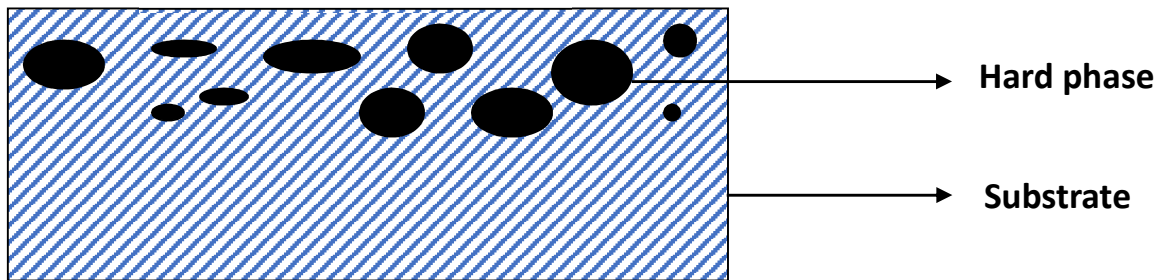


Fig. 18

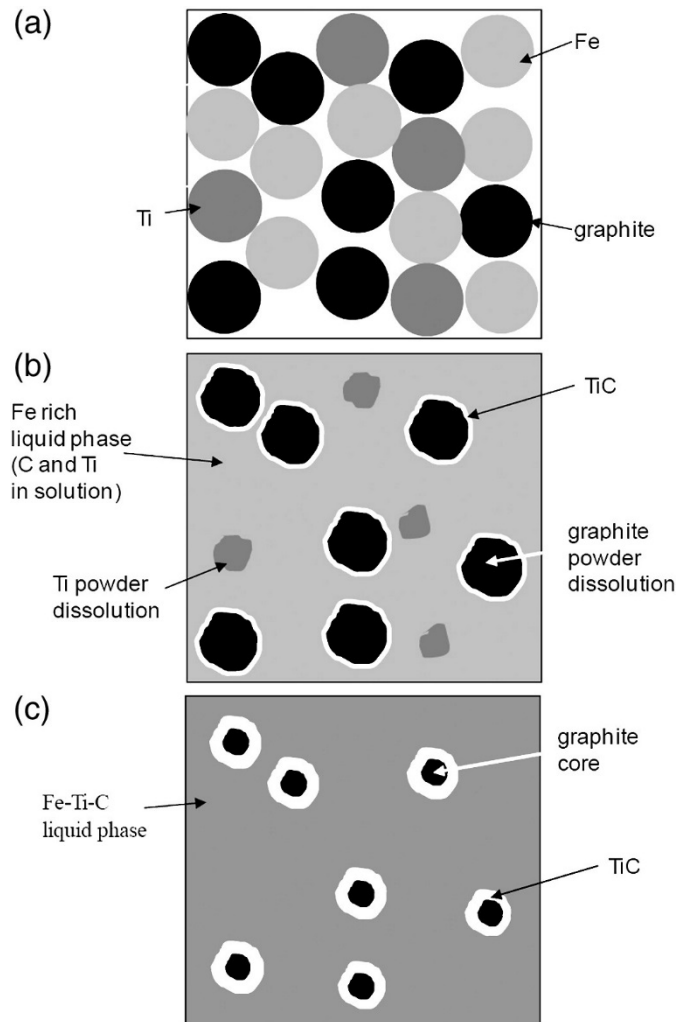


Fig. 19

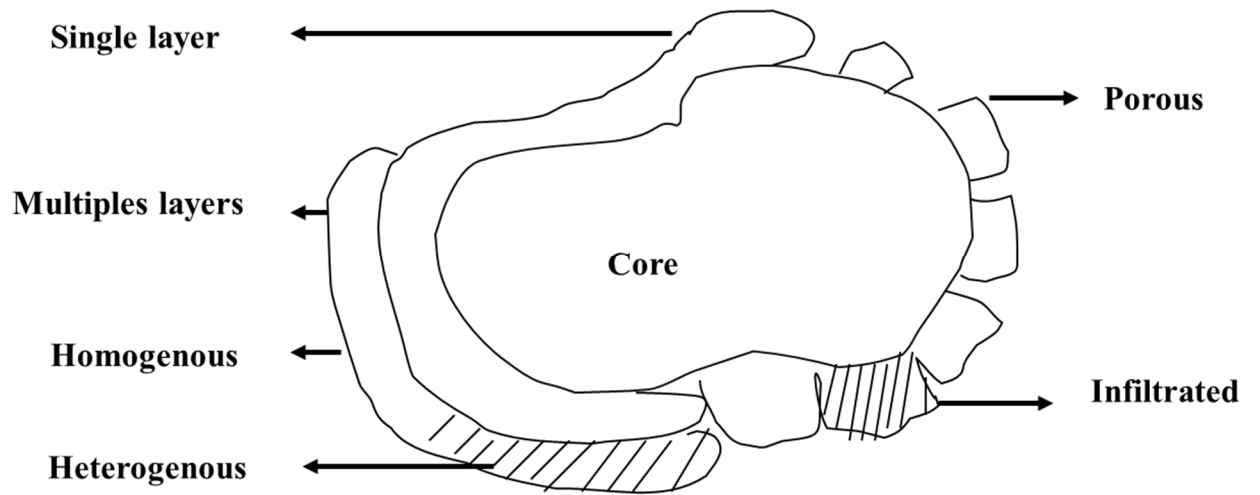


Fig. 20

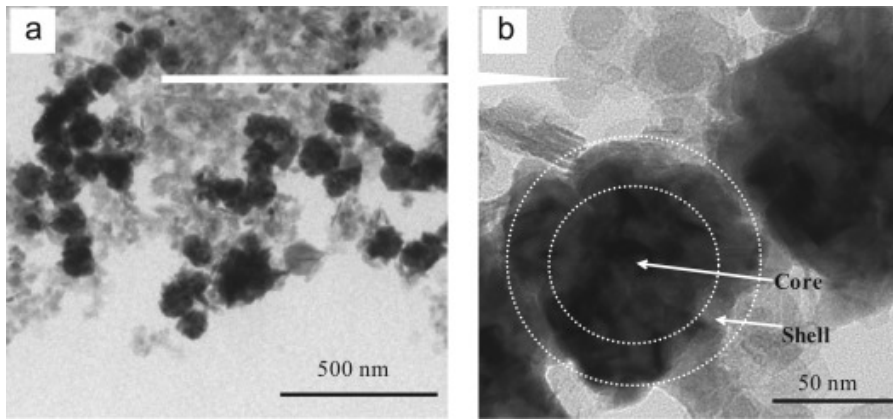
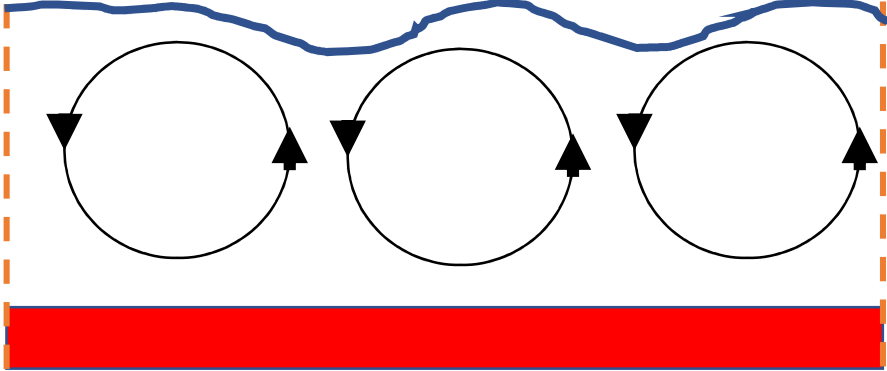


Fig. 21

Cold surface



Hot bottom part

Fig. 22

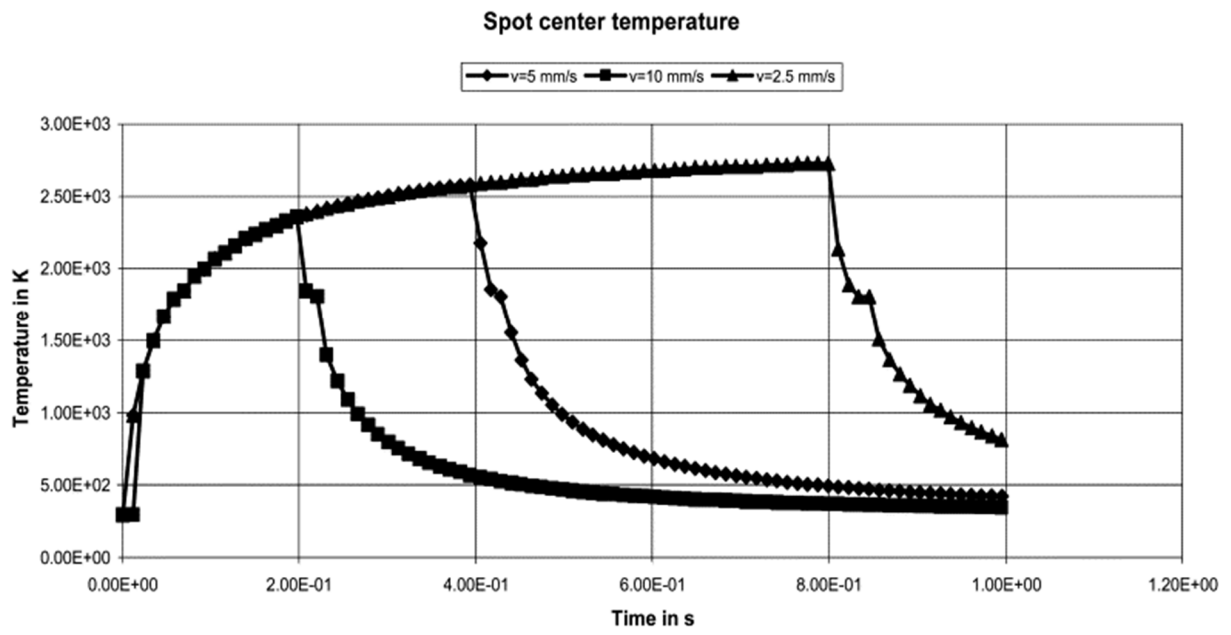


Fig. 23

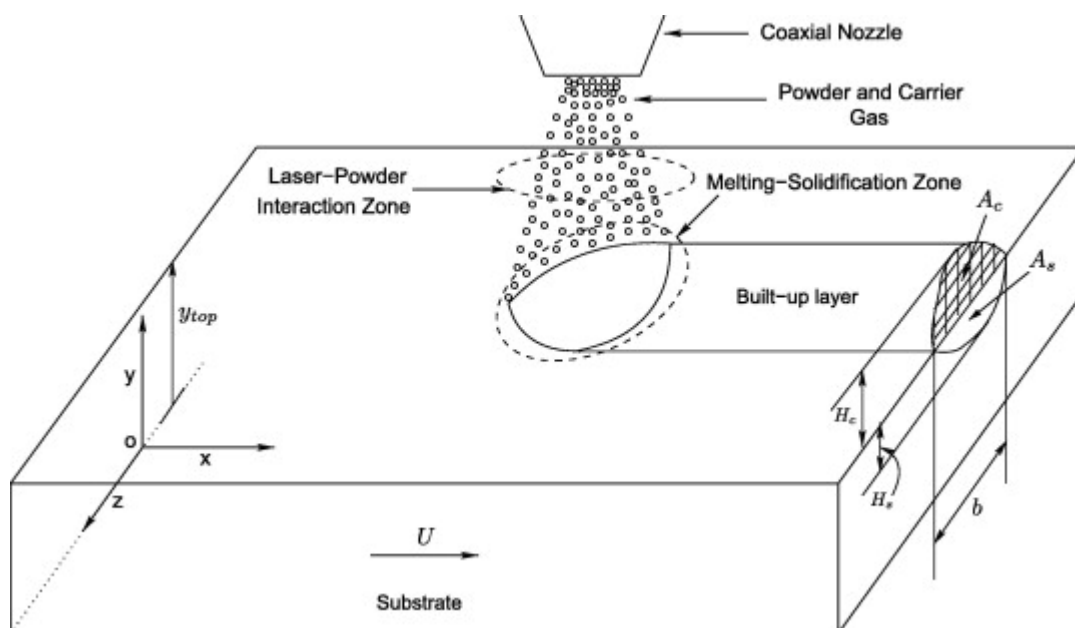


Fig. 24

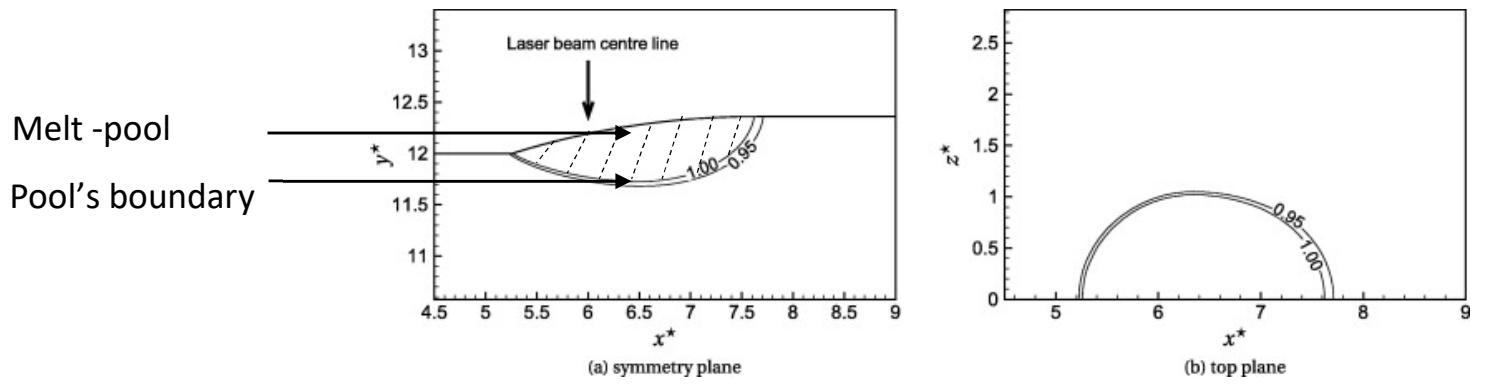


Fig. 25

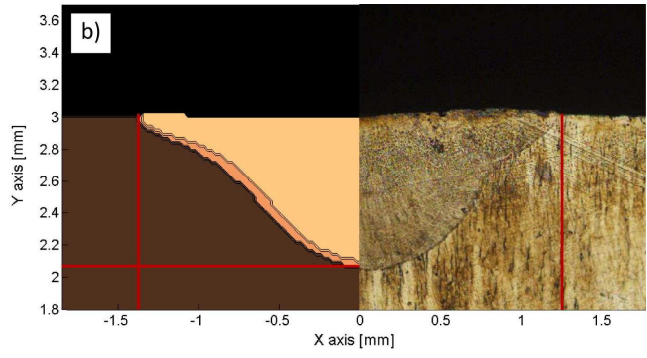
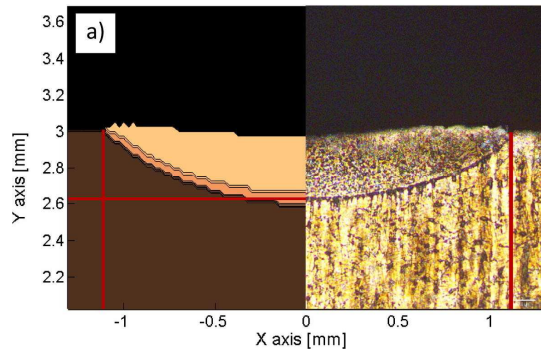


Fig. 26

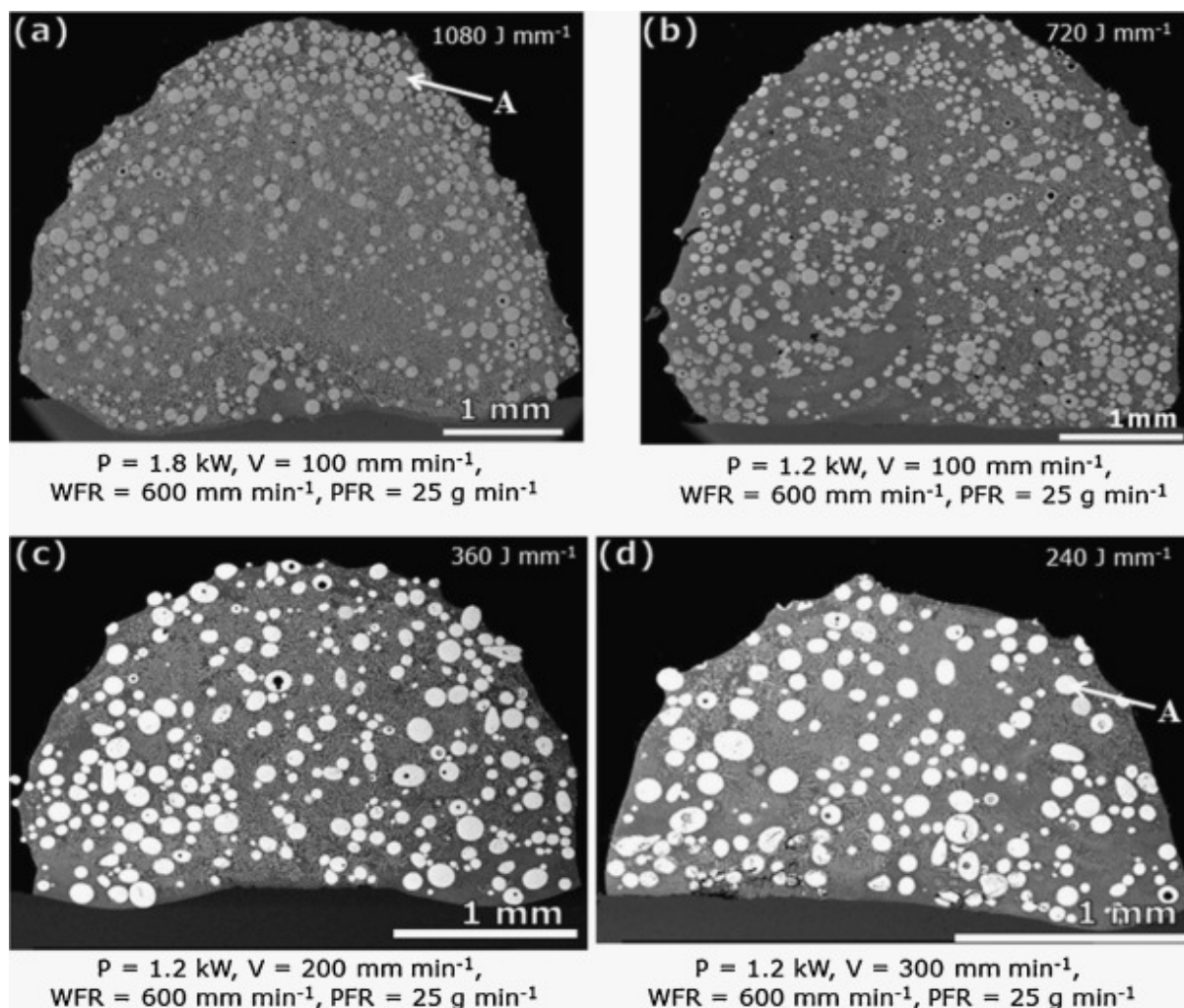


Fig. 27

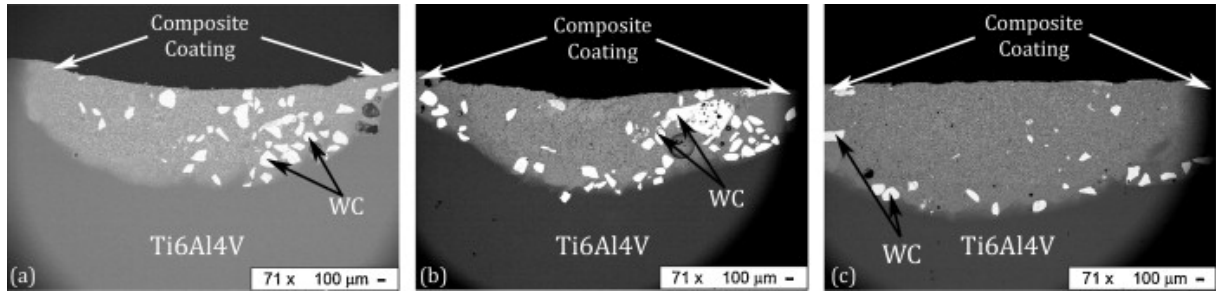


Fig. 28

Islands of agglomerated YSZ reinforcement

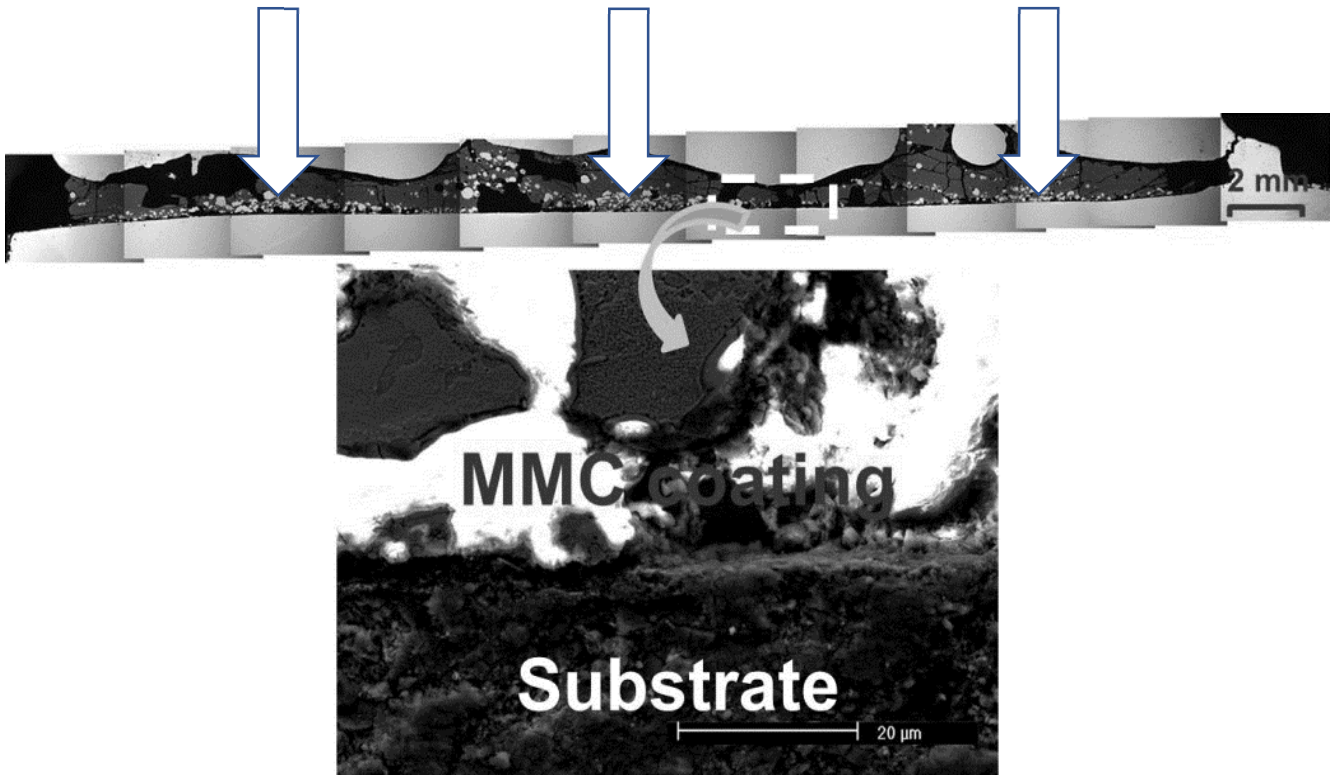


Fig. 29

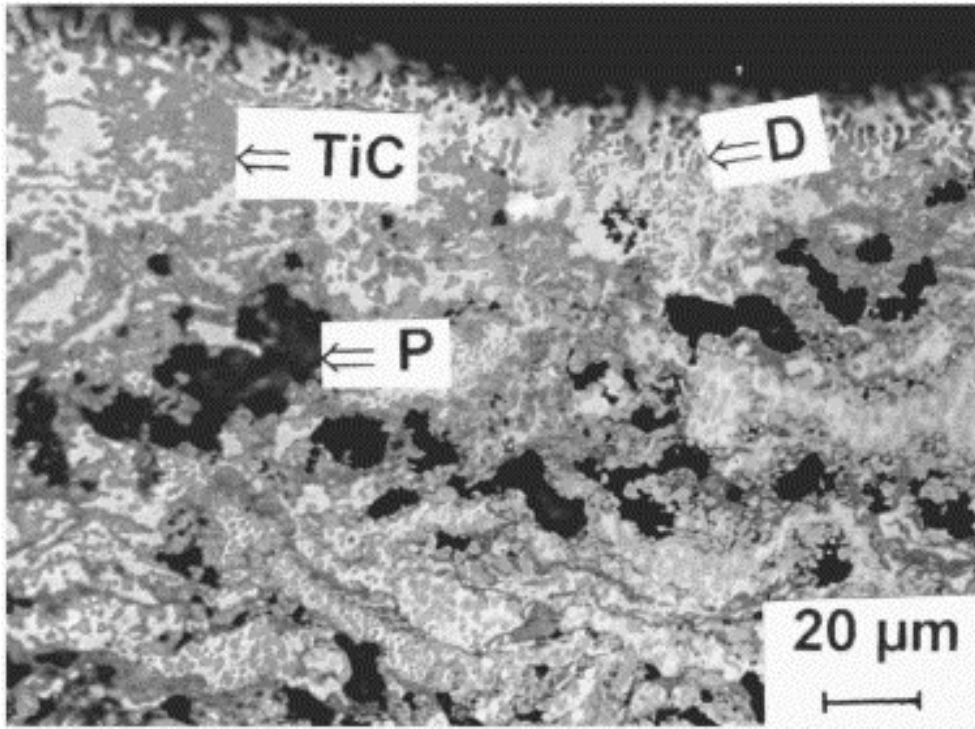


Fig. 30

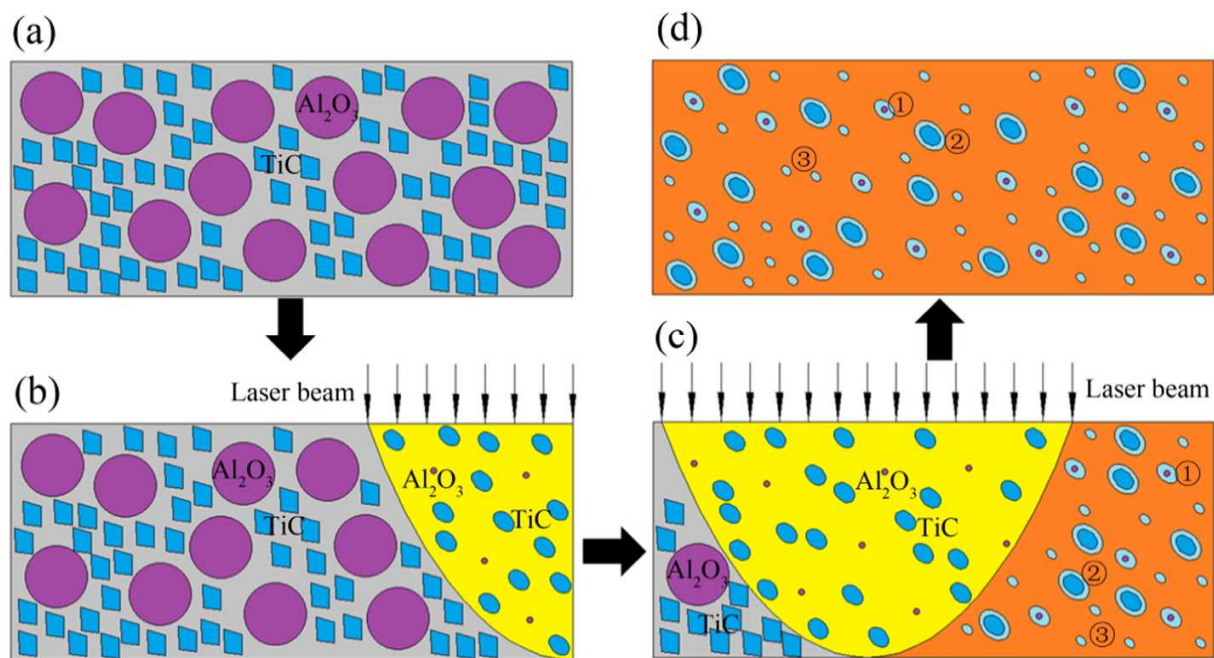


Fig. 31

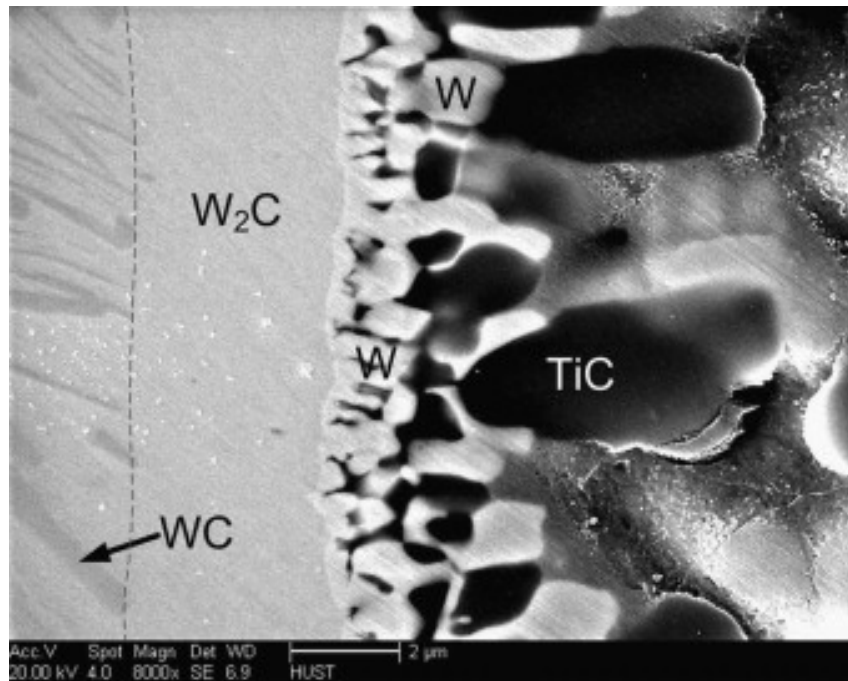


Fig. 32

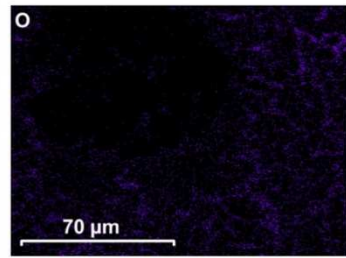
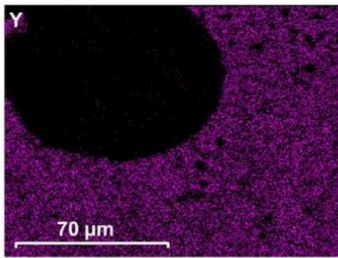
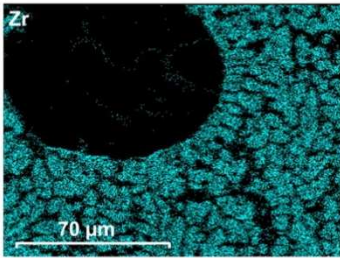
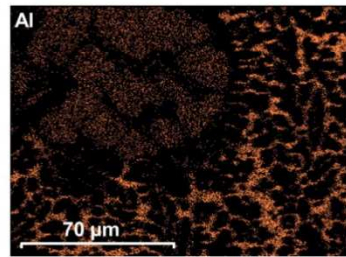
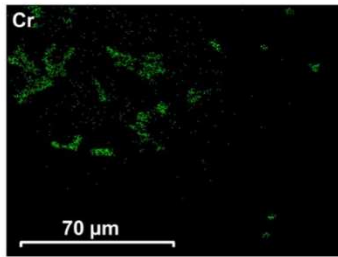
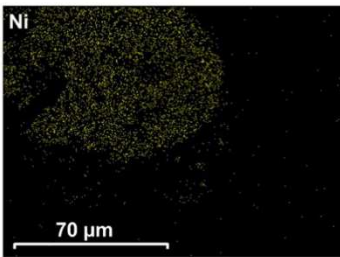
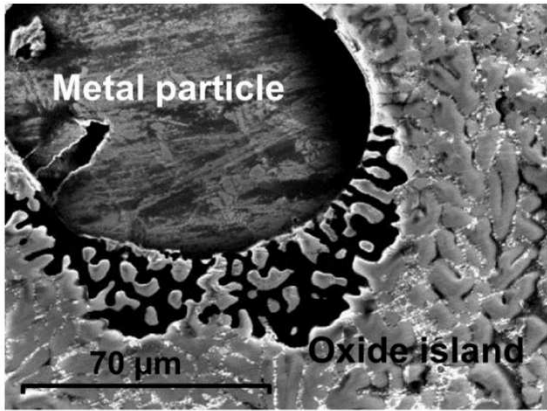


Fig. 33Error! Reference source not found.

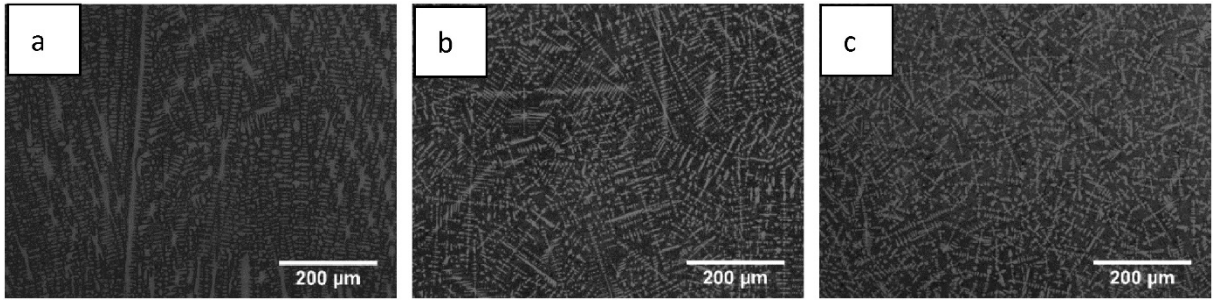


Fig. 34

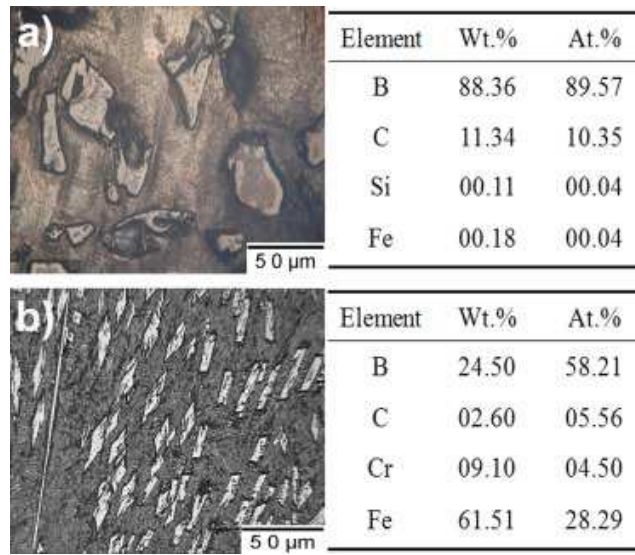


Fig. 35

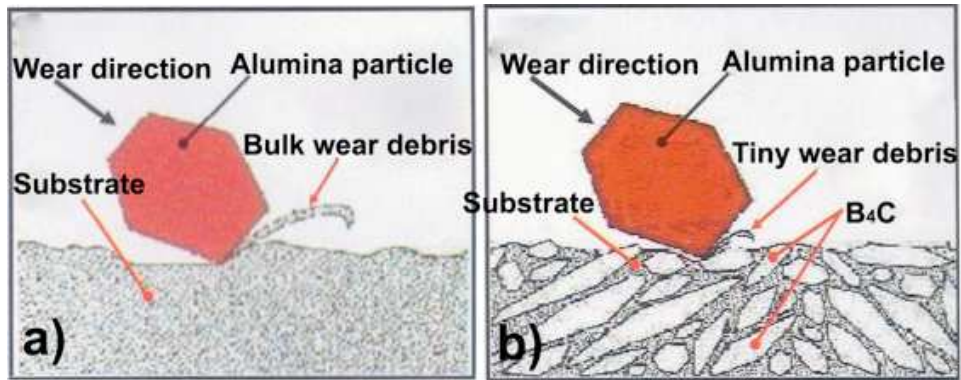


Fig. 36

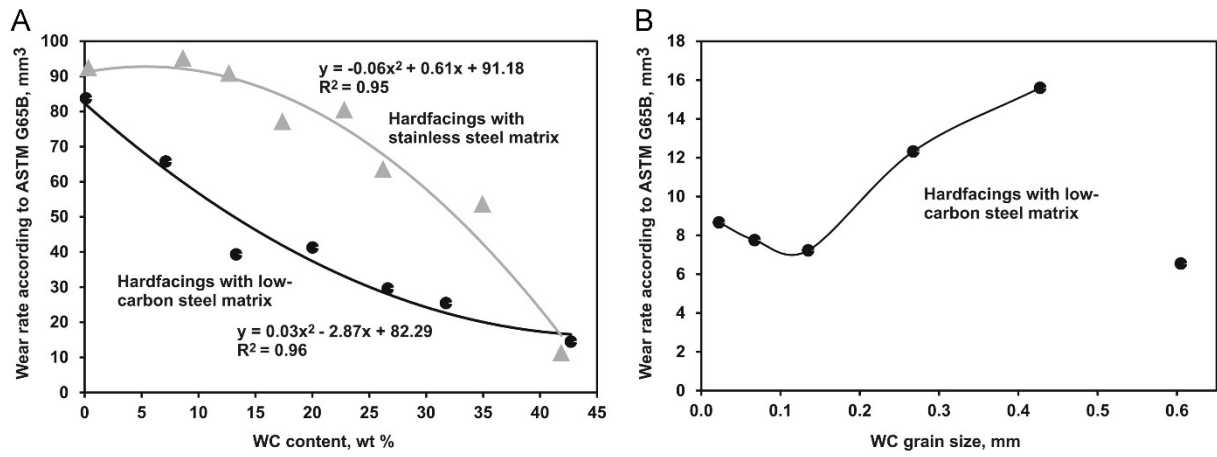


Fig. 37

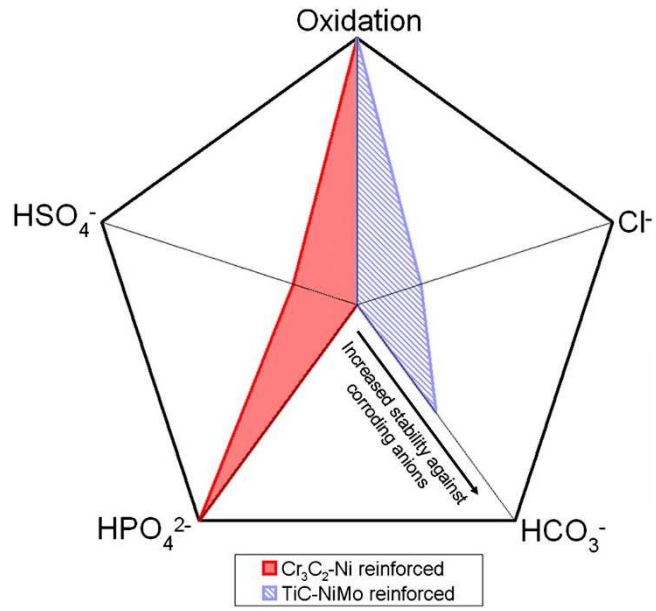


Fig. 38

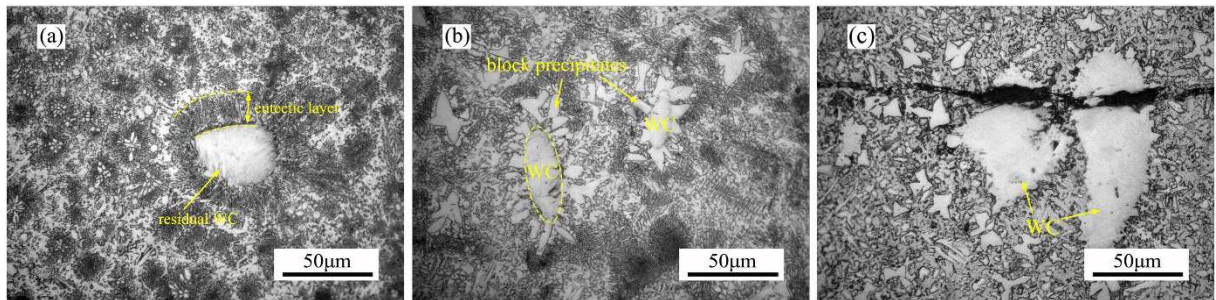


Fig. 39

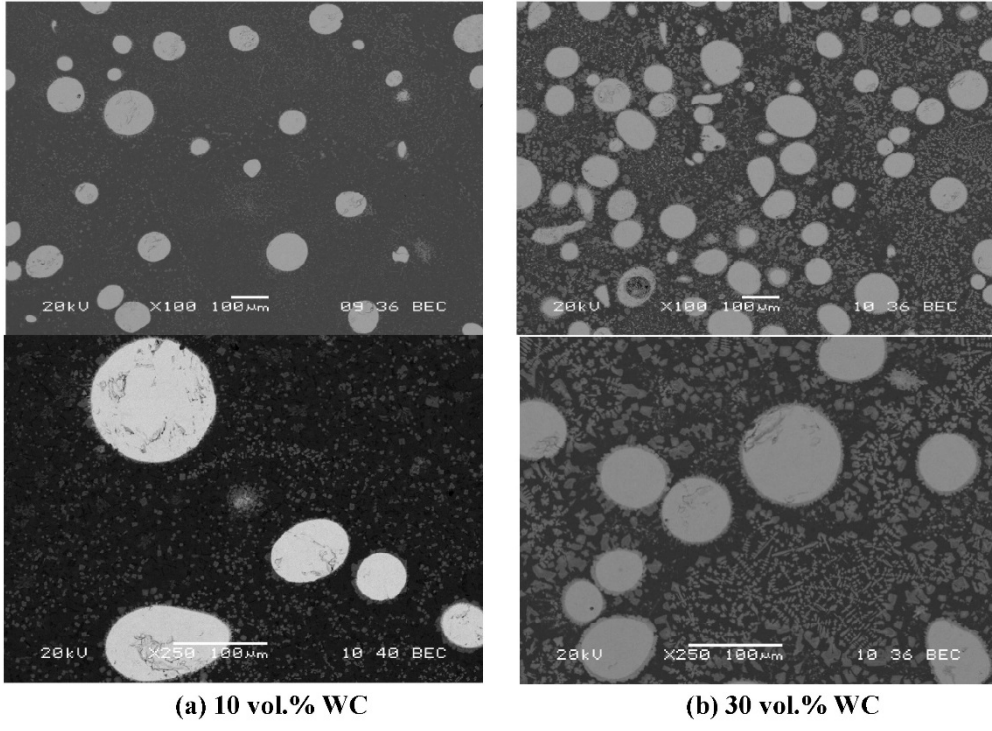


Fig. 40

Table 1 Some properties of metals [11]

Property	Al	Ni	Fe	Co	Cr	V	Ti
<i>Molar mass</i> M , g/mol	26.98	58.69	55.85	58.93	52.00	50.94	47.88
<i>Density</i> ρ , kg/m ³	2700	8910	7880	8900	7190	6110	4510
<i>Melting point</i> T_m , K	933.5	1728	1806	1768	2180	2163	1941
<i>Boiling point</i> T_{ev} , K	2743	3003	3023	3143	2943	3680	3558
<i>Brinell hardness</i> HV	167	638	608	1043	1060	628	970
<i>Elasticity (Young) modulus</i> E , GPa	70	200	211	209	279	128	116
<i>Shear modulus,</i> GPa	26	76	82	75	115	47	44

Table 2 Properties of NiCr (Ni + 20 wt. % Cr) in standard conditions [14]

Property	Value
<i>Elasticity (Young) modulus, E, GPa</i>	220
<i>Density, ρ, kg/m³</i>	8400
<i>Melting point, T_m, K</i>	1 673
<i>Specific heat, c_p, J/(kg.K)</i>	450
<i>Thermal conductivity, λ, W/(m.K)</i>	11.3
<i>Thermal expansion, α, K⁻¹</i>	14×10^{-6}

Table 3 Properties of nickel aluminides [16]

Property	Value
Density of Ni_3Al , ρ , kg/m ³	7160
Yield strength, σ_y , MPa	855
Rockwell hardness, HRC	12
Thermal conductivity of Ni_3Al , W/(m.K)	29
Thermal conductivity of $NiAl$, W/(m.K)	76
Melting point of Ni_3Al , T_m , K	1668
Melting temperature of $NiAl$, T_m , K	1955
Thermal expansion of Ni_3Al , α , K ⁻¹	12.5 x10 ⁻⁶
Thermal expansion of $NiAl$, α , K ⁻¹	13.2 x10 ⁻⁶

Table 4 Chemical compositions of some *Hastelloys* [19].

Alloy	Composition in wt. % (symbol * means maximum)									
	Co	Cr	Mo	W	Fe	Si	Mn	C	Ni	Others
B-2	1*	1*	28	–	2*	0.1*	1*	0.01*	Up to 100 %	–
B-3	3*	1.5	28.5	3*	1.5	0.1*	3*	0.01*	65 %	Al-0.5*, Ti-0.2*
C-4	2*	16	16	–	3*	0.08*	1*	0.01*	Up to 100 %	Ti-0.7*
C-2000	2*	23	16	–	3*	0.08*	–	0.01*	Up to 100 %	Cu-1.6
C-22	2.5*	22	13	3	3	0.08*	0.5*	0.01*	Up to 100 %	V-0.35*
C-276	2.5*	16	16	4	5	0.08*	1*	0.01*	Up to 100 %	V-0.35*

Table 5 Main chemical reaction in system Fe-Ti-C after Wang *et al.* [40].

System and possible reactions	Ti-C Ti+C→TiC	V-C V+C→VC	Fe-C		Fe-Ti
			3Fe+C→Fe ₃ C	2Fe+C→ Fe ₂ C	
<i>Standard free enthalpy of reaction</i> ΔG_i^0 (J/mol)	-186606+13.2T	-1020904 -9.581T	25 920-23T (298 K<T<463 K) 26 670-25T (463 K<T<1 115 K) 10 340-10T (1 155 K<T<1 808 K)	19 860-10T (298 K<T<1 115 K) 18 420-103 (1 155 K<T<1 808 K)	-53 300+53. 7T (298 K<T<2 000 K)

Table 6 **Surface tension** of some metals at the melting point [41]

Pure metal	Melting point temperature T_m , K	Surface tension γ , J/m ²
Ni	1728	1.778
Cr	2180	1.672
Co	1768	1.873
Al	933.5	0.914
Fe	1806	1.872
Si	1684	0.865
Zn	693	0.782

Table 7 - Carbon diffusion coefficient in iron and austenite [53-54]

$D=D_0 \exp(-Q/RT)$, m ² .s ⁻¹	Metal	D_0 m ² .s ⁻¹	Q , J.mole ⁻¹
	α -Fe	$25 \cdot 10^{-6}$	144000
	Austenite	$20 \cdot 10^{-6}$	83996

Table 8 Diffusion coefficients of N in liquid Fe and low carbon Fe-alloys [57, 59-60, 65-67]

System	Temperature T(K)	Coefficient of diffusivity $D, 10^{-9} \text{ m}^2/\text{s}$					
		N in liquid Fe and in low carbon alloys	1873	4.12	9.2	8.87	
	1600	5.6 (with very low carbon alloys)	5.5	9.2	14.89	3.7	4.41

Table 9 Experimental values of diffusion coefficient of N in the alloys including iron with other metals noted as X and Y at 1873 K. The content of other metals is 2.5% X and 2.5% Y [57].

X-Y	Ni-V	Co-V	Ni-Co	Ni-Cr	Co-Cr	Cr-V
Coefficient of diffusivity $D, 10^{-9} \text{ m}^2/\text{s}$	4.93	5.34	21.43	7.76	8.87	2.42
X-Y	Cr-Si	Cr-Mo	Mn-Co	Mn-Ni	Mn-Cr	Mn-V
Coefficient of diffusivity $D, 10^{-9} \text{ m}^2/\text{s}$	7.75	3.0	11.81	10.31	4.63	2.32

Table 10 Diffusivity of oxygen in liquid nickel and iron [70]

D (in liquid Ni)	T= 1773 K	$49 \times 10^{-8} < D < 81 \times 10^{-8} \text{ m}^2 \text{ s}^{-1}$
D (in liquid Fe)	T=1823 K	$25 \times 10^{-8} < D < 55 \times 10^{-8} \text{ m}^2 \text{ s}^{-1}$

Table 11 Surface tension of metals at melting point [71].

	Cu	Ag	Au	Ni	Pd	Pt	Co	Rh	Ir	Fe	
<i>Surface tension</i> $\gamma (T_m), \text{mJ.m}^{-2}$	1352	925	1211	1810	1467	1896	1779	2010	2241	1650	
<i>Melting point</i> <i>temperature</i> T_m, K	1358	1234	1338	1728	1828	2045	1768	2237	2716	1806	
Ru	Os	Mn	Tc	Re	Cr	Mo	W	V	Ti	Zr	Hf
2363	2508	986	2245	2755	1582	2110	2676	1902	1520	1669	1591
2606	3306	1519	2430	3459	2180	2896	3680	2175	1941	2128	2506
Sc	Y	Ce	Pr	Nd	Gd	Th	U	Al	Pb	Tl	Na
895	899	845	789	658	690	1108	1453	1031	466	439	215
1814	1799	1068	1208	1297	1585	2028	1405	933	601	577	371
K	Rb	Cs	Ca	Sr	Ba	Mg	Zn	Cd	Ta	Nb	Li
110	90	73	328	268	231	359	466	305	2467	2335	465
337	312	302	1115	1050	1000	923	693	594	3290	2750	454
Be	La										
1637	901										

Table 12 - Physical properties of oxides [11]

	Al ₂ O ₃	ZrO ₂	Y ₂ O ₃	CeO ₂
<i>Molar mass</i> <i>M, g/mol</i>	101.96	123.218	225.81	172.115
<i>Density</i> <i>ρ, kg/m³</i>	3987	5680	5010	7215
<i>Melting temperature</i> <i>T_m, K</i>	2345	2988	2698	2670
<i>Boiling temperature</i> <i>T_{ev}, K</i>	3250	4570	4570	3770
<i>Specific heat,</i> <i>J/(mol.K)</i>	78.83	56.21	102.51	61.52
<i>Standard enthalpy of formation</i> <i>ΔH_f⁰, kJ/mol</i>	-1675.7	-1080	-1905	--1088.7

Table 13 Physical properties of typical carbides [11]

	WC	TiC	Cr ₃ C ₂	B ₄ C	VC (VC _{0.88})	MoC and Mo ₂ C
<i>Molar mass</i> <i>M, g/mol</i>	195.85	59.89	180.09	55.26	62.95	107.961 (MoC) 203.911 (Mo ₂ C)
<i>Density</i> <i>ρ, kg/m³</i>	15630	4930	6680	2520	5577	8900
<i>Melting temperature</i> <i>T_m, K</i>	3058	3430	2168	3036	3080	2960
<i>Boiling temperature</i> <i>T_{ev}, K</i>	6270	5090	4070	3770	4171	-
<i>Thermal conductivity</i> <i>λ, W/(m.K)</i>	110	-	-	-	-	-
<i>Specific heat,</i> <i>J/(mol.K)</i>	39.8	34.0	99.21	52.46	32.31	37.601 (MoC) 59.014 (Mo ₂ C)
<i>Standard free enthalpy of formation</i> <i>ΔH_f⁰ [kJ/mole]</i>	-40.584	-183.7	-85.349	-62.68	-101.7	-284.510 (MoC) -531.276 (Mo ₂ C)
<i>Elasticity (Young) modulus</i>	530-700	400	-	460	380	-

E, GPa						
--------	--	--	--	--	--	--

Table 14 Wetting by non-reactive liquid metals (after Dezellus and Eustathopoulos [79])

Kind of solid	Contact angle θ	Examples of contact angles
Solid metals	$\theta \ll 90^\circ$	Pb/Fe - 40° AgCu/Stainless Steel - 10° - 60°
Semiconductors		Sn/Ge - 40°
Ceramics with a partially metallic behavior		AgCu/Ti ₃ SiC ₂ - 10° Au/ZrB ₂ - 25°
Carbon materials	$\theta \gg 90^\circ$	Au/C - 119° - 130°
Iono-covalent oxides		Cu/Al ₂ O ₃ , Cu/SiO ₂ - 120° - 130°
Covalent ceramics		Al/AlN - 134° - 138° Au/BN - 135° - 150°

Table 15 -Selected characteristics of industrial lasers applied in laser assisted deposition coatings methods [112-115]

Parameter	Laser type			
	CO ₂	Nd doped YAG	Diode laser	Fibre laser
Wavelength, μm	10.6	1.06	0.82-1.07	0.4 – 2.8 (most frequent 1.05 for Ytterbium doped fibre)
Excitation technique	Gas discharge	Flash or arc lamp	Electric excitation (electrons passing <i>band gap</i>)	Optical pumping of diode's light
Pulsed/cw	Both	Both	Both	Both
Maximum average power, kW	100	15	3	20
Beam quality	Very high	Low	Low	Very high
Efficiency, %	5-10	2-5	Up to 70	Optical-to-optical efficiency up to 70% and total efficiency up to 35%

Table 16 Cermet powders and wires used for plasma/ flame and laser cladding [117-121]

N	Substrate	Powders/wires						Method of cladding	Powder feed rate, g/min	Reference
		Ceramic reinforcement	Metallic matrix, wt. %	Size matrix, μm	Size of reinforcement, μm	Chemical composition, vol. %	Powder preparation			
1	Mild steel (1.0037)	WC-Co	NiCrSiFeB=Ni+4Cr+2.5Si+2Fe+1B+1Al	Powder: +32-125	+150-410	NiCrSiFeB+25,30, and 40 WC-Co	Recycled powders treated chemically	PTA	35	Zikin <i>et al.</i> [117]
2	Steel (SS40)	Cr ₂ C ₃ or TiC	Stellite 6: Co+28Cr+4W	Powder:+53-150	About 39, 79, and 148	Stellite+20, 30, and 40 Cr ₂ C ₃ or TiC		PTA	45	Deuis <i>et al.</i> [8], Araki <i>et al.</i> [118]
3	Stainless steel 316 L	CaP: HA+TCP+TTCP	Ti-6Al-4V alloy	Powders: mean 75	-	Ti-6Al-4V+33 wt. % CaP	Alloy was gas atomized	CO ₂ laser prototyping	2.2	Mansur <i>et al.</i> [119]
4	Steel Grr22	Cr ₂ C ₃	Inconel 625: Ni+21.5Cr+9Mo+4Nb	Powder:+45-90	-44	Inconel+20 wt.% Cr ₂ C ₃		Diode laser cladding	16.5	Chang <i>et al.</i> [120]
5	Stainless steel 304	WC+W ₂ C	Inconel 625 (as in line 3)	Wire, OD 1.2 mm	+40-160	Inconel+35 to 49 carbides (Estimated from volume fraction of carbides equal to 24 to 49 %)	Carbide was made by cold crucible induction fusion system	Fibre laser cladding	Inconel: 5.7; carbides: 25	Abioye <i>et al.</i> [121]

Table 17 Mechanical properties of plasma/flame cladded cermets [108, 120, 141-1454]

No	Cermet composition (reinforcement + matrix wt. %)		Process of cladding	Properties			Reference
	Reinforcement	Matrix		Hardness	Elasticity modulus	Wear resistance	
1	TiC+20 NiMo	NiCrBSi	PTA	Matrix about 2 GPa Carbide about 34 GP	Matrix about 230 GPa Carbide about 390 GPa		Zikin <i>et al.</i> [108]
2	Cr ₃ C ₂	60 NiCrBSi	PTA	HV10=680 at RT and HV10=300 at 973 K		Impact-abrasive volumetric wear 12 mm ³ at RT and 18 mm ³ at 973 K	Chang <i>et al.</i> [120]
3	B ₄ C	80 (Fe+12 Cr+1 B+ 1 Si)	Injection of powders into plasma formed melt pool			Pin-on-disk test 0.05 mg/(mN) depending on B ₄ C injection geometry (see Fig. 36)	Lyu <i>et al.</i> [141]
4	TiC	47 Fe	Reactive plasma cladding of pre-prepared powder	HV0.2 in the range 1350 to 1900		Ball-on-disk wear test about 0.01 mm ³ volume worn	Liu <i>et al.</i> [142]
5		40 vol. % γ-(Fe,Ni)	PTA	HV0.5 above 1600		Ball-on-disk fretting wear test about 0.22 mm ³ volume worn	Chen <i>et al.</i> [143]
6	WC	40 vol. % CuNiMn	Flame spraying of WC and CuNiMn particles including wire	HV0.2 of matrix 125 and of reinforcement 2440		3-body abrasion test with silica sand show volume loss of 100 mm ³ after sliding distance of 800 m	J. Liu <i>et al.</i> [144]
7	WC-8 Co large particles	Steel	Injection of reinforcement particles in substrate melted by transferred plasma arc	HV0.01 about 800			A. Liu <i>et al</i> [145]

Table 18 Mechanical properties of laser cladded cermets [120, 134, 147-150]

No	Cermets composition (reinforcement + matrix wt. %)		Process of cladding	Properties			Ref.
	Reinforcement	Matrix		Hardness	Elasticity modulus	Wear resistance	
1	TiC	70 NiCr	Pulsed Nd: YAG laser cladding of injected powder	HV0.5=620		Erosion visible after use of 1050 g of quartz sand	Kathuria [148]

2		Stainless steel AISI 304	Pulsed Nd: YAG laser cladding of preplaced powder	HV0.05 from 400 to 1200			Kumar <i>et al.</i> [149]
3	WC	70 Ni	Cw CO ₂ laser cladding of preplaced powder	HV0.1 about 745		Ball-on-disc sliding wear volume about 2.4 mm ³	Luo <i>et al.</i> [150]
4		70-90 vol. % NiCrBSi	Cw high power diode laser cladding of injected powder	HB from 440 to 573 HB 513 for pure matrix		Abrasion wheel test wear loss of 30 to 40 mm ³	Deschuyteneer <i>et al.</i> [147]
5	Cr ₂ C ₃	80 Inconel 625 (NiCrMoNbFe)	High power diode laser cladding of injected powder		About 243 GPa (211 GPa for matrix)		Chang <i>et al.</i> [120]
6	Cr ₂ C ₃ powder with particles clad with 50 wt. % NiCr	50 NiCrSiB	Cw CO ₂ laser cladding of preplaced powder	HV0.2 of 950 to 1200			Dawei <i>et al.</i> [134]